Tool-part tribological interaction assessment for continuous deformation processes

Alejandra Torres Chamorro

Tool-part tribological interaction assessment for continuous deformation processes

Alejandra Torres Chamorro

Thesis submitted to *Universitat Politècnica de Catalunya* in partial fulfilment of the requirements for the degree of Doctor in Mechanical Engineering, Fluids and Aeronautic

UNIVERSITAT POLITÈCNICA DE CATALUNYA
BARCELONATECH
UPC
Escola d'Enginyeria de Barcelona Est

eurecat

Alejandra Torres Chamorro

Tool-part tribological interaction assessment for continuous deformation processes

Doctoral thesis

Supervised by Dr. Ing. Antonio Travieso Rodríguez

Supervised by Dr. Jordi Llumà i Fuentes

Supervised by Dr. Nuria Cuadrado Lafoz

Supervised by Dr. Montserrat Vilaseca Llosada

Title: Tool-part tribological interaction assessment for continuous deformation processes

Author: Alejandra Torres Chamorro

Advisors: Dr. Ing. Antonio Travieso Rodríguez
                   Dr. Jordi Llumà i Fuentes
                   Dr. Nuria Cuadrado Lafoz

Abstract: This dissertation is an experimental assessment of the tool-part tribological interaction of continuous deformation processes: ball burnishing as a superfinishing process and wire drawing as a bulk deformation process. Through the integration of friction as their fundamental parameter, these processes can be optimized. Thus, after the determination of the coefficient of friction, its impact on the final components surface integrity (hardness, roughness, and residual stresses), as well as the resulting wear mechanisms (adhesion and abrasion) from the sliding contact between hardmetal (WC/Co) and the treated materials (stainless-steel and aluminum alloy), has been analyzed by means of advanced characterization techniques such as: X-ray diffraction (XRD), field emission scanning electron microscope (FE-SEM), energy dispersive x-ray analysis (EDX) and confocal scanning optical microscopy (CSOM). The results have shown that beyond the operational parameters and the macro-contact conditions, the influence of the micro-contact, microstructure and chemical composition, represent critical points in the tribological behavior of each process. In addition, these experimental outcomes constitute validation tools for numerical models, allowing integral configurations that surpass the simplified models that so far have not achieved adjustments in terms of surface finish and residual stresses, simultaneously. Therefore, potential solutions to the misalignments of each study case have been established from the analysis of a hitherto underestimated factor: friction.

Keywords: Tribology, friction, deformation processes, ball burnishing, wire drawing, stainless-steel, aluminum alloys, wear mechanisms

Títol:	Avaluació de la interacció tribològica eina-peça per a processos de deformació contínua
Autora:	Alejandra Torres Chamorro
Assessors:	Dr. Ing. Antonio Travieso Rodríguez Dr. Jordi Llumà i Fuentes Dra. Nuria Cuadrado Lafoz

Resum:

Aquesta tesi és una avaluació experimental de la interacció tribològica eina-part dels processos de deformació contínua: el brunyit amb bola com a procés de superacabat i el trefilat com a procés de deformació massiu. Mitjançant la integració de la fricció com a paràmetre fonamental, aquests processos es poden optimitzar. Així, després de la determinació del coeficient de fricció, el seu impacte en la integritat superficial dels components finals (duresa, rugositat i tensions residuals), i en els mecanismes de desgast resultants (adhesió i abrasió) pel contacte de lliscament entre metall dur (WC/Co) i els materials tractats (acer inoxidable i aliatge d'alumini), s'ha analitzat mitjançant tècniques de caracterització avançades com ara: difracció de raigs X (XRD), microscòpia electrònica d'escaneig d'emissió de camp (FE-SEM), anàlisi de dispersió d'energia de raigs X (EDX) i microscòpia òptica d'escaneig confocal (CSOM). Els resultats han demostrat que més enllà dels paràmetres operatius i de les condicions de macro-contacte, la influència del micro-contacte, la microestructura i la composició química, representen punts crítics en el comportament tribològic de cada procés. A més, aquests resultats experimentals constitueixen eines de validació de models numèrics, que permeten configuracions integrals que superen els models simplificats que fins ara no han aconseguit ajustos en termes d'acabat superficial i esforços residuals, simultàniament. Per tant, s'han establert solucions potencials als desajustaments de cada cas d'estudi a partir de l'anàlisi d'un factor fins ara subestimat: la fricció.

Paraules clau:	Tribologia, fricció, processos de deformació, brunyit, trefilat, acer inoxidable, aliatges d'alumini, mecanismes de desgast

Título:	Evaluación de la interacción tribológica herramienta-pieza para procesos de deformación continua
Autora:	Alejandra Torres Chamorro
Asesores:	Dr. Ing. Antonio Travieso Rodríguez Dr. Jordi Llumà i Fuentes Dra. Nuria Cuadrado Lafoz

Resumen: Esta disertación trata sobre la evaluación experimental de la interacción tribológica herramienta - pieza para procesos de deformación continua: el bruñido con bola como proceso de superacabado y el trefilado de alambre como proceso de deformación masivo. Mediante la integración de la fricción como su parámetro fundamental, estos procesos pueden ser optimizados. Así, después de la determinación del coeficiente de fricción, su impacto en la integridad superficial de los componentes (dureza, rugosidad y tensiones residuales) y en los mecanismos de desgaste resultantes (adhesión y abrasión) del contacto por deslizamiento entre el metal duro (WC/Co) y los materiales tratados (acero inoxidable y aleación de aluminio), se ha analizado mediante técnicas de caracterización avanzadas: Difracción de rayos X (DRX), microscopía electrónica de barrido (FE-SEM), dispersión de energía de rayos X (EDX) y microscopía óptica confocal (CSOM). Los resultados muestran que más allá de los parámetros operativos y de las condiciones de macro-contacto, la influencia del micro-contacto, la microestructura y la composición química, representan puntos críticos en la tribología de cada proceso. Además, estos resultados constituyen herramientas de validación de modelos numéricos, permitiendo configuraciones integrales que superan los modelos simplificados que hasta ahora no han logrado ajustes en acabado superficial y tensiones residuales, simultáneamente. De esta manera, se han establecido soluciones a partir del análisis de un factor hasta ahora subestimado: la fricción.

Palabras clave: Tribología, fricción, procesos de deformación, bruñido, trefilado, acero inoxidable, aleaciones de aluminio, desgaste.

Acknowledgement

Saying thank you, is a way of showing appreciation for the memories kept, not only in the mind, but also in the heart. Therefore, it is in my heart I keep every word said, every trust shown, time spend, and the support given by each one of my directors during this doctoral thesis development. My most sincere gratitude goes to all of them: Dr. Montserrat Vilaseca, Dr. Nuria Cuadrado, Dr. Antonio Travieso and Dr. Jordi Llumà. I will always consider myself fortunate to have found on my path, leaders who, in addition to their great knowledge and expertise, also have a deep sense of humanity. I also want to thank Dr. Daniel Casellas, Scientific Director of the Research Center of Catalonia EURECAT, for the opportunity to be part of this noble institution through the Vicente López scholarship program, to its scientific-technical and service staff, who were part of my work, both during the laboratory time and the hours of writing in the office. Thanks to SINTEF and NTNU for hosting me during my pre-doctoral stay. They have, in addition to sharing their scientific knowledge, also given me the chance to live out exceptional experiences and meeting wonderful people, which all have filled out each of my days there.

And of course, I want to thank my family, for the miracle of their love which transcends time and distance. Thanks for believing in me. To my parents, Álvaro and Leidy; my siblings Darío and Wendy and my sister-in-law Karlita, for supporting each of my decisions, for the laughter and the shared sorrows, for making us feel close even with an ocean in between. Not a day has gone by without me feeling loved. Thanks to my grandmother, her husband, my aunts and uncles, for their blessing which accompanies me wherever I go. Thank you, Antonio, and Paqui, for opening up the doors to your home, for taking care of me, and for letting me experience Catalonia from the inside, for making me be a part of this place. I don't know what good I did for God in order to have you in my life.

Finally, thanks to the reader of this thesis, for the interest and curiosity which led you to open this text, I hope you will find the answers to your questions, and that it will represent the starting point of the development of your own research.

Barcelona, July 2023

Table of contents

List of Figures

List of Tables

List of Symbols

General parameters

Adhered volume	V
Applied load	P
Arithmetical average roughness	Ra
Arithmetical mean height	Sa
Developed interfacial area ratio	Str
Diameter	Ø
Experimental wear coefficient	K
Hardness	H
Hardmetal / Cement carbide	WC/Co
Hydrogenated amorphous carbon	a-C:H
Hydrogen-free tetrahedral amorphous carbon	ta-C
Indenter radius	R
Kurtosis	Sku
Length of the diagonal measured from corner to corner on the residual impression in the specimen	L
Load	F
Normal load	N
Parallel length	Lc
Parallel tensor to the burnishing path	σ_x
Penetration depth	h
Perpendicular tensor to the burnishing path	σ_z
Poisson coefficient	ν
Pressure	P
Pressure in the center of the contact region	p_0
Radius	R
Real plastic strain	ϵ
Reduced elastic modulus	E*
Root mean square height	Sq
Self-hardening coefficient	n

Skewness	Ssk
Specific adhesive wear rate	K
Speed	N
Stress	σ
Stress for unitary strain	K
Temperature	T
Ten-point height	S10z
Test distance	L
Test duration	t
Texture aspect ratio	Str
Ultimate tensile strength	UTS
Velocity	v
Vickers hardness	HV
Viscosity	η
y-axis numerical nodal displacement	Uy
Yield strength	σ_{ys}
Young's module	E

Abbreviations

Additive manufacturing	AM
American Society of Materials	ASM
Auger electron spectroscopy	AES
body-centered cubic	bcc
Ceramic-metal composite	Cermet
Chemical vapor deposition	CVD
Coefficient of friction	COF
Confocal scanning optical microscope	CSOM
Diamond-like-carbon	DLC
Electrical discharge machining	EDM
Electron backscattered diffraction	EBSD
Energy dispersive X-ray spectroscopy	EDX
Field Emission Scanning Electron Microscope	FE-SEM

Finite element model   FEM

Hexagonal close-packed   hcp

Incremental hole drilling   IHD

Metal matrix composites   MMCs

Micro hardness tester   MHT

Physical vapor deposition   PVD

Scanning electron microscopy   SEM

Surface integrity   SI

Transverse rupture strength   TRS

Tungsten carbide   WC

Vibration-assisted ball burnishing   VABB

Vibration transmission unit   VTU

Wire arc additive manufacturing   WAAM

X-ray diffraction   XRD

Chapter 1

Introduction

Continuous deformation processes, known also as forming process, are aimed at modifying the shape of an element of interest through plastic deformation, increasing its strength and improving its surface finish [1]. Friction affects the processes performance substantially. Hither, friction occurs in a high-pressure environment between a hardened tool and a soft workpiece that deforms plastically. When the coefficient of friction (COF) is large enough, adhesion occurs. Therefore, it is important to control the friction during the process since it can lead to the formation of residual stresses and defects due to a delayed metal flow, increasing the demand of forces, power, and tool wear, to finally deliver a product with little dimensional accuracy and countless defects [2].

Under these considerations, this work takes into account two plastic deformation processes: ball burnishing as a superfinishing process [3] and wire drawing as a bulk deformation process [2]. For ball burnishing, failure modes in forming and machining processes are modified by producing local plastic deformation on the metal surface in cold working conditions, by the action of a force that is transmitted through a penetrator (generally of spherical, conical, or cylindrical geometry). Successive, continuous, and adjacent passes are performed until cover the entire area of the part [4]. For wire drawing, metal flows plastically through a matrix giving it a certain shape, improving the mechanical properties and guarantee a good finish of the piece. Changes in their operational parameters, coatings [5] and lubricants applied in the tool-metal working interface [2] have been proposed as alternatives to modify the failure modes and surface finish involved in these processes.

This background reveals the importance of the configuration of these processes in the forming of stainless-steels and aluminum reinforced with nanoparticles, from a tribological point of view, where friction, wear, coatings, and lubrication play a relevant role, in order to achieve the accurate dimensions and proper surface finish in the final products while extending the tool service life.

1.1. Background and motivation

Friction is a phenomenon that has been studied since the 15th century, with Leonardo da Vinci as the pioneer in developing a systematic study of friction, on which modern tribology is based. Two centuries later, Guillaume Amontons, developed the laws of friction, later verified by Charles Augustine de Coulomb. During the 19th century, Arthur-Jules Morin introduced the term "coefficient of friction" as an empirical measurement determined experimentally to quantify the interaction between the parts of a system. In recent decades, research in this field has led to a better understanding of friction, so that through atomic manipulation, new materials and substances development, as well as the use of mathematical modeling software, knowledge has been enhanced to avoid waste of resources and tool wear caused by friction.

Along these threads, Tribology is one of the research lines in the Metallic and Ceramic Unit of the Research Technology Center of Catalonia Eurecat. In this research line, several works are conducted in order to determine friction and minimize the wear mechanisms produced due to the contact between the tool and the workpiece. On the other hand, the work of the Manufacturing Technologies research group (TECNOFAB) of the Universitat Politècnica de Catalunya, seeks the appropriate interaction of the tool-part to increase the surface integrity of the workpiece through burnishing.

Thus, research on the relationship between microstructure, material properties, applied loads, and surface conditions resulting from continuous deformation processes, takes a new approach by considering friction as a parameter to be determined and controlled for further processes optimization. Otherwise, reduced production efficiency with a very high economic impact, are the dire implications at the industrial level. Therefore, during the last few years, new materials have been developed and enhancements have been made to existing ones through alloys, tool materials, finishing processes, lubricants, and surface treatments (coatings and thermochemical treatments). Nevertheless, to increase the products surface quality and to extent the tool service life it is also necessary evaluating the behavior of the entire system from a tribological point of view.

Therefore, the first aim of the proposed thesis is to experimentally assess the friction effect and to identify the wear mechanisms in two industrially important continuous deformation processes:

1. Ball burnishing on stainless-steels
2. Wire drawing of aluminum alloys

In both processes, the final goal is to obtain an optimal surface integrity of the material processed to improve the mechanical performance of the final component. These processes are industrially relevant due to stainless-steels and aluminum alloys are materials highly applicable in aerospace and automotive industries. Then, the second target is an attempt to improve the surface integrity of the final components while extending tool life through the pertinent selection of loads, coatings, and lubricants for each case of study.

1.2.   Research contributions

The present dissertation has concentrated on the tool-part tribological interaction assessment for two continuous deformation processes, (1) ball burnishing as a superfinishing process and (2) wire drawing as a bulk deformation process. The tribological behavior implies the COF determination, the surface characterization conditions of the materials in contact as well as the resulting wear mechanisms assessment. In order to improve the process tribological behavior, it is necessary to modify the critical process parameters or to include coatings and lubricants within the contact by means of an experimental approach. Despite the different purpose of both processes (superfinishing and bulk deformation processes), their experimental approaches, in tribological terms, derives in a similar conceptualization and purpose, where the challenge is an optimal surface integrity of the components. Therefore, the present work derives in certain issues to be resolved.

1.2.1.   Previous questions

1.   How can COF be experimentally established to improve an industrial continuous deformation process?
2.   Can the effect of friction be evaluated by computer modelling? Can the factual friction tool-part interaction be introduced in a computer modelling to obtain a feasible industrial solution in terms of part surface integrity?
3.   How is the optimum COF established for each continuous deformation process, considering that the bulk production processes require a minimum value, while a minimum value may be ineffective for surface finishing processes?
4.   How can the effects of friction on surface integrity and tool performance be reduced in a continuous deformation process?

5.   Is it possible to enhance the surface integrity of the parts by controlling friction and reducing wear at the tool-part interaction by means of friction reduction strategies: materials, coatings and tool surface condition, lubricants, or process operational parameters?

1.2.2. Hypothesis raised

Under the previous questions, the hypotheses that drive the development of the research are presented below:

1.   A representative COF can be obtained through a proper design of the tribological test to reproduce the wear mechanisms of the continuous deformation process.

2.   Introducing the obtained experimental COF and the initial surface integrity of the part, a numerical solicitation of both, the part and the tool in continuous deformation processes, can be computed by means of integral numerical model.

3.   Through numerical modelling, it is possible to determine the COFs range, which optimizes the process in terms of tool-part surface integrity.

4.   The use of different tribology-based strategies such as coatings and lubrication during the tribo-contact, allows to optimize the COFs for different materials in order to satisfy their industrial demands.

5.   The reduction of wear in the tribo-contact entails an optimized COF. In this manner, it is possible to improve the finish integrity and the tool service conditions through wear mechanisms minimization.

1.3.   Objectives

The general target and the specific objectives set for this dissertation are presented in next sections:

1.3.1. General objective

Study and characterization of the tool-part tribological interaction for continuous deformation processes by means of experimental methods to optimize them, guaranteeing the surface integrity of the interacting parts.

1.3.2. Specific Objectives

1. Design tribological tests that reproduce the damage mechanisms observed in the material surfaces, in order to obtain reliable COFs values, representative for each sliding interaction.

2. Optimize the selected processes by defining sustainable tribological conditions, using different strategies such as: adjustment of process parameters, use of coatings and lubricants or their combination, considering besides the piece surface status, its microstructural nature, in order to extend the tool life and therefore, guarantee the final product quality.

3. Provide an experimental methodology that allows the validation of integral numerical models, where the tool-part interaction is considered, in order to conceptualize reliable and versatile numerical tools for future processes application.

1.4. Publications and Contributions in international congresses

Publications in JCR indexed journals

1. Torres, A.; Cuadrado, N.; Llumà, J.; Vilaseca, M.; Travieso-Rodriguez, J.A. Influence of the Stainless-Steel Microstructure on Tribological Behavior and Surface Integrity after Ball Burnishing. *Materials* 2022, *15*, 8829. https://doi.org/10.3390/ma15248829

2. Torres, A.; Amini, C.; Cuadrado, N.; Travieso-Rodriguez, J.A.; Llumà, J.; Vilaseca, M.; Experimental validation of ball burnishing numerical simulation on ball-end milled martensitic stainless-steel considering friction and the initial surface topography. *J. Mater. Res. Technol.* 2023, *22*, 3352-3361. https:// doi.org/10.1016/j.jmrt.2022.12.100

Contributions in international congresses

1. Torres, A.; Cuadrado, N.; Travieso-Rodriguez, J.A.; Llumà, J.; Vilaseca, M. Characterization of hardmetal dies used in wire drawing of steel and evaluation of their surface integrity after service life. *23rd International Conference on Wear of Materials and the 5th International Conference on BioTribology*, 26-29 April 2021, Online and On-demand (Poster presentation).

2. Torres, A.; Cuadrado, N.; Travieso-Rodriguez, J.A.; Llumà, J.; Vilaseca, M. Experimental Validation of Ball Burnishing Numerical Simulation on Ball-End Milled Martensitic Stainless-steel Surface Considering Friction and the Initial Surface Topography. *7th World Tribology Congress*, Lyon (France), July 2021 (Oral presentation).

Projects contribution

1. Ultrasonic-assisted ball burnishing tool, for super-finishing of parts, in a lathe (BRUVIT), Travieso-Rodriguez, J.A.; Jerez-Mesa, R.; Llumà, J.; Martínez, E.; Estévez, A.; Velázquez, E.; Marqués, J.; Torres, A. *Universitat Politècnica de Catalunya (UPC); Universidad de Sevilla (US),* funded by the Ministry of Science and Innovation of Spain, through grant PDC2022-133596-I00.

1.5.   Thesis dissertation in brief

The present dissertation is organized in 6 chapters. In **Chapter 2**, by means of an exhaustive bibliographic review, the state of the art developed within the subject is summarized in two main sections. The first part defines the tribological criteria that the selected continuous deformation processes follow, as well as the relevant techniques and parameters for their evaluation, and the second part describes the intrinsic characteristics of them (ball burnishing and wire drawing). Next, **Chapter 3** describes the methodological approaches for the tribological interaction assessment of the ball burnishing process on stainless-steels and during the sliding contact between the hardmetal tool and aluminum feedstock that constitute the fundamental interacting materials of wire drawing process. Then, subsequent chapters summarize the encountered findings during the experimental phase in terms of the tribo-interaction and surface integrity, their optimization, and partial conclusions.

In that sense, **Chapter 4** demonstrates the influence of the stainless-steels microstructure on the tribological behavior and surface integrity after ball burnishing. The results of this study show that the process parameterization from a tribological point of view (so far neglected) is markedly relevant, since the superfinishing varies depending on the microstructural nature of the steel components to be treated. Two stainless-steels, austenitic and martensitic, were tribologically evaluated, exhibiting highly contrasted surface responses to continuous

deformation under the same conditions. In this way, it was demonstrated that the friction values generalization for this interaction is a misstep and that, in order to achieve a surface that satisfies industrial demands, an adequate COF must be defined. Thus, this study represents the starting point for a parameterization methodology from a tribological perspective while providing experimental friction values that feed the integral numerical models of the process, i.e., that contemplate the totality of the variables that affect it. Additionally, this section provides the ball burnishing parameters for an optimal improvement of martensitic stainless-steel UNS S46500 surface integrity, not evaluated so far. This is followed by exposes the experimental validation of ball burnishing numerical simulation on ball-end milled UNS S46500 martensitic stainless-steel considering friction and the initial surface topography. With this work, the structured 3D ball burnishing numerical simulation applicability was demonstrated. This model configuration (previously established for ball – milled AISI 1038 steel surfaces) went further than other models, considering roughness, the initial residual condition and friction in its setup. This setup adapted to the tribological interaction between the hardmetal tool, and the martensitic stainless-steel surface overcame the limitations stated by a tailored finite element model (FEM) configuration for specific materials. In this way, the numerical 3D roughness parameters and the final topography have a convincing agreement with the experimental results, reproducing the detrimental effects of load and friction on the surface finish. Then, the numerical residual anisotropy showed the same experimental trend, with a fairly close fit in the residual stress tensor values. Thus, upon validation, the model was able to provide an approximation of the subsurface stress behavior, elucidating that friction, as a function of the applied load, is totally responsible of the onset of superficial degradation and to an early isotropic residual state. Therefore, this versatile model configuration represents a useful tool in the search of the best process setup, according to the component applicability.

Regarding the wire drawing process, **Chapter 5** summarizes the advances achieved in the processing of reinforced aluminum wire with titanium carbide (TiC) particles used in welding arc additive manufacturing (WAAM). It has been evidenced that the components manufactured with this technology present two disadvantages generated in the feed wire: cracking and porosity. The presence of TiC nanoparticles in the aluminum wire suppresses this cracking. The second problem must be solved during the diameter reduction process known as wire drawing. Since the porosity of the WAAM components is caused by the accumulation of hydrogen from the moisture in the oxide layer and impurities on the surface of the wire feedstock, it is mandatory that this continuous deformation process performs an optimal tribological

interaction during the pass of the wire through the die to reduce friction and adhesion effects (delayed metal flow, tool wear and part surface integrity degradation). Thus, this section proposes solutions to this new issue, starting from the characterization of the tribological interaction of the tool material (hardmetal) and wires (Al 1370 and Al-2%TiC), to the evaluation of diamond-like-carbon (DLC) coatings on the tool surface as possible solutions. The results showed that, in addition to crack suppression in WAAM components, the presence of TiC nanoparticles mitigates hardmetal wear and reduces in-process friction values, favoring lubrication. However, mitigation is not inhibition, so coatings, as protective layer of the material tool, take special relevance. Finally, **Chapter 6** synthesizes the outcomes and scientific contributions achieved in this research towards the final conclusions.

Chapter 2

State of the art

This section summarizes the state of the art, based on an extensive literature research of the selected continuous deformation processes as well as the tribological criteria that involves such industrial processes. The optimization of both ball burnishing and wire drawing processes starts from the numerical conceptualization of the tool-part interaction by means of the COF from which the understanding, analysis and improvement of these processes takes place. However, the variables that influence the friction behavior and its effects on piece integrity depend on the purpose of continuous deformation: superfinishing or bulk deformation. Thus, the engineering and science development takes a particular approach to each process. Therefore, the present state of the art exposes the shared concepts as well as the intrinsic characteristics of the selected processes constituting the starting point, in order to satisfy the novel industrial demands from a hitherto underestimated parameter: friction. Then, friction assessment in continuous deformation processes (ball-burnishing and wire drawing) and its effects in stainless-steels and aluminum surfaces, both highly relevant materials in industries such as aerospace and automotive, constitute another point of innovation in this scientific research.

2.1. Tribology criteria and methods

Tribology is the science and technology concerned with interacting surfaces in relative motion, including friction, lubrication, wear and erosion. The science and technology concerned with interacting surfaces in relative motion, including friction, lubrication, wear and erosion [6]. Wear, because of the contact deficiency, constitutes the main cause of components deterioration and the implicit failure of machinery operation. Likewise, friction is the principal cause of wear and energy dissipation. Some of this dissipated energy results in wear of the sliding surfaces and their eventual degradation to the point where replacement of whole components becomes necessary. Moreover, tool wear due to friction events have a direct result on the final quality of the manufactured component, in terms of surface integrity and mechanical performance. Therefore, wear mitigation through friction reduction strategies becomes critical to enhance industrial processes and final quality components. In that sense, the appropriate tribological

materials configuration, coatings, surface finishes and lubrication become energetically and economically relevant [75].

Considering that this study is focused on improving surface integrity of ball burnished and drawing materials, in order to improve the mechanical performance of the final produced components, this section begins defining what is considered as surface integrity and why is important to improve it.

2.1.1. Surface Integrity

Surface integrity is defined as the surface condition of a workpiece after being modified by a manufacturing process. The nature of a surface has a significant impact on the product performance, longevity, and reliability. Then, surface integrity not only refers to the topological aspects of the surface but also their physical, mechanical, metallurgical, chemical, and biological properties and characteristics (Figure 2.1).

Table 2.1. Different levels of surface integrity (SI) [7]

Minimum SI data set	Standard SI data set	Extended SI data set
Surface finish	Minimum SI data set	Standard SI data set
Microstructure (10 x or less)	Fatigue test (screening)	Fatigue test (extended to obtain
Microcracks	Stress corrosion test	design data)
Macrocrack indications	Residual stress and distortion	Additional mechanical tests
Plastic deformation		Tensile
Phase transformation		Stress rupture
Intergranular attack		Creep
Pits, tears, laps, protrusions		Other specific tests (e.g.,
Built-up edge		bearing performance, sliding,
Melted and re-deposited layers		friction evaluation, sealing
Selective etching		properties of surface)
Microhardness		

Typical surface alterations are plastic deformation, microcracking, phase transformations, microhardness, tears and laps, residual stress distribution, etc.

Taken this into account that a manufactured surface is not perfectly flat, the real contact area of the tool-part interacting surfaces is normally smaller that the apparent contact area due to its asperities. As a result, there is a COF generated during the tool-part interaction over a wide range of normal pressures. Due to the elastic contact deformation of the asperities, the actual contact area (and thus the friction force) increases with the normal pressure keeping the same friction coefficient as the ratio of the frictional and normal forces (stresses) [7]. On the other

hand, the presence of a lubricant layer between the tool and the manufactured part, significantly decreases the bonding forces in the contact and then the friction is reduced. For all the aforementioned, it is important to highlight the inseparable relation between friction reduction strategies and surface integrity quality and vice versa.

To guarantee an optimal surface integrity during a manufacturing process such as ball burnishing or wire drawing, an adequate surface finish (good roughness) and proper residual stresses (related with mechanical properties and microstructure) in the subsurface layer is needed [8]. The surface quality of a part is directly influenced by the stress conditions under which they were produced. Under high stress conditions, a low, poor, or suspect surface integrity is expected. When the design parameters that affect the processes remain stable during production, the surface quality of the workpieces is good, and their roughness are reduced [9]. For instance, the path of the different interactions that can be generated in the processes must be evaluated. One way to predict the final surface quality of a part or the tool life depending on the process parameters is numerical simulation. Nevertheless, these interactions depend on the constitutional characteristics, design, manufacture, and events raised throughout the tool life, so a path to the failure cannot be precisely defined [10]. Figure 2.1 represents a summarized workflow of the possible tool paths leading to failure.
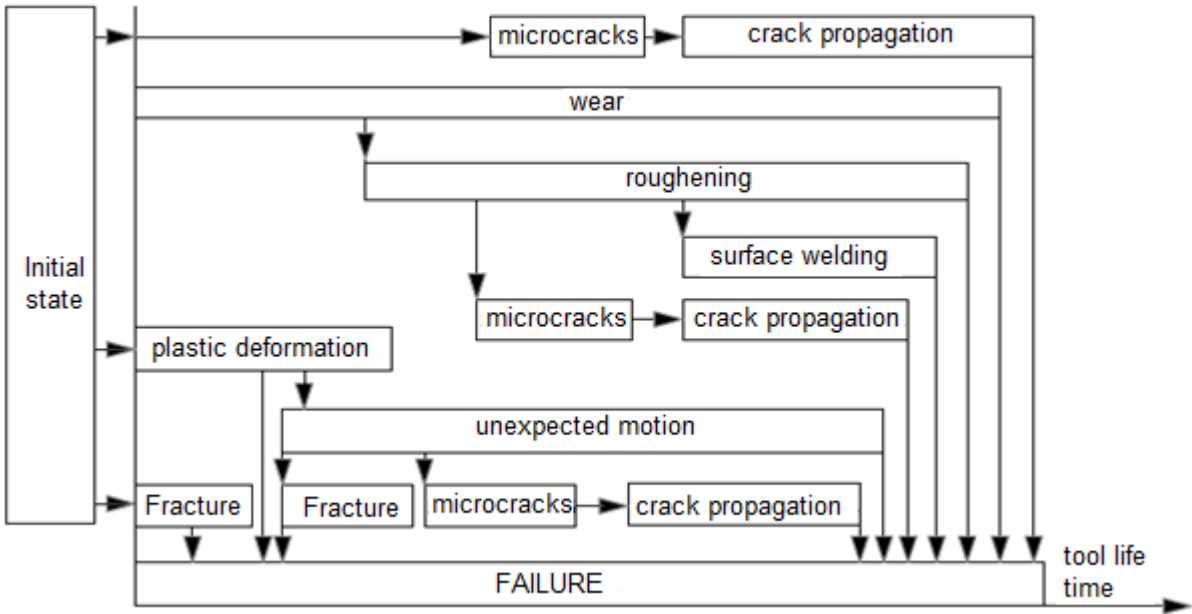
Figure 2.1. Tool path leading to failure [10]

One of the most considerable tool damages involved in manufacture processes is wear due to roughness of the interacting parts. Tool wear is capable of altering the tolerances and the quality of the surface finish of the final product, which can lead to a manufacture process reprocessing

11

stage and a replacement of the tool delaying the delivery of the final product [10]. Hence, surface texture and roughness conditions of the interacting parts must be known before, during and after wear mechanisms occur [11]. Surface texture refers to the irregularities (peaks and valleys) that a surface exhibits because of the manufacturing process. It includes waviness and roughness. Waviness refers to larger-scale variations in a surface that occur over longer wavelengths. It is a measure of the deviations from the nominal surface that occur at a slower rate than the roughness and is the widely spaced irregularities that are often produced by vibration in the processes; it is characteristic of the process itself, such as the grit spacing of a grinding wheel or the feed of a single-point tool. Roughness refers to the irregularities that occur over short wavelengths. It is a measure of the fine-scale irregularities that are smaller than the waviness wavelengths [11]. Figure 2.2 represents schematically the difference between roughness and waviness profiles in a surface.
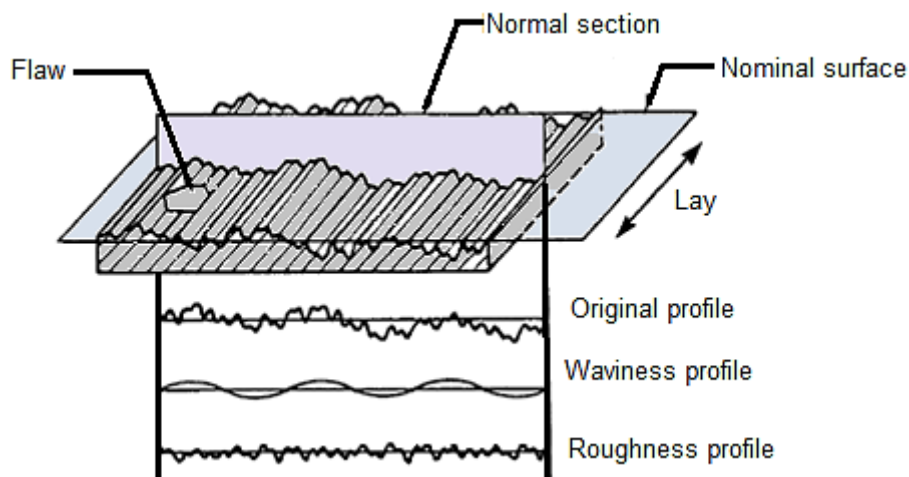
Figure 2.2. Roughness and waviness in a surface [12]

Several methods involved in the morphology, topography, and image analysis of engineered and worn surfaces have been developed as characterization techniques. An image is projected and scanned by a focused stream of electrons over a surface is usually acquired by Scanning Electron Microscope (SEM). This equipment excels above the optical microscope because of its large depth of field, that allows focusing on a large part of the specimen to at one time. The SEM also has greatly higher resolution, so closely spaced samples can be magnified to much higher levels. Since the SEM uses electromagnets instead of lenses, more control over the magnification level is allowed. Confocal scanning optical microscope (CSOM), that can produce three-dimensional images of samples in high-resolution, with a short depth of field, eliminating the out-of-focus glare, is another technique for surface topography evaluation. It is connected to an image analyzer to allow quantitative measurements of surface topography, both

12

in lateral and vertical dimensions. CSOM technique allows both surface roughness measurements as well as subsurface structure imaging and characterization [11]. Nevertheless, although their great advantages, these techniques are limited mainly by their complexity, environmental conditions sensitivity and cost.

As explained at the beginning of this section, one of the surface alterations due to the tool-part interaction that involves surface integrity is residual stress. Residual stresses are induced by the tool-part tribological contact in the sub-surface layer of the manufactured part and can be detrimental or beneficial for the mechanical performance of the manufactured part. To compute the effect of residual stresses there are two methodologies: destructive detection methods and non-destructive testing methods. Figure 2.3 show a brief classification of specific measurements methods. The principle of destructive methods is to remove some or all of the materials (mechanically or chemically), measure the strain or displacement of a specific area, and according to mathematical inversion of residual stress is performed for specific boundary conditions. Non-destructive methods are based on physical properties of the materials. In any case, residual stress is indirectly measured from strain, displacement or distortions in the lattice parameters [13].
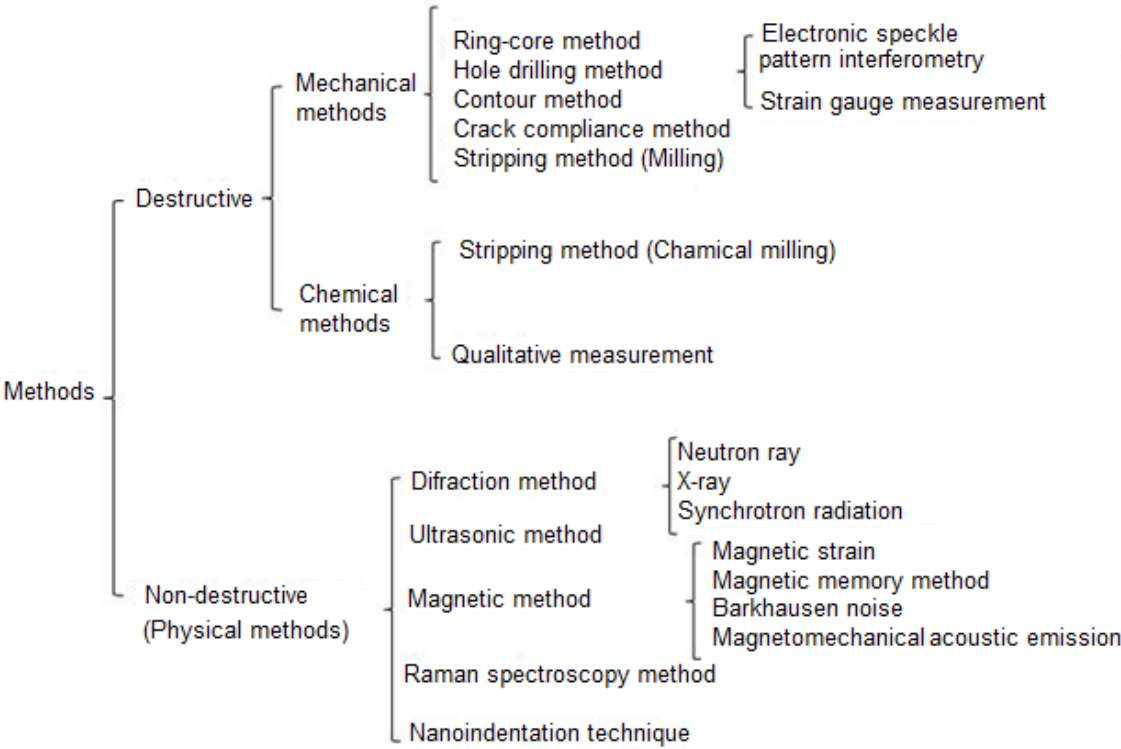
Figure 2.3. Classification of specific residual stresses measurement methods [14]

The most common non-destructive methods are Diffraction methods (x-ray, neutron, x-ray synchrotron radiation), Ultrasonic [15] and Acoustic wave propagation [16]. When the Bragg diffraction occurs, the diffraction peak is moved due to the residual stress, and the value of this residual stress can be computed mathematically form the peak shift. Ultrasonic stress measurement is based on the theory of acoustic elasticity, using the phenomenon of acoustic birefringence in stressed materials. Acoustic wave propagation is based on the variations in the velocity of the ultrasonic waves in stressed materials. A proper selection of these techniques allows quantifying, the residual stresses induced by the manufacturing processes. Therefore, the effect of friction on the surface integrity quality of the produced part can be computed and improved by means of friction reduction strategies.

2.1.2. Friction

Friction is a force that resists sliding and is defined as the resistance to movement of one body over another. It is commonly represented by the COF that is the ratio between the friction force (F) and the normal load (N):

$$COF = \frac{F}{N} \qquad\qquad (1)$$

The COF typically ranges from 0.03 for a very well lubricated bearing, to 0.5 to 0.7 for dry sliding, and even greater than 5 for clean metal surface in vacuum [11]. The fundamental experimental laws that govern friction of solid bodies are quite simple and are usually named for Coulomb who formulated them. These general laws are quoted as follows [11]:

- Static friction may be greater than kinetic (or dynamic) friction.
- Friction is independent of sliding velocity.
- Friction force is proportional to applied load and it is independent of contact area.

However, for many instances, these laws break down [11]. Friction force is generated by numerous mechanisms; thus, it is not a unique materials property. Friction depends on measuring conditions, surface roughness, presence or absence of oxides or adsorbed films, etc. Then, there are several effects because of friction to be considered within a tribosystem. Figure 2.4 shows a summary of these interactions.
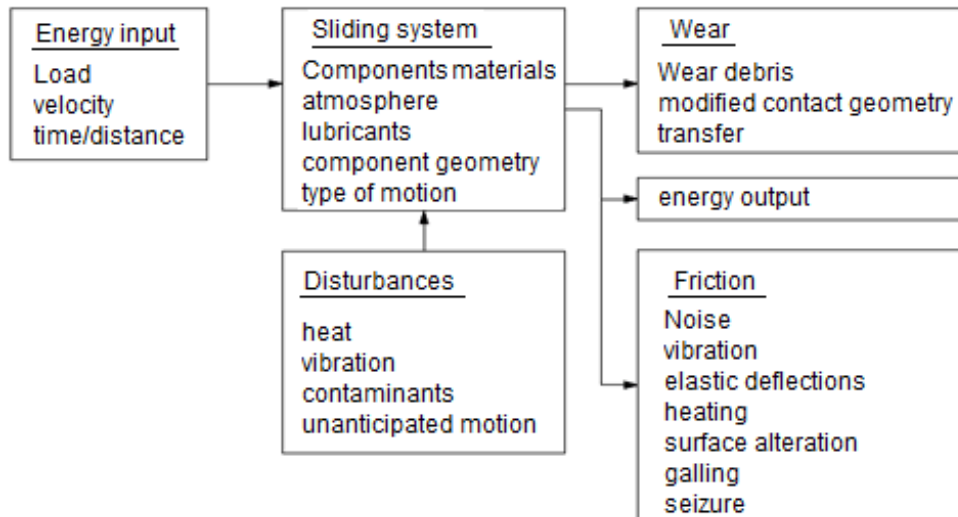
Figure 2.4. Systems approach for analyzing friction problems [11]

Because so many mechanisms are involved in generating the friction force during sliding contact, several strategies can be adopted to prevent or reduce it: influence of the tool-part geometry and roughness, operational process parameters, lubrication, tool coatings, etc. Hence, it is evident that friction can be altered by modifying any of them. For instance, if the roughness of the surfaces is considerably high, it can produce mechanical blockage even in lubricated conditions [11]. In that sense, in this section two of the most used industrial solutions to optimize friction and reduce wear in manufacturing processes are presented:

- Lubrication
- Tool coating

2.1.2.1. Friction under lubrication conditions

In general, lubrication is the control of friction and wear by the introduction of a friction-reducing film between moving surfaces in contact. When a layer of lubricant separates two materials enough, the COF of the system is essentially the COF of the fluid, whereas if there is partial contact between the parts, this coefficient corresponds to a combination of the properties of the fluid and the interacting surfaces [11]. In that sense, the Stribeck curve (Figure 2.5) shows that friction in fluid-lubricated contacts is a non-linear function of the contact load, the lubricant viscosity and the lubricant entrainment speed. In a tool-part lubricated interaction, the Stribeck curve shows the relation between the Hersey number, a dimensionless lubrication parameter, and the friction coefficient by equation (2) [11]:

$$Hersey\ number = \frac{\eta \cdot N}{P} \qquad (2)$$

15

Where η is the viscosity, N the speed (N) and P the pressure.
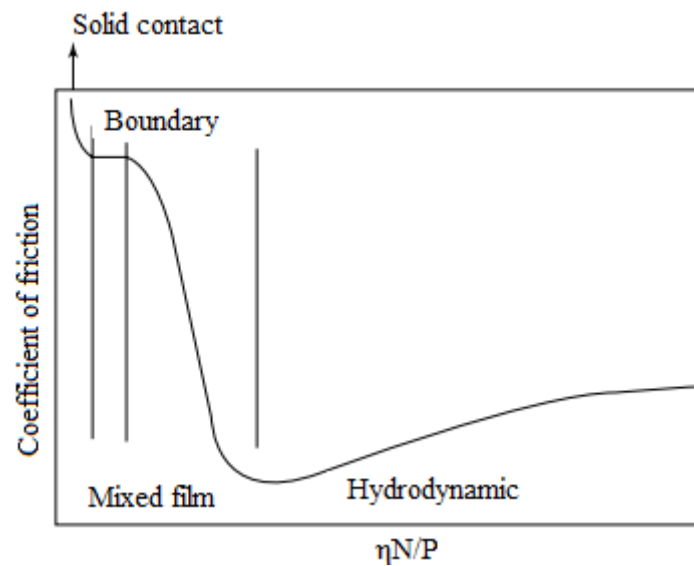
Figure 2.5. Example of a Stribeck curve for determining the COF from lubricant properties

The nature, topography, and composition of the surface layers may be important also under lubricated conditions. The lubricant should maintain the micro-geometric interaction between the tool and the part to reduce the effect of bonds during sliding (due to the roughness between surfaces) [17]. The correct selection of the lubricant will depend on the manufacturing process, working temperature, chemical reactivity with the tool and working metal, toxicity, ease of application and cost [2]. An improper lubricant selection leads to a change in the friction conditions and, therefore, to the variation of the contact speed, the tangential and normal stresses, the surface temperature conditions and the contact pressure, all these conditions different from the established in the process design, generating wear mechanisms as well as thermal fatigue [10].

2.1.2.2. Friction & coated systems

The use of coatings is widely used as an industrial solution to reduce friction and wear. In tool-part tribological contacts, tools are coated, conferring to their surfaces new and improved tribological properties. The application of coatings over the tool surface entails enhanced life service, mechanical properties, tribological performance and even generate an improvement of the surface integrity of the manufactured part. In general, ball burnishing tools and wire drawing dies are usually coated by vapor deposition processes. In that sense, vapor deposition process can form a thin coating layer on a substrate by condensation: Physical Vapor deposition (PVD)

or by chemical reaction of the gas on the substrate surface: Chemical vapor deposition (CVD) [2].

PVD is a process that converts the coating material into steam within a vacuum chamber and then condenses as a thin layer on the surface of the part [2]. Three subcategories of this process are distinguished: vacuum evaporation, sputtering and ion plating. Application of each of them will depend on the material to be applied. Thus, for Ag, Al, Au, Cr, Cu, Mo, W vacuum evaporation is used with low-cost equipment but does not guarantee good adhesion like the other two processes (sputtering and ion plating). For Al_2O_3, Au, Cr, Mo, SiO_2, Si_3N_4, TiC, TiN, sputtering provides better throwing powder and coating adhesion but is more difficult to control the process than vacuum evaporation. Ion plating is the best coverage and coating adhesion process for the previous materials but is most complex process control than sputtering [2]. For cold bulk metal forming, there is a coating method very efficient to increase the tool life: Hard coating by plasma – assisted PVD technology [18]. According to a statistical evaluation based on the observation of micrography, the modes or mechanisms of tool failure are altered by modifying the manufacturing processes of the tool followed by the application of a surface coating like PVD, increasing its lifetime up to six times more. Applying the Weibull analysis to a particular case, an unaltered tool performs 72 000 operations, but once modified it reaches 465 200 operations [19].

During the CVD, interaction occurs between the hot surface to be coated and a gas mixture, causing chemical decomposition of some of these gases that leads to the formation of a solid layer on the substrate. Reactions occur by the addition of heat, ultraviolet light or plasma. CVD includes high ranges of temperatures and pressures, and it is used in the coating of carbide tools and other parts where high resistance to wear, corrosion, erosion and thermal shock is important. The main advantages of CVD are grain size control, no vacuum chamber is required, and it produces a good bonding of coating to workpiece surface. Its disadvantages involves that they require a closed chamber with pumping and disposal equipment due to gas toxicity, low material utilization and reaction elements can be expensive [2]. There are countless conditions where it is necessary to use coatings to avoid friction, wear of the tools or the material transfer between the tool and the part that can cause scratches and subsequent cracks in the formed material [18].

In the search of industrial solutions, in this thesis, different types of PVD coatings for tools have been studied, involving two types of DLC coatings. The DLC coatings are a mixture of

diamond (sp3) and graphite (sp2) and are divided into hydrogen-free such as hydrogen-free tetrahedral amorphous carbon (ta-C) and hydrogenated such as amorphous hydrogenated carbon (a-C:H), the latter being of main interest due to their high wear resistance and low friction [20]. Analyzing tribological and surface properties of these PVD coatings by means of different techniques: ball-on-disc test, SEM, energy dispersive X-ray spectroscopy (EDX), Auger electron spectroscopy (AES) and light interference profilometry, it was observed that the behavior of DLC coatings depends on the material with which it interacts [20].

Therefore, the coating of the tool in a deformation process is a critical parameter so that the presence of an inadequate surface roughness as well as the interaction of its components with the components of the part must be considered [20]. For instance, and according to previous research, by coating the dies of aluminum deep-drawing with DLC coatings, dies improve the non-stick properties for aluminum, as long as use oil-lubricated conditions [21]. Thus, in this thesis coatings are an important parameter to take into account to improve surface integrity of the part as well as to enhance tool service life.

2.1.3. Wear mechanisms during continuous deformation processes

Friction influences the continuous deformation processes performance extensively as friction strikes in a high-pressure environment. Thus, friction leads to wear that can be defined as the progressive loss of material resulting from the mechanical interaction between to contacting surfaces, generally in relative motion. Under excessive COF values, adhesion and its subsequent effects occur [2]. Adhesion is caused in sliding contacts due to large atomic bounding forces at the surface asperities, the strong atomic bonding initiates the removal of the material from one of the surfaces due to the higher strength in the bonding (Figure 2.6 a). The plastic nature causing the local welding between the materials roughness leads to the generation of wear particles that interact in the process since the force to overcome these unions increases, causing greater resistance to movement and consequently increasing friction. This process is known as abrasive wear (Figure 2.6 b) [22].
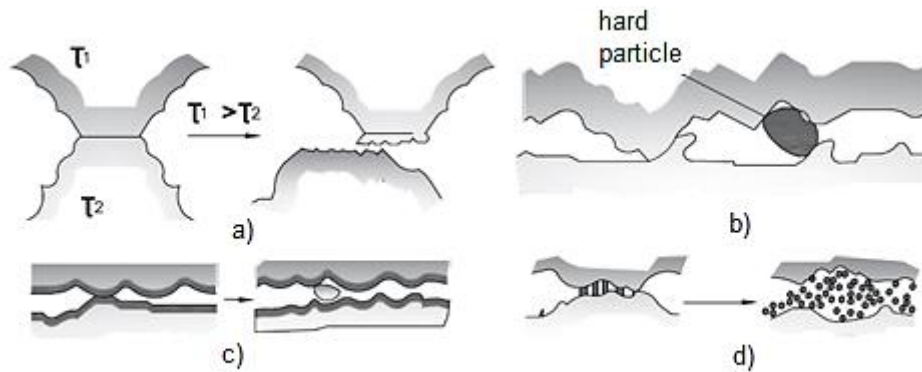
The basic wear mechanisms are a) adhesive, b) abrasive, c) fatigue, d) chemical wear

Figure 2.6. Wear Mechanisms [19]

Abrasive wear has four stages [23]:

- Micro-plough: The material is located in front of the abrasive particle forming a groove.
- Micro-cut: If the abrasive particle releases material of the same volume as the groove generated.
- Micro-fatigue: When the micro-cut is repeated several times on the surface of the material.
- Micro-crack: Originated in the high concentrations of stresses on the fragile surface.

The abrasive wear mechanisms can be seen in Figure 2.7 when an indenter slides on a metal piece without lubrication:
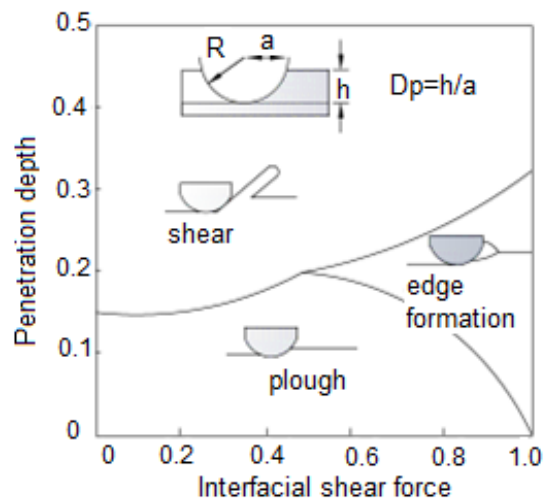
Figure 2.7. Abrasion Wear [24]

The literature denotes two basic modes of abrasive wear (Figure 2.8) :

- Two-body abrasive wear: caused by particles embedded or attached to some opposing surface.

- Third-body abrasive wear: caused by particles which are free to slide and roll between two surfaces.

a) Two-body abrasive wear   b) Third-body abrasive wear
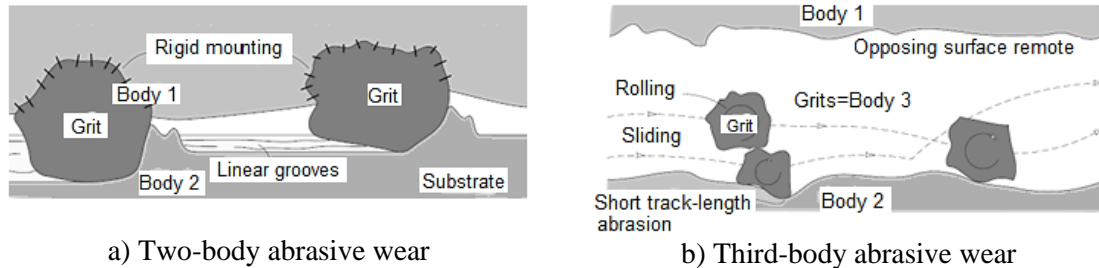
Figure 2.8. Two and three-body modes of abrasive wear [25]

Other wear mechanisms involved in the continuous deformation processes are fatigue and tribo-chemical wear (Figure 2.6). The first one begins from the cracks and fissures initiated on the material surface, as a result of the strain-induced on the surface due to conditions as sliding or rolling on the quoted surface [26]. The latter one is produced due to the mechanical and thermal interaction that occurs between the surfaces, then new wear particles can be generated. An example is the tribo-oxidation, where, due to environmental effects and high temperatures, adhesion particles can oxidize. In this manner, the formation of protective films by the interaction between surfaces of certain metals [22] can happen.

In the literature exists different predictive models of wear to quantify the wear losses in a particular process to contemplate good operability. For instance, regarding the wire drawing process, if the part is not positioned correctly to pass through the die or rows, friction and the multi-axial stresses will increase in certain areas of the tool and consequently the fracture wear mechanism will take place. With the aim to compute and vary wear rate, several authors are dedicated to predicting wear in industrial processes. A simple model to describe sliding wear is the Archard model. In this model an empirical equation based on contact mechanics is developed to quantify wear losses. The Archard equation is a function of the incremental volume:

$$dV = K \ (dP \cdot dL \ /H) \tag{3}$$

Where P is contact pressure, L is the test distance, H is hardness of the worn part and K is an experimental wear coefficient influenced by variation in wear conditions (temperature, environment) [27].

Then, to overcome the quoted wear mechanisms, the causes of the damage must be observed and discussed, eliminating unsuspected phenomena, to finally take action concerning the process, improving tool materials and lubricants [19]. Accordingly, in this thesis innovations are found to maintain the surface integrity of both the tools and the parts by controlling the mean parameter interaction: Friction.

2.1.3.1. Tool wear mechanisms in wire drawing dies

In the wire drawing process, the cross section is reduced by forcing the wire through a series of dies. The drawing die is the most critical part, because it gives the final shape of the wire. In the wire drawing process, the die angle, coefficient of friction, and area reduction have a major influence on stress inhomogeneity and the wire quality as well as die wear [28]. Die wear is the predominant factor affecting tool life in the deformation process, moreover, is a key factor to achieve an optimal surface integrity of the finished parts. Dominant factors influencing die wear are the wear coefficients between the die and the wire, the surface pressures of the dies, and the relative length movement between the die and the wire [28]. The most common failures modes in tools during cold forming processes due to die wear are shown in Figure 2.9. Additionally, the anisotropic properties of the tool materials also affect its useful life and are influenced by the reception and service conditions [8].
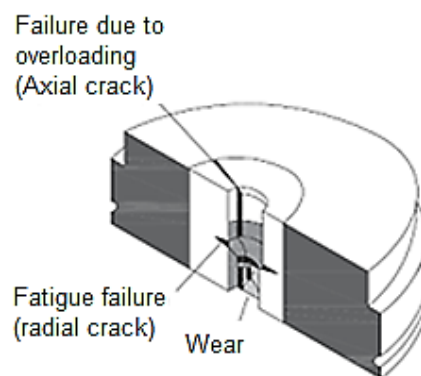
Figure 2.9. Typical locations of failures and their location in a die tool [29]

In wire drawing dies, fatigue as a wear mechanism, manifests itself with the presence of cracks that will cause breakage after a defined number of cycles. If there are indentations, irregularities due to the machining process and inclusions, the cracks are superficial. Its propagation depends on contact geometry, elastic and plastic properties of the materials and the magnitudes of the applied loads. Another factor to consider is the pressure with which lubricant is applied as well as its viscosity, since if it is very high, will not flow into the surface crack. Subsurface cracks will be caused by crystalline defects and inclusions. When they propagate parallel to the surface,

delamination occurs [22]. Therefore, a proper relationship between the applied stress and the anisotropy of the material becomes increasingly important.

Regarding lubrication conditions, die wear will be affected by them since it determines mainly the contact time between the part and the die, the friction coefficient and the contact pressure during drawing. Then superficial cracks due to die wear can be prevented or even eliminated using appropriate lubrication strategies.

2.1.4. Friction Tests and Simulative Tribotesting

Systems with interacting surface in relative motion are tribological systems. They interaction diagnosis is carried out through laboratory test configurations and test specimens, taking into account that friction and wear must be related to the entire system of interacting components, materials pairs and interfacial lubricants. The main parameters are the specimen geometry, composition and microstructure material and the operational parameters such as load, stress type, deformation velocity and temperature, environment, motion of a material/material pair (dry system) or a material/lubricant/material combination (lubricated system) [11]. Currently, the most used experimental methods to evaluate friction and wear damage effects are: pin on disc/plate, cylinder-on-cylinder and load scanning [30].

To design friction and wear experiments is important to define objectives of the tribotesting to be performed. The scope of tribotesting can be classified into the following primary areas:

- Evaluation of the function, performance, maintainability, reliability, life, or efficiency of engineering tribosystems or tribocomponents
- Quality control of tribocomponents
- Characterization of the tribological behavior of materials and lubricants
- Investigation of basic tribological processes and friction-induced energy losses or wear-induced materials losses [11].

According to DIN Standard 50322: 1986-03 [31], tribotests can be grouped into six categories depending on the structure and function:

- Machinery Field Tests
- Machinery Bench Tests
- Systems Bench Tests

- Components Bench Tests
- Model Tests
- Laboratory Tests

In the same sense, the American Society of Materials (ASM) Volume 18: Friction, Lubrication and Wear Technology [11] establishes a sequence for laboratory friction and wear designing:

1. Choose a proper test arrangement for the test specimens of triboelement (1) and triboelement (2), specifying the geometry of the test configuration, characteristics and properties of the materials, and surface characteristics (clean surfaces before test).

2. Characterize the interfacial element (3) (e.g., lubricant) and the environmental atmosphere (4) in terms of their chemical nature, composition, and physical properties.

3. Select an appropriate set of the operational parameters, involving motion type, load (N), velocity (v), temperature (T), and test duration (t)

4. Perform the tests as functions of modified structural parameters of the triboelements (e.g., hardness, roughness) and operational parameters (e.g., load cycles, speed variations). The conditions of the tests, such as the time dependence of operational parameters, ought to be controlled by suitable detectors or sensors and supported by on-line computer techniques.

5. Determine interesting tribometric characteristics, like friction, wear, tribo-induced acoustic quantities (noise or vibrations), and tribo-induced thermal quantities (e.g., friction-induced temperature rise).

6. Characterize the worn surfaces of triboelement (1) and triboelement (2) with regard to surface roughness and the composition and structure of that surface.

Mathematical models, computer simulations, and statistical techniques are essential for the development of these tests [11].

In that sense, an approximation that constitutes a starting point of the tribological test design for sliding interaction assessment is the classical Hertzian theory of non-adhesive contact. In this thesis, the first interaction between a ball and a plane surface have been approximated to the classical Hertzian theory of non-adhesive contact [32]. The pressure in the contact region center (p_0) is determined as a function of the applied normal force (F), the radius of the indenter (R), and the reduced elastic modulus (E*), according to the normal contact between a rigid sphere and an elastic half-space Equation (3):

$$p_0{}^3 = 6F \cdot E^{*2}/\pi^3 \cdot R^2 \qquad\qquad (4)$$

Where E* is defined by the Young's modulus (E_1, E_2) and the Poisson coefficient (ν_1, ν_2) of the interacting materials, in agreement to Expression (4):

$$1/E^* = [(1-\nu_1{}^2)/E_1] + [(1-\nu_2{}^2)/E_2] \qquad\qquad (5)$$

With this premise the contact pressure of the continuous deformation processes studied, ball-burnishing and wire drawing, have been approximated to be used in the design of the laboratory tribological tests.

2.2. Continuous deformation processes: study cases

A continuous deformation processes is one in which the shape of a metal piece is modified by plastic deformation, thus materials used in continuous deformation require a moderate level of ductility to enable plastic deformation with no fracture. The deformation is induced by an external force that exceeds the yield strength of the material, improving among other its surface integrity or mechanical properties[1]. In these processes, the tools, matrices, or dies used are subjected to great stresses transmitted by the metal formed from the piston, punch or traction system that exerts the deformation loads [1]. When stresses are excessive high, friction increases, and adhesion or other damaging wear mechanisms occur. Thus, unconscionable friction leads to a detrimental piece surface conditions with undesired residual stresses and defects that delay the metal flow. This material backlog demands a power increment while the tool wear arise, delivering defective and dimensionally inferior products [2]. Based on these factors, two metal forming operations have been considered in the framework of this thesis: ball burnishing and wire drawing.

2.2.1. Ball burnishing process

Burnishing is a process that modifies the finish of a surface through precision metal finishing tool. This tool smooths metal peaks over valleys in the surface without removing metal from the part. Under regimes of high fatigue, turbine blades, pistons, landing gears, molds, lasting valve seals, shafts for pumps and bearing bores components [33,34] suffer cracking on their machined surfaces, which can be avoided with the application of an appropriate finishing

treatment. Thus, the literature proposes the use of burnishing, as the last machining operation [35-38], in the search of less rough and harder surfaces compared to other processes such as electropolishing, shot peening or laser shock peening [39]. During burnishing, a cylindrical or spherical indenter that can rotate, transmits a load while displacing on an irregular metal surface [35]. This procedure confers extra mechanical properties on the treated parts, reducing execution times [36,40-42] and avoiding extra machining costs [35,36,38]. Properties such as strain hardening are amplified on the treated metal surface due to plastic deformation prompted by the displacement of the indenter at a given pressure [36,40]. In this manner, burnishing improves the surface integrity (roughness. residual stress state, hardness, microstructure [9,38]), reliability, and service performance [43] by inducing surface [37,44-48] and subsurface residual stresses [35,37,49-52]. Consequently, wear, corrosion, and fatigue resistance are enhanced due to the newly induced residual compressive state [35,37,40,41,44,49,53,54]. However, to achieve these advantages, process (overloading) and material limitations (loss of ductility) [55], which depend on the microstructure [35,56,57], must be overcome by using a satisfactory configuration [4,33-35,55,58].

Burnishing proceeds by crushing the surface irregularities generated by machining with a rotating cylindrical or spherical indenter. The indenter is free to rotate about its axis and is pushed and translated against the machined part and along the material surface. Thus, burnishing mechanics is based on the tear-shaped region formation on the material surface generated in front of the indenter in its displacement. This tear-shaped region is composed by three zones: (1) engagement, (2) plastification, and (3) superfinishing, as shown in Figure 2.10. In the engagement zone starts the elastic deformation, then in the plastification zone, the yield strength of the material is exceed involving plastic deformation of the surface peaks and valleys. Finally, in the superfinishing zone the indenter is in longer contact with the surface.
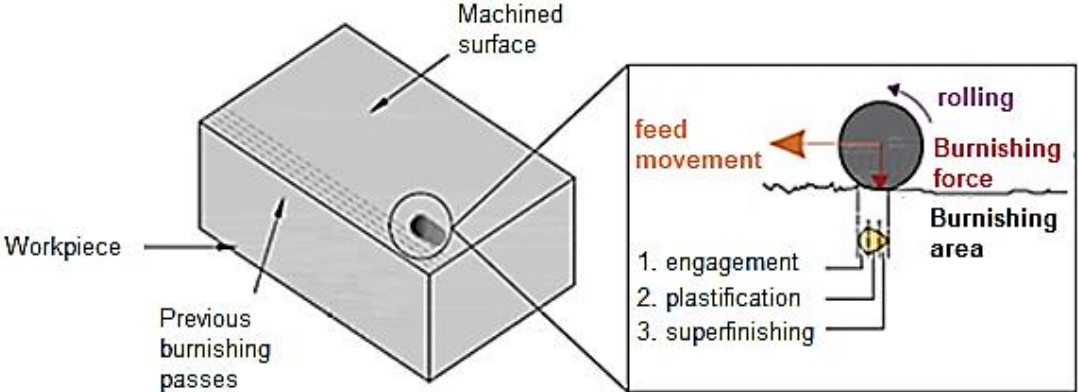
Figure 2.10. Working area of burnishing set-up [39]

Without considering the loss of intermittent contact due to the rotating movement (without affecting the result), the surface is compressed, plasticized, and finally cleaned until a final surface finish while the contact and the stresses are gradually dissipated. The main effect occurs in the central area of plasticization, where peaks and valleys become plastic. The flow is induced along the lines of least resistance on both flanks of the bulges, filling the depressions when two opposite flow currents meet at the bottom [4].

Burnishing processes can be enhanced varying operational parameters, especially the shape of the indenter and the force regulation method [39]. Regarding the burnishing tool, it must be attachable to a specific machine, capable of resisting the preload, guaranteeing the mechanical engagement between it and the part. Its free movement while maintaining the mechanical integrity also is required [59]. Thus, the indenter can be a ball type or roller type tool. Therefore, innovative special configurations have been developed to improve the process, as shown in Figure 2.11.
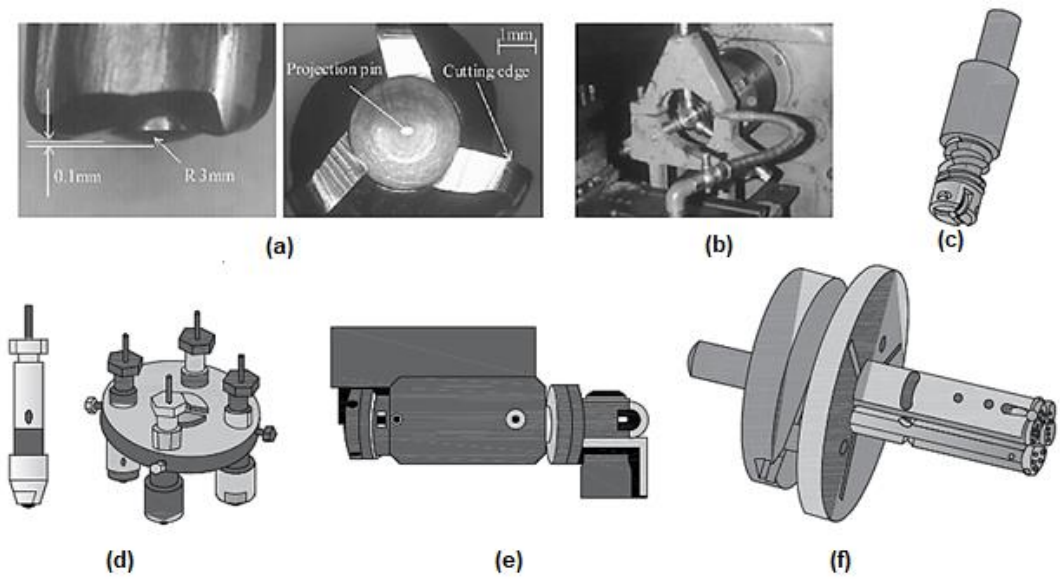
Figure 2.11. Special burnishing tool configurations. (a) Milling & burnishing tool [65], (b) Center rest multi-ball tool [66], (c) Multi-roller tool [67], (d) Multi-ball tool [65], (e) Adjustable roller tool [68], (f) Multi–ball tool [69]

Regarding the shape of the burnishing indenter, its geometry and configuration will determine the way through the force is transmitted and controlled to the part. When a ball type tool is used, burnishing is characterized by low radial loads, low feeds, and almost absent rolling friction and sliding, adapting to several shapes. In contrast, roller indenters are not versatile because they cannot treat complex surfaces [4].

The force regulation method constitutes one of the most important parameters in the process efficiency in terms of induced compressive state in the subsurface layer and surface roughness [36,31,70-72]. Under this load effect, a maximum compression state is induced in the subsurface (at 100 μm depth [1]) within the affected layer thickness [70,73] (up to 300 μm on 15-5 PH martensitic stainless-steel turned surface [74]), while roughness peaks shift to valleys [74]. In that sense, in the literature is reported that other burnishing parameters such as speed [69,70,75], feed [70,75] and number of passes [64,70] have a scare influence on the final residual stresses state.

The burnishing force is the normal force transmitted by the burnishing tool to the part surface. The transmission of this force could be controlled according to the mechanisms shown in Figure 2.12.
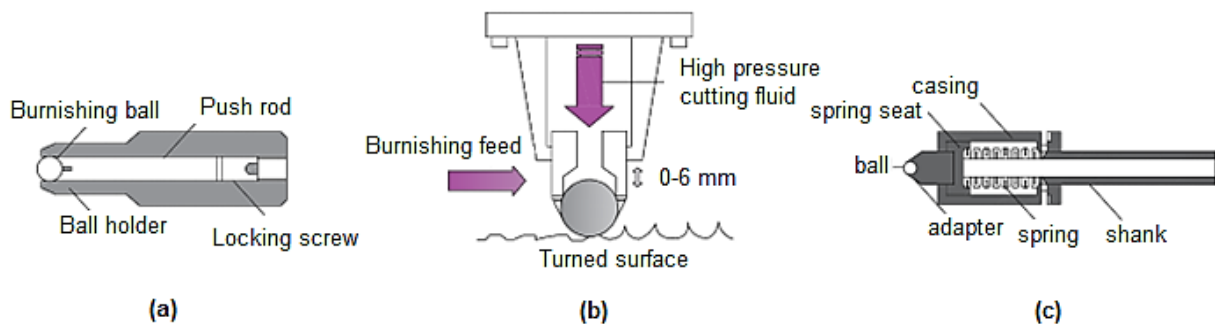
Figure 2.12. Force regulation systems in classical burnishing tools.
(a) Depth-of-penetration tool [76], (b) Hydrostatic tool [4], (c) Spring-regulated tool [77]

Jerez-Mesa et al. [61] incorporates ultrasonic vibrations into the burnishing tool to improve the surface integrity of the parts. The phenomenon of acoustoplasticity or Blaha effect minimizes the quasi-static stress necessary to deform the material due to the simultaneous propagation of waves inside the material, entailing a residual hardening effect, and superimposing an oscillating force on the preload established for a static burnishing process. According to the patent developed in the Polytechnic University of Catalonia [78], the mechanism works according to a compression spring that regulates the preload, offering a constant balancing of the ball and it is interchangeability in different machining tools. The electrical part is isolated from the medium and transmits to the ball the vibratory movement caused by the alternative change of piezoelectric thickness. Figure 2.13 shows the vibration-assisted ball burnishing (VABB) tool.
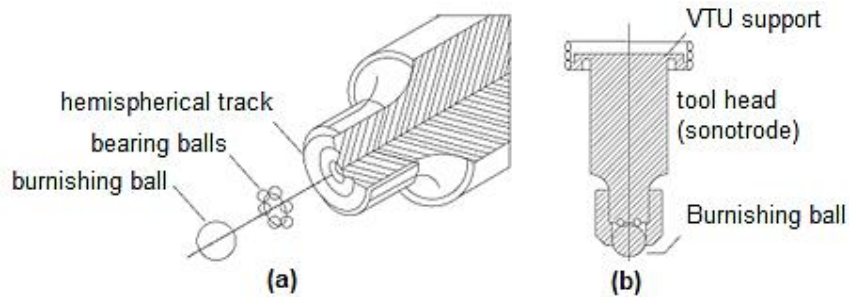
Figure 2.13. Schematic representation of the force transmission unit.
(a) Detail of bearing balls on hemispherical track machined on the sonotrode tip,
(b) Assembled section of vibration transmission unit (VTU) components [39]

With these precedents, several authors have worked on obtaining analytical [38,52,54,64,70,79, -81] and numerical models [36,38,64,71,79,82-84], of surface finish and residual stress state from experimental data [4]. For instance, E.g., Zhang et. al. [52] established an empirical method to estimate the roughness and residual state from pressure, velocity and feed rate process parameters on 17-4 PH martensitic stainless-steel surfaces, obtaining a qualitative fit for the stress state. Li et. al. [79] determined constant coefficients within the process to predict the roughness behavior as a function of yield strength. El-Tawel et al. [64] and Jerez-Mesa et al. [81] based their studies of the roughness imparted by burnishing (on brass and AISI 1038 steel surfaces, respectively) on the Taguchi method. Travieso et al. [54] and Avilés et al. [80] have implemented a predictive analytical method for the fatigue behavior of burnished AISI 1038 and AISI 1045 steel surfaces with relevant fittings. Garcia et al. [49] measured residual stresses using the incremental hole drilling procedure (IHD) with the intention of establishing a FEM model to obtain the strain release equations using IHD. Additionally, several experimental studies have been customized according to specific material surfaces states. Thus, Dzierwa et al. [70], Loh et al. [50], Świrad et al. [85] and Aviles et al. [80] have analyzed the effect of a set burnishing configuration on the surface finish, while Abrao et al. [48], Chomienne et al. [35], and Luca et al. [44] have experimentally assessed the influence of different configurations on the residual stress behavior.

Regarding FEMs, they are adapted according to each particular condition, meaning that one model is not applicable to all cases [79]. Thus, Rodriguez et al. [38] proposed a 2D simulation in order to obtain the magnitudes of residual stresses introduced by hydrostatic ball burnishing on an AISI 1045 steel surface, with quantitative divergences. On the contrary, the models of Rao et al. [71] approach the experimental values of residual stresses induced by burnishing on aluminum surfaces with a variation of less than 10%. Additionally, the 3D model of Balland et al. [36] on 11SMn30 surfaces showed a ridge flow in agreement with the experimental results

obtained by Barquins et al. [82]. Then, Sayahi et al. [83] programmed a 2D and 3D ball burnishing model to validate the numerical results with experimental residual stresses acquired on Ti-6Al-7Nb surfaces, demonstrating higher accuracy in their 3D setup. In contrast, Yen et al. [53] configured a 2D model on AlSl 52100 steel showing a better fit in terms of residual stresses with respect to the 3D configuration. However, this 3D model reproduces the material flow and surface deformation in a more representative way. Additionally, Kermouche et al. [86] by their model on AISI 52100 steel, simulated the contact severity where the friction coefficient and the hardness of the piece constitute the key parameters of the process. Later, Maximov et al. [84] approximated the tool displacement to a sequence of planar movements on a modeled roughness surface, so that the flow stress and the coefficient of sliding friction were obtained numerically. In this regard, the ball - rough surface interaction during the ball burnishing has been numerically addressed by 2D simulations by several authors. Consequently, Amini et al. [37] developed a structured 3D FEM taken into account the initial finish and including the initial residual tensor induced by the previous machining procedure. Amini et al. 3D model uses the Coulomb-Mohr's frictional model without cohesion, according to the power law:

$$\sigma = K\epsilon^n \tag{6}$$

Where σ is the stress, K is the stress for unitary strain, ϵ is the real plastic strain experienced by the material, and n is the self-hardening coefficient of the material. [37]. This model revealed the friction influence of a ball burnishing configuration on an extruded AISI 1038 steel surface [37]. In that sense, under a defined load, a low *COF* may be effective to improve roughness but not reach a compressive state. On the contrary, a high *COF* could lead to a pile-up intensification and an increase of the surface residual stress state, but degrading surface roughness. Therefore, a factual *COF* to feed the model is required [37,70]. Additionally, the quoted 3D FEM [37] also shows that the direction of the highest residual stress concentration induced under a specific tribological configuration of burnishing will depend on the ball path, independently of the initial stress state produced by milling [37]. The most significant effect of burnishing occurs in the perpendicular direction to the ball displacement, which reflects that the process can induce anisotropic properties on the AISI 1038 steel surface [70,87].

This background emphasizes the complex requirements in the burnishing process setup and highlight the importance of friction during the process in order to achieve an optimal surface integrity. Thus, particular considerations in terms of tribo-contact between the microstructure of the target surface [35,53] and its interaction with the tool [37,81,86] must be evaluated.

Accordingly, despite the numerous analytical, experimental and numerical studies dedicated to parameterizing the process, none of them proves that, even belonging to the same metal family, metals respond in a different way to the same plastic deformation mechanism as a matter of the initial surface conditions [55-57,88-90] and of the capacity of their microstructure [35,53] to interact with the tool. For instance, TRIP AISI 301 LNS steel is impacted by the process to different degrees according to the martensitic percentage. Higher martensitic contents entail lower texture generation effects and a shallow hardening effect in the subsurface [56]. Furthermore, after burnishing, textured steel surfaces (such as Ck45 steel) can adopt a defined texture orientation regardless the previous one [57]. Besides, Kuznetsov et al [55] identified the relevant influence of friction (as a function of load) on the final surface state by nanostructuring the microstructure on the subsurface of HRC55 20Cr4 steel through burnishing. Therefore, the friction enforces the intensity of the deformation-induced behavior. High friction leads to a thinner layer of plastic deformation on the surface (maximum concentration of frictional shear stress). In contrast, low friction propagates the deformation in depth. In consequence, the main external process parameters, such as load, side pass, and ball conditions [35,36,38,50,52,53,64,81] must be set according to the material of the machined component [35], considering the interactional factors, such as the friction coefficient [37,84,86] and the imparted anisotropy [37,53,57,58,70] (that decreases as the load increases [58]), in compliance with the performance of the final component.

Accordingly with all the aforementioned, the study of the burnishing performance takes a new approach: a tribological approach. It is the tribo-contact between the burnishing ball and the machined material that determines the intensity of the deformation-induced behavior at the subsurface of the material [55]. The high friction generated by an increased load leads to a stress state induced in the front protrusion similar to that induced by uniaxial compressive loading. In contrast, the rear area behind the indenter reacts as if uniaxial tension is imposed. The higher the coefficient of friction, the lower the maximum shear stress in the subsurface. Consequently, the plastic deformation is concentrated in a thinner surface layer. However, too high friction values could lead to surface deterioration (fracture, tensile residual stresses) [55]. When friction decreases, the depth of the maximum shear deformation increases (which reduces the effectiveness of cold nanostructuring) [55] and, eventually, it could promote residual stress relaxation, reducing the inhibition of crack propagation [37]. Thus, the burnishing tribo-interaction defines the geometry (by the degree of plastic deformation) and the location of the maximum residual stress (by the depth of shear stress). Consequently, ball burnishing must be

settled according to part performance, prioritizing the geometric (roughness) or metallurgic (hardness and compression stress state) characteristics [35,54,87]. Therefore, both the micro- and macro-responses to the process must be investigated through the microstructure influence on friction behavior.

2.2.2. Wire drawing process

Wire drawing is generally a cold working operation where a cable is extracted from coils to be passed through a series of draw dies (between 4 and 12) until reach the desired diameter, according with Figure 2.14.
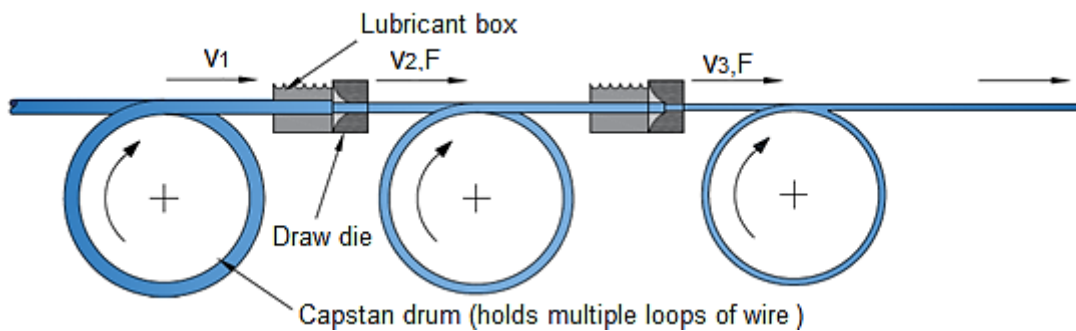
Figure 2.14. Continuous drawing of wire [2]

Prior to drawing process, the stock must be prepared. As first step, it must be annealed to increase the ductility. Then, it is necessary to clean the stock to prevent damage of the part and draw die. Chemical pickling or shot blasting are usually used to remove surface contaminants. When necessary, a pre-lubrication of the wire, in order to guarantee that the wire rod slides through the die, is applied after the cleaning step. The diameter reduction of the starting end of the stock (pointing) is performed so that it can be inserted aligned through the draw die to start the process [2]. Then, a proper lubrication is essential to minimize the friction during the drawing. The selection of the lubricant (oil or water-based lubricants) is based on its tribological attributes and its cooling power. Lubrication can be applied to the die inlet, the wire, or also to the capstan [21].

The drawing die is the most critical part of the process, because it gives the final shape of the wire. In the wire drawing process, the die angle, coefficient of friction, and area reduction have a major influence on stress inhomogeneity and the wire quality as well as die wear [28]. Regarding the tool geometry, typical draw die is shown in Figure 2.15.
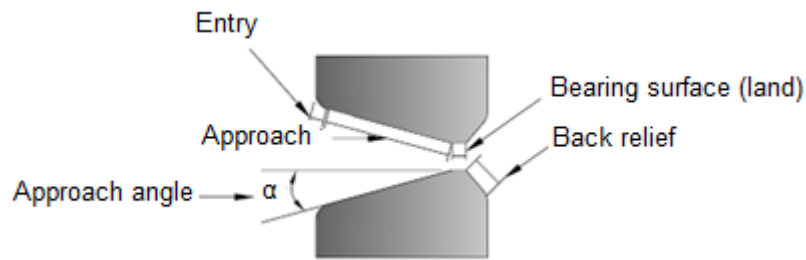
Figure 2.15. Draw die for wire drawing [2]

The entry is usually a bell-shaped mouth that does not contact the part but is necessary to funnel the lubricant into the die and prevent scoring of part and die surfaces. The approach is where the drawing process occurs with a half angle between from 6 to 20 degrees (it depends on the work material). The size of the final drawn stock is determined by the bearing surface or land. Finally, the back relief is provided with a back relief angle of about 30º [2].

Drawing dies are usually manufactured by spark erosion machining also known as (EDM). EDM is typically used when it is necessary to machining complex shapes in hard materials, making a copy of the tool in the manufactured part. The EDM process involves using thermal energy to excess material from a part, creating the required shape (see Figure 2.16).
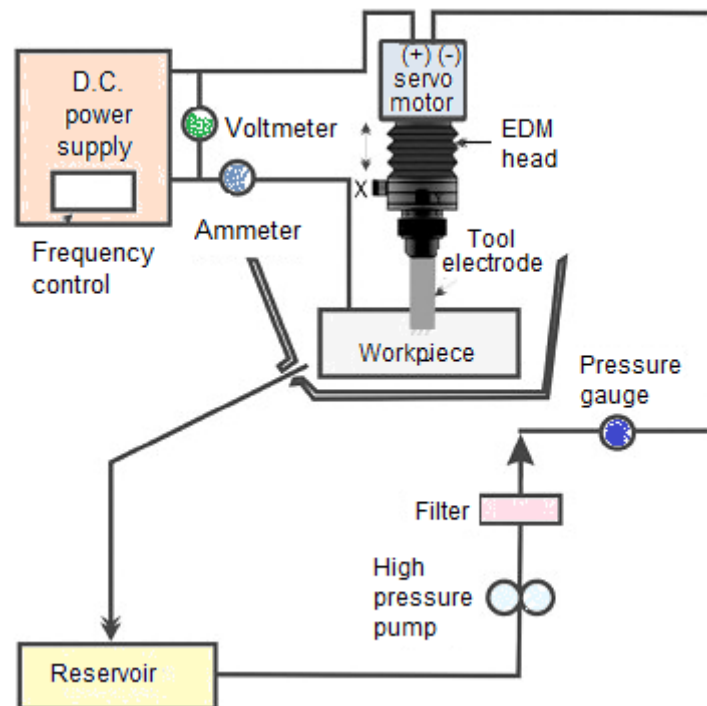
Figure 2.16. EDM cutting process in hard materials surfaces [91]

Then, EDM process interacts with the tool surface layer creating a characteristic rim zone alteration. According to the literature, in cold forming processes, the failure of the tool mostly

occurs due to the inadequate EDM process evidenced by the formation of a brittle white layer on the metal surface. Although this layer is generally reducing the mechanical endurance, the precise structure and composition of this layer is unknown. The characteristics of the white layer can affect the mechanical behavior significantly reducing die drawing life and the comprehension of its influence on the withe layer formation is crucial to guarantee a satisfactory surface integrity of the die tool [92].

During EDM manufacturing, the craters formed in the electrode are sources of defects in the part, however these defects can serve also as a refrigerant reservoir. The number of defects in the part increase with increasing pulse energy. When low energy levels (low thermal energy) are applied, the with layer surface is thinner. However, low energy machining increases the possibility of arcing due to a reduced spark gap. Then, effects such as stress concentration zones, micro-irregularities and molten material can be observed in the manufactured part. On a microscopic scale, due to the thermal energy of the process, defects induced by the EDM are similar to stress cracks. On the other hand, when the discharge energy is reduced, the average surface roughness of the tool improves but it also depends on the type of electrode used [93]. Copper electrodes are the best in terms of material removal, wear ratio but it had no significance in the surface finish improvement [93].

When high energy levels (high thermal energy) are applied, the material removal rate is also higher. this implies a surface characterized by metal inclusions, microcracks and gas trapped in the white layer . In summary, relatively satisfactory die tool surface finish results in an EDM intermediate energy level . With a controlled white layer formation, wear ratio is also improved due to the reduction or even elimination of the brittle white layer [93].

The dies made of diamond or cemented tungsten carbide are used in the manufacture of round wire. Softer cemented carbides, containing approximately 8% Cobalt (Co), may contain greater reductions without breaking, but wear out faster than lower cobalt grades [21]. The use of diamond dies is restricted by limitations in the available industrial sizes and by the cost, although the latter is a relative parameter since diamond tools can outperform cemented tungsten carbide matrices by 10 to 200 times. In that sense, a variety of polycrystalline and monocrystalline synthetic diamond matrices became available to reduce the cost [21]. For special shapes, hardened tool steel is used which is lower in cost but does not provide superior performance (greater reductions without breaking) like cemented carbide which is effectively used in any application [21]. In this regard, tool steel wire drawing dies, should have an almost maximum hardness (62 to 64 HRC) for reductions of less than about 20%. For further reductions, the hardness should be reduced (due to the possibility of die breakage) to 58 to 60

HRC, although the wear rate will increase. Wear resistance is sacrificed to minimize die breakage. Die breakage is typically due to abnormal reductions, inadequate lubrication, lack of mechanical insert support, or use of a tool material that is too hard for the process [21]. All of these with consequences in friction, wear, and wire surface integrity.

Die wear is the predominant factor affecting tool life and wire tolerances in the drawing process by thermal load and wire-die contact during the deformation process [94]. Then, as the first step to obtain an effective deformation of the wire during its passage through the die it is necessary to minimize the friction generated by the sliding contact [2,95]. Die wear can be divided into three zones, according with Figure 2.17: the first wear zone is around the first contact point between the wire and the die. The second wear zone is the working cone and the third is the bearing at the die exit [28]. Therefore, the understanding of die wear mechanisms and the factors that control the COF (explained in detail in section 2.3 of this chapter) during the drawing process are crucial to improve both wire surface quality and tool life.
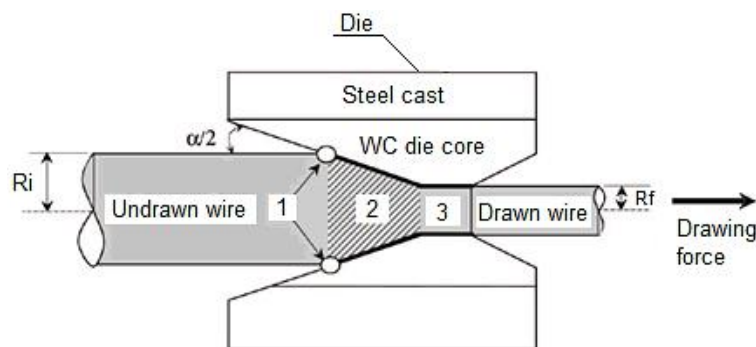
Figure 2.17. Working zones of draw die : (1) first contact point zone, (2) working cone zone and (3) bearing zone [28]

The high-pressures reached during wire drawing process entails adhesion as a main wear mechanism, resulting in a COF increase during the wire drawing process [2,21,95]. Because of the aforementioned wear mechanisms, marked scratches or striations following the sliding direction can be observed in the softer material [32], resulting in a defective and dimensionally inaccurate product [94]. In addition, when cemented carbide (hardmetal) dies are used in the drawing process, it has been reported that the size of the scratch marks observed on the tool, correspond to the size of the tungsten carbide grains of the hardmetal tool [96]. There is scarce literature in that field during drawing process, but some works have reported cavities left by the WC dislodged during machining of aluminum on the hardmetal (WC/Co) tool surface due to a preferential wear of its softer binder (Co) [96-100]. Moreover, recent advances in improvements of hardmetal tools wear during continuous sliding contact with soft materials (copper)

mentioned this phenomenon; however, its characterisation remains in the early stages of development [101]. Thus, the presence of hard tungsten carbide (WC) free particles in the die-wire contact entails a third-body wear abrasion (explained in section 2.1.3) that involves a micro-cutting effect on the surface wire of the soft materials like aluminum or cooper. At that point, micro-cutting effect is repeated several times on the emerging feedstock surface, giving rise to a different levels of ductile microfractures [95,102] known as chevron cracking (or crow's feet) [95], as Figure 2.18 exposes.
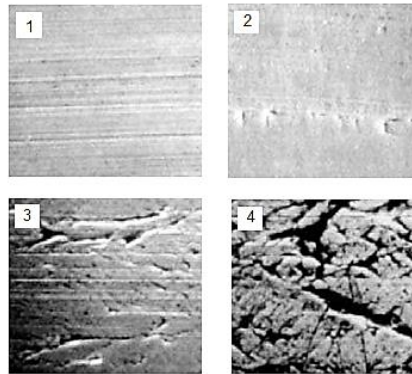
Figure 2.18. Levels of chevron cracking on wire surfaces [95]

These microfractures are caused by high local stresses concentration on the surface wire due to the micro-cutting that results in a micro-fatigue state on localized parts of the drawn wire [23]. Thus, third-body wear abrasion in hardmetal dies, constitutes a main problem in terms of wire surface quality, since it allows the propagation of fatigue failure [108] and the retention of impurities on the surface [95]. Moreover, tool service life is also affected due to continuous loss of surface material and consequent matrix weakening [95,102].

Therefore, in order to reduce these tool and wire detrimental effects, optimal lubrication and the use of coatings as a complement, are mandatory. A proper lubrication strategy reduces adhesion, power, heat, friction, and tool wear while a better surface finished wire is obtained [2,104]. In that sense, it is convenient that the lubricant adheres to the surfaces to reduce friction [2]. Thus, the roughness conditions of the surfaces in contact govern the lubrication regime by voids acting as reservoirs influencing the contact area and local stresses that lead to wear [105]. Furthermore, regarding the drawing Al alloy production, the hardness and roughness of the films must be taken into account in terms of compatibility with the lubricant [103].

According to previous studies, wear in the die tool has been considerably reduced improving the wire materials properties as well as using coatings on the tool surface [103,106,107]. For instance, the effect of reinforcement TiC nanoparticles in a wire aluminum alloy matrix, even

in dry conditions has been proved to enhance tool life reducing die wear [108]. It has been proved that coating films provides a lower COF, high thermal and mechanical fatigue and wear resistance to the metal forming tools [103,106,109]. Besides, they constitute a shield against Co wear in hardmetal tools, being that even in lubricated conditions [107], the adhesion on the tool surface and its effects persist [103]. For this purpose, the use of low friction coatings as diamond-like carbon (DLC) [106,109-113] (described in section 2.1.2.2) has been proved effective. DLC coatings constitute a technological solution to reduce the tool wear mechanisms [109], becoming industrially relevant due to their noteworthy tribological characteristics [106,109-113]. In that sense, Vidales et al. [109] have evaluated the tribological performance of a-C:H/Cr and a-C:H/CrN amorphous hydrogenated carbon coatings deposited on WC/Co balls while interacting with Al 5754 discs under lubricated conditions, in order to reduce the tool wear caused by aluminum transfer during forming process.

2.2.3. Hardmetal as tool material used for selected continuous deformation processes

Cceramic-metal composites (Cermets) are metallic matrix compounds (MMC) made of metallic matrix reinforced by a second phase that includes ceramic particles and fibers from other metals, ceramics, carbon and boron. Cermets are subdivided into oxide-based cermets and cemented carbides. Oxide-based cermets generally use Al_2O_3 as the particulate phase. A common metallic matrix is chromium. They are used, e.g., for cutting tools and mechanical seals. Cemented carbides or hardmetals (WC/Co) are formed of one or more carbide compounds (usually WC) acting as hard and wear-resistance phase, bonded in a ductile metal matrix (usually Co). They are based on tungsten carbide (WC), titanium carbide (TiC), chromium carbide (Cr_3C_2), and tantalum carbide (TaC), among others. The main metal binder for the WC is cobalt (Co), while Ni is used for TiC and Cr_3C_2. The binder constitutes only about 5% to 15%, but it significantly affects their mechanical properties [2]. Hardmetal exhibits an outstanding combination of hardness, wear resistance, strength and toughness because of their microstructure and composition. This unique combination of properties enables hardmetal to be widely used in engineering and tooling applications that require extremely demanding conditions, such as ball burnishing and wire drawing continuous deformation processes. The remarkable performance of hardmetal is given by their microstructure, that includes composition, content, size and distribution of the constituents as main microstructural

parameters. This microstructure can be tailored regarding each particular engineering application broaden their application fields and uses.

Cement carbides are produced by liquid phase sintering. In the first stage, the reduction of oxides and degasification of the binder (shrinkage) is induced [31,93]. As the temperature increases, the binder wets the WC grains and subsequently the dissolution and transport of material takes place by diffusion in the solid state, the porosity decreases, and the material dissolved in the binder begins to precipitate in the undissolved grains. The reorganization of particles and the contraction of the mixture favor densification. Once the WC/Co melting temperature has been reached (1300 ºC) the sintering phase begins, the small WC grains dissolve until saturation while the larger ones thicken and densify completely. With subsequent cooling, solidification of the material is obtained [31,113-115].

About the factors that influence the properties of WC/Co, that are the grain size and cobalt content [65]. Figure 2.19 shows the effect of cobalt content on hardness and transverse rupture strength (TRS) [2].
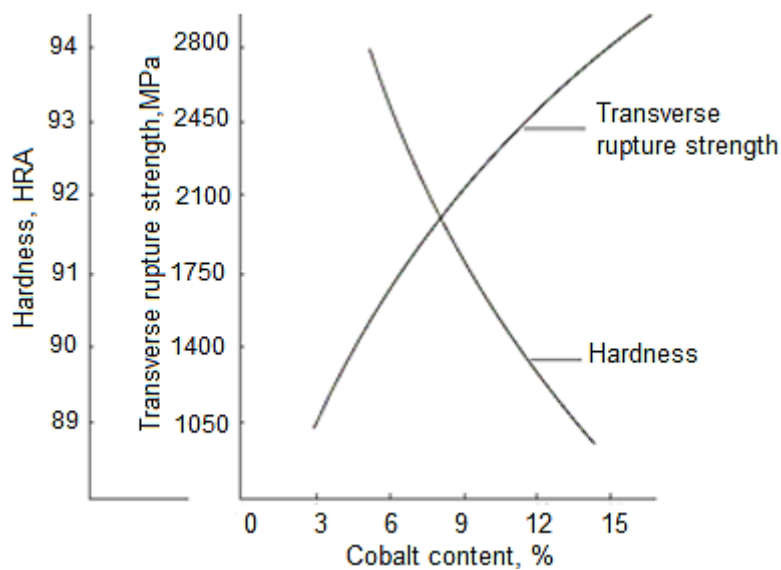
Figure 2.19. Typical plot of hardness and transverse rupture strength as a function of cobalt content [2]

On the other hand, Figure 2.20 shows the specific properties confer by different combinations in the microstructure [66].
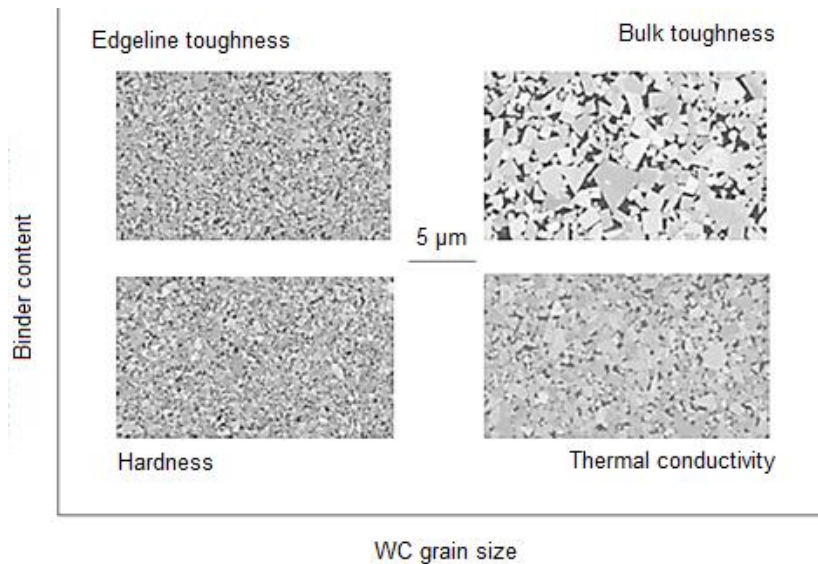
Figure 2.20. Correlation between binder content and WC grain size with main properties of cemented carbides [66]

Figure 2.21 shows the classification according to the Fachverband Pulvermetallurgie of WC/Co microstructures for different WC grain sizes.

| Ultrafine | Submicron | Fine | Medium | Coarse | Extra coarse |
| (0.2-0.5) µm | (0.5-0.9) µm | (0.1-1.3) µm | (1.4-3.4) µm | (2.5-5.0) µm | >5.0 µm |
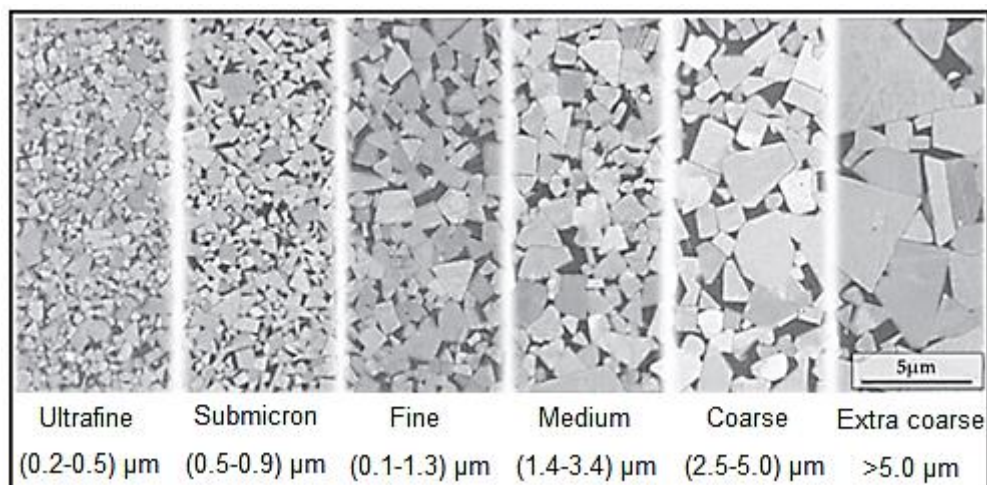
Figure 2.21. WC/Co microstructures for different WC grain sizes [65]

Due to its wide variety, several international classification systems have been created, including ISO-committee TC, the US-Industrial code and DIN 4990 [66]. García et. al. [66] classifies cement carbides and cermets based on the microstructure in four groups with five sub-categories, as seen in Figure 2.22.

Figure 2.22. Categorization of cemented carbide microstructures selected [65]

The WC phase- hexagonal close-packed (hcp) possesses a narrow range of homogeneity, high hardness and a significant ability for plastic deformation. Fine and nano-grained WC are generally used for cutting tool inserts [67]. A grain size of less than 0.2 µm is considered nanometric [68]. Bi-modal WC grain size distribution involves the interaction of two WC raw materials of different sizes but with uniform characteristics, which provides greater strength to toughness ratio (generated in the optimized path of the metal binder) and greater resistance to plastic deformation (due to the dense packing of WC grains). Hexagonal doped –WC consists of doping the WC of hcp structure to alter the properties of the final product. Thus, Weidow et al. doped WC with Tantalum (Ta), increasing the ductility and toughness of the piece but sacrificing hardness [69,72]. During the sintering process, the carbide crystals develop a truncated trigonal prism shape, however, by doping the WC with another component and due to the increase in anisotropy and small platelets can be generated during precipitation, this type of cement carbide is known as Platelet WC [116]. The plate-like grains form a barrier in the propagation of cracks. Cubic carbides and additional carbides such as WC-Co-γ-phase, cermets, WC-CO-η- phase, particle reinforced cement carbides and NbC-based cermets, are mainly used for cutting tools. They are produced by substitution (cermets) and / or addition of Ti, Ta, Nb, V, Zr or Hf carbides to WC/Co and by adding hard phases of oxides, silicides or borides that are not part of the carbide skeleton but that increase its resistance. Regarding gradients, cement carbides with different regions or gradients can be produced in such a way the gradient presents greater toughness in its surface layer due to higher content of Co, on the contrary, the gradient presents greater hardness in the external layer due to a greater concentration of carbides. These

gradients allow the surface layer to be preloaded to avoid cracking and propagation of cracks [117].

The most common binder hardmetal is the Co. It has been attempted to replace with Ni but its work hardening is moderate and it has less capacity to dissipate energy during the crack propagation [118]. On the other hand, iron binder tends to form martensite during cooling, which represents a disadvantage due to its hardness and brittleness. However, combination of these three elements can be advantageous in certain applications [119]. The use of multilayers of Al_2O_3, Ti (C,N), Zr (C,N) and (Ti,Al) N provide great advantages in applications where high resistance to corrosion and wear is required as well as a coefficient of low friction [2]. Coated carbides have one or more layers of titanium carbide, titanium nitride and/or aluminum oxide applied superficially by CVD or PVD to increase the wear resistance. The coating thickness is between 2.5 to 13 µm. Higher thicknesses can generate brittleness and subsequent separation of the substrate. Multilayer approaches are being applied and are used as TiN or TiCN base due to their good adhesion and similar coefficient of thermal expansion. Layers of TiN, TiCN, Al_2O_3 and TiAlN are subsequently applied [2]. Therefore, selection of WC grain size, % Co, and alloying materials must be carried out depending on the service to guarantee the processes [2].

2.3. Main conclusions of the state of the art

Through the state of the art, the fundamentals for the development of this work and its satisfactory completion by optimization of two relevant industrial continuous deformation processes: ball burnishing and wire drawing, have been outlined. So, the processes conceptualization from the operational and geometrical parameters have been established. However, it has been evident that the tribo-interaction inside the selected processes is not prioritized as a fundamental variable, despite the available knowledge on the topic. This dissertation combines the current process configuration with the essence of the interactions that follow them. In this manner, the main conclusions resulting of this background are for each studied process:

2.3.1. Ball burnishing – main conclusions

1. A specific methodology for the tribological characterization of the burnishing process is not available. Their configuration is limited to the operational parameters, then, their improvements must be achieved by a proper tribo-interaction.

2. There is not a suitable tribotest configuration for the process. There is the need to design it, in order to feed integral numerical models and to achieve reliable experimental approaches that constitute a sustainable solution for the industry.

3. The numerical models of ball burnishing do not contemplate a factual value of COF, only approximate values where considered. Those conceptual values do not contemplate the differentiation of the processes and materials, which leads to a false estimate of both, the tool conditions and the surface finish of the treated parts.

4. Despite the availability of surface characterization techniques and resources for tribological improvements within the studied process, there is no established procedure that makes use of them in order to obtain the optimal COF that allows to improve the tool and part surface integrity.

5. Techniques and procedures have been established to improve surface conditions for ball burnishing processes, but none of them regards the friction control on their resulting surfaces.

2.3.2. Wire drawing – main conclusions

1. Despite the different available configurations of tribotest, each case needs to be settled according to the specific interacting materials. Then, with the development of new materials, new methodology for the tribological characterization must be established.

2. The process has characterized since an operational view, where friction consequences are only quoted but not established from the beginning of the materials interaction. Then, its optimization must begin from the prior tribo-contact approximation.

3. Although there are several techniques of surface characterization, scare of them related wear with friction values for the wire drawing process. Then, it is important to define a methodology that relate wear and friction, in order to improve the tool and part surface integrity.

4. Techniques and procedures have been established to improve wear conditions for wire drawing processes. Nevertheless, these improvements must be settled according to the explicit materials and its interaction capability with the material tool, coatings and lubricants.

Chapter 3

Materials and methods

The purpose of this chapter is to define the materials, including lubricant and coatings, as well as the experimental and numerical path to assess and characterize the tool-part tribological interaction for both continuous deformation processes: ball burnishing and wire drawing. Since both processes occur under sliding contact conditions, the determination of the COF is computed under the same tribological test conceptualization. Then, two different tribological approaches haven established to evaluate the efficiency of these processes in terms of the final surface integrity analysis of each processed part. In the ball burnishing process, surface integrity is defined according to the surface roughness and residual stresses state on the treated piece. In the wire drawing processes, surface integrity is defined considering the wear mechanisms that influence the tool that have a direct influence in the wire final macro-conditions.

The presented methodology gives solution to the previous questions set out in section 1 (1.2.1). Thus, processes optimization and improvement in surface integrity of the parts can be achieved thorough the tribological approach presented in this thesis combined with the use of numerical tools as well as applying coating and lubrication strategies referred in the previous chapter.

3.1. Materials

In this thesis different materials have been considered depending on the particular study case. On one hand, the ball burnishing study case is carried out in stainless-steels, including, austenitic and martensitic microstructures. On the other hand, the wire drawing study case is accomplished in aluminum and aluminum with reinforcing TiC particles wires. However, in both cases the same hardmetal balls have been used as a counterpart in the tribological laboratory tests. In this section, the used lubricants and coatings in wire drawing case study are also described.

3.1.1. Hardmetal

Tribological laboratory tests were carried out using a WC/Co ball as a counterpart to compute COF values. The characteristics of the WC/Co ball employed in this experimental assessment are summarized in Table 3.1:

Table 3.1. WC/Co ball characteristics

Diameter [mm]	%Wt. Co	Grain size [2,69]	Ra [µm]	H [GPa]
10	5%	Submicron	0.023 ± 0.003	20.3 ± 0.6

3.1.1.1. WC/Co ball coatings

The use of coated tools is a common industrial strategy to reduce or even eliminate wear. In that sense, this work takes into account the effectiveness of a low friction coating in reducing the wear mechanisms observed when an uncoated WC/Co ball is used. Two different DLC coatings with a bi-layer architecture, have been deposited on WC/Co balls (Figure 3.1): DLC hydrogenated amorphous carbon coating (a-C:H) with a Cr interlayer, Figure 3.1 (a), and DLC hydrogenated amorphous carbon coating (a-C:H) with a CrN interlayer, Figure 3.1 (b). In both cases, the thickness of the top layer was around 1µm, while Cr and CrN interlayers shown a thickness around 1µm and 3µm, respectively.
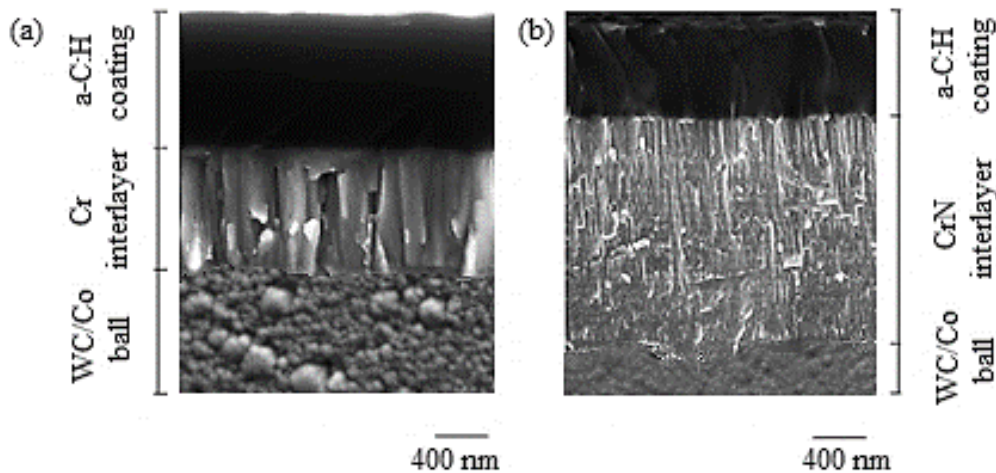
Figure 3.1. Coatings deposited on WC/Co balls for scratch tests:
a) a-C:H/Cr and b) a-C:H/CrN

Conventionally, a selection criterion between the DLC coatings shown in Figure 3.1 is the loading support given by a CrN interlayer. [109] shown a gradient hardness profile in depth which tend to improve the adhesion between substrate and coating. The a-C:H/CrN coating is designed for applications with high stress concentration and high abrasion wear or micro-impacts, such as forming tools [109]. However, the top layer is the same in both cases (a-C:H),

thus is expected to have similar hardness values at the surface layer. On the other hand, the Ra is highly influenced by the coating growing of the interlayers Cr and CrN. In this case Cr adhesion layer presented a densified columnar structure, while the CrN presented a coarse cauliflower columnar structure which was replicated by the a-C:H top layer. Thus, surface quality of a-C:H/CrN presented disrupts and some isolated droplets on surface, as shown in Figure 3.1.

3.1.2. Stainless-steels

Austenitic AISI 316 stainless-steel (processed according to EN 10028-7-2016) and martensitic precipitation-hardened UNS S46500 stainless-steel (aged according to ASTM A564/A564M) were selected for the present assessment.

3.1.2.1.   Chemical Composition and Material Processing

Table 3.2 shows the chemical composition of the analyzed materials obtained by spark emission spectrometry (SPECTROMAXx LMF08, SPECTRO, Kleve, Germany).

Table 3.2. Chemical composition of analyzed steels (in wt.%)

Material	Fe	C	Mn	Ti	Cr	Ni	Mo
AISI 316	68.50 ± 0.03	$0.02 \pm 2\times10^{-4}$	$1.25 \pm 4\times10^{-3}$	$0.01 \pm 1\times10^{-4}$	16.69 ± 0.01	9.92 ± 0.02	2.21 ± 0.005
UNS S46500	74.40 ± 0.02	$0.01 \pm 6\times10^{-4}$	$0.03 \pm 3\times10^{-4}$	1.70 ± 0.02	11.69 ± 0.03	10.89 ± 0.01	$1.01 \pm 6\times10^{-3}$

3.1.2.2.   Microstructural Characterization

After mechanical polishing to a mirror-surface finish (0.03 µm colloidal silica suspension), the AISI 316 and UNS S46500 samples were etched with aqua regia solution and Kalling I reagent, respectively. Microstructural characterization was performed using optical microscopy (Epiphot 200, Nikon, Tokyo, Japan) (Figure 3.3). The AISI 316 microstructure consisted of austenitic grains, some of which exhibited twinning, whereas the UNS S46500 stainless-steel showed mainly a martensitic matrix.

<div align="center">
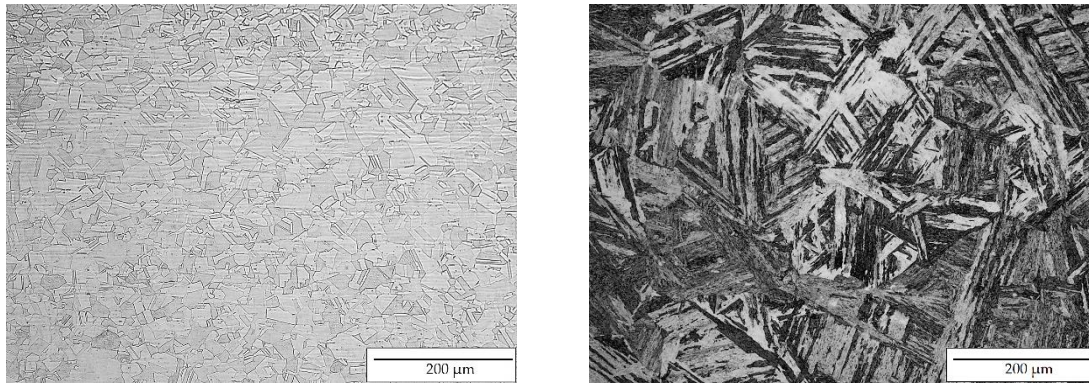
(**a**) AISI 316 Microstructure   (**b**) UNS S46500 Microstructure

Figure 3.2. Stainless-steel microstructural characterization

</div>

3.1.3. Aluminum

Two different wire materials have been assessed in this thesis, Al 1370 and Al-2%TiC wires, to determine the TiC particles effect during the interaction with WC/Co. The aluminum feedstock consisted of Al 1370 pellets with a purity of 99+% (Hydro Karmøy industry). In Al-2%TiC wire, TiC ceramic nanopowder of size between 40 nm to 60 nm (US Research Nanomaterials, Houston, TX, USA) has been introduced in Al 1370 wire by means of a prototype screw extruder machine (patent number EP2086697B1 WO2008 06307) [126] located at the Department of Materials Science and Engineering of the Norwegian University of Science and Technology (NTNU).

3.1.4. Lubricant

For the wire drawing study case the influence of lubricants during the sliding contact between hardmetal and aluminum has been considered. A commercial mineral oil base enhanced with additives, described according to Table 3.3, was applied over each of the studied wire materials.

<div align="center">

Table 3.3. Lubricant characteristics

Lubricant	Formulation	Viscosity (ISO 40ºC)	Flash/pour point
LUB 1	Mineral Oil+Ester additives	170 mm² /sec	215/-3 ºC

</div>

3.2. Experimental Methods

3.2.1. Mechanical characterization

Mechanical characterization of the samples was carried out with uniaxial tensile test, conventional Vickers hardness and with nanoindentation for hardmetal balls and coatings.

3.2.1.1. Uniaxial Tensile Properties

Tensile testing is a fundamental test to obtain the mechanical properties of isotropic materials. In a tensile test, a sample is subjected to a controlled tension until failure. Properties that are directly measured via tensile test are ultimate tensile strength, fracture strength, maximum elongation and reduction in area. From these measurements the following properties can also be determined: Young's modulus (E), Poisson's ratio (ν), yield strength ($\sigma_{ys)}$ and strain-hardening (n) properties.

Ball burnishing case study

The elastic properties of austenitic and martensitic stainless-steels were established using an ultrasonic method (Panametrics 5900 PR pulser, Olympus, Tokyo, Japan) and an oscilloscope (Hameg HM1508, RS, Corby, UK). The longitudinal plastic tensile properties were acquired using the conventional tensile test configuration (ISO 6892-1 standard). Three AISI 316 and five UNS S46500 tensile specimens fitted to the standard requirements (width=6 mm and Lc=34 mm) [120] were tested. The strain measurements (0.0067 s-1 until the failure) were obtained by a video-extensometer device. Table 3.4 shows the measured mechanical properties for both materials.

Table 3. 4. Mechanical properties of the AISI 316 and UNS S46500 stainless-steels

Material	E [GPa]	ν	σ_{ys} [MPa]	UTS [MPa]	n
AISI 316	203.6 ± 0.4	$0.287 \pm 6\mathrm{x}10^{-4}$	327 ± 2	588 ± 1	$0.307 \pm 8\mathrm{x}10^{-4}$
UNS S46500	198.8 ± 0.4	$0.294 \pm 2\mathrm{x}10^{-4}$	1571 ± 8	1656 ± 5	$0.29 \pm 2\mathrm{x}10^{-3}$

Wire drawing case study

Conventional tensile tests according to ISO 6892-1 standard were performed to obtain the tensile properties of the two investigated wires for the longitudinal orientation. Tensile specimens with a width of 1.8 mm and a parallel length (Lc) of 90 mm were used (specimen described in Annex C of ISO 6892-1). The head displacement was directly used to obtain the strain measurements. The strain rate during the test was 2.5 mm/min until the end of the elastic

deformation. Three specimens per material were tested. The mechanical properties obtained are summarized in Table 3.5, each value represents the mean of the three measures and their standard deviation.

Table 3.5. Al 1370 and Al-2%TiC wires mechanical properties

Specimen Ø 1.8 mm	σ_{ys} [MPa]	UTS [MPa]	n
Al 1370	34 ± 12	102 ± 0	0.32 ± 0.13
Al-2%TiC	97 ± 16	129 ± 2	0.05 ± 0.01

3.2.1.2. Micro-hardness

A particular meaningful quantity in indentation hardness is the mean contact pressure of the contact and is found by dividing the indenter load by the projected area of the contact. The mean contact pressure, when determined under conditions of a fully developed plastic zone, is taken to be the indentation hardness, H, of the specimen material. Conventional hardness test is generally made with either spherical (Brinell test) or pyramidal (Vickers test) indenters. For a Vickers diamond indenter (a square pyramid with opposite faces at an angle of 136° and edges at 148°, the Vickers hardness (HV) is found from:

$$HV = \frac{2P}{d^2} sin \frac{136°}{2} = 1.86 \frac{P}{d^2} \tag{6}$$

With *d* equal to the length of the diagonal measured from corner to corner on the residual impression in the specimen surface.

Ball burnishing case study

Hardness values of the austenitic AISI 316 and martensitic UNS S46500 stainless-steels were computed from the mean of 10 measurements acquired using the Vickers microindentation test at a load of 1000 g (Micrometer HV1, Future Tech, FM-700, Tokyo, Japan). The hardness values were 168 ± 6 HV and 521 ± 10 HV, respectively. the. Ferritic AISI 1038 steel, used as a reference in this study, has a hardness value of 175 HV $\pm$ 10 [37].

Wire drawing case study

Hardness values Al 1370 and Al-2%TiC alloys were acquired by Vickers microindentation test at 500-g load (Micrometer HV1, Future Tech, FM-700, Japan), three indentations per material were performed. The hardness values were 31 ± 2 HV and 44 ± 2 HV, respectively.

3.2.1.3.   Nano-hardness

In addition to conventional micro hardness testing, nanoindentation experiments were performed to obtain in situ recording of applied load (P) - penetration depth (h) curves. Nanoindentation technique captures the progress with time of the evolution of the contact response of the specimen. In that sense, nanoindentation is the most suitable technique to compute coatings hardness. In this thesis, a Nanoindenter XP (MTS) equipped with a Berkovich tip (a diamond three-sided pyramid) was used to compute the hardness of the coatings described in section 3.1.1. The indentations were performed at a maximum applied load of 10 N on WC/Co balls (as a reference) and on coatings previously deposited on WC/Co flat surfaces. Hardness values were computed using the Oliver and Pharr methodology [121]combined with the 10% rule for indentation depth on coatings. The 10% rule refers maximum penetration depth to which an indentation test can produce substrate independent hardness measurements. Thus, coating hardness values were computed at a penetration of the 10% of their thickness.

3.2.2.   Ball Burnishing Process

Ball burnishing process on the surface was performed by means of a CNC router milling machine. The burnishing tool protected by Spanish patent number 201730385 commercially known as Acoustomill [78] was used by adapting a 10 mm diameter hardmetal ball in the force transmission unit. The initial burnishing load and the number of passes were selected according to the referential conditions used in the preceding study settled by Amini et al. on ferritic milled surfaces [37]. Nevertheless, due to the low hardening coefficient and high hardness conferred by the martensitic matrix, UNS S46500 required a load increase in contrast to AISI 316. This load increase allows evaluating the capability of the model to predict the tribological material answer, as well. The process setup and its descriptive scheme are shown in Figure 3.3.
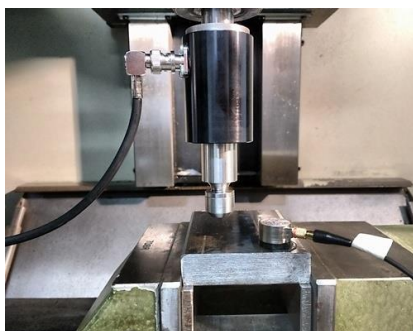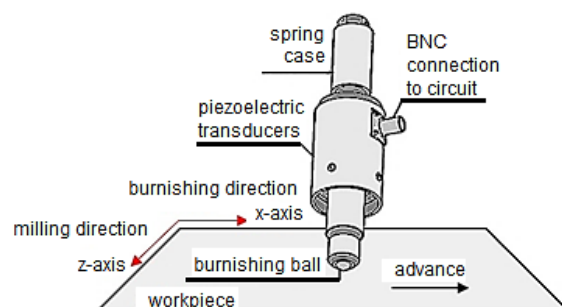
(**a**) Ball-burnishing setup   (**b**) Ball-burnishing descriptive scheme

Figure 3.3. Ball-burnishing configuration

The set assembled in the CNC router milling machine was displaced once in the perpendicular direction (x-axis) to the milling finish (z-axis) on a 10 mm × 10 mm patch for each material. The ball-burnishing operational parameters are summarized in Table 3.6.

Table 3.6. Operational parameters of ball burnishing

Applied load	270 [N], 470 [N]
Lateral pass width	0.30 [mm]
Feed rate	600 [mm/min]
Vibration	No

3.2.3. Wire Drawing Process

To obtain the wire diameter required by WAAM technology (1.2 mm - 1.6 mm), extruded wires (Al and Al-2%TiC) were drawn at room temperature and lubricated conditions on a wire drawing machine (DWU-2/S, Friedr. Krollmann, Germany) through a seven hardmetal dies sequence. The present study considers the wire section diameter of 1.8 mm, corresponding to the penultimate drawing step, from which the final pass conditions are defined.

3.2.4. Tribological test design

Tribological test were design to quantify friction during the sliding of a rigid sphere over a surface material considered an elastic half-space. In that sense, a valid approximation of continuous deformation processes (ball burnishing and wire drawing) is the use of classical theory of Hertz for non-adhesive contact [32] as a first step to qualify the mean contact pressures existing during the sliding of the industrial process. This analytical model has demonstrated significant adjustments depending on the process configuration and the material to be deformed [40,122,123]. Based on this theory, through equations (4) and (5), the pressure in the center of the contact region (p_0) were computed as a function of the normal force (F) and the indenter radius (R).Then, friction tests were performed conforming to the sequence for designing of laboratory friction and wear proposed by the ASM [11]. A Micro-indentation–Scratch Tester MHT (CSM Instruments, Germany) was used to investigate the COF during the sliding contact performance.

Ball burnishing case study

For the ball burnishing approximation, linear scratch was performed according to the experimental parameters described in Table 3.7, at room temperature in dry conditions with a tungsten carbide ball indenter. Three tests per surface were performed.

Table 3.7. Experimental parameters of scratch test to assess the ball – stainless-steel textured surface interaction

Ball Ø	2.5 [mm]
Contact pressure	2700 / 3100 [MPa]
Sliding distance	20 [mm]
Feed rate	600 [mm/min]

Figure 3.4 shows the micro-indentation scratch tester (MHT) and a descriptive scheme of scratch test employed for this assessment.
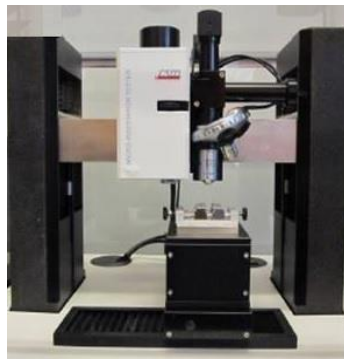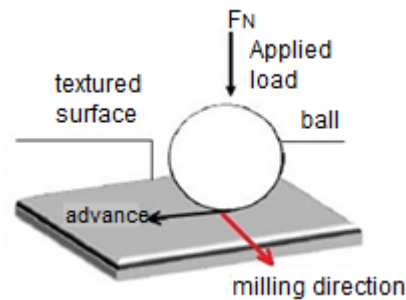
(**a**) Micro-indentation scratch tester (MHT)   (**b**) Scratch test setup

Figure 3.4. Scratch test configuration for ball burnishing study case

Wire drawing case study

On the other hand, a modified scratch test, settled in agreement with Peter et at. [130] was designed to reproduce the first stage of wear damage in a WC/Co ball surface when it is drawn over aluminum wires. It is expected that WC/Co wear damage have an influence in both COF and wire surface integrity. A scheme of the scratch test is depicted in Figure 3.5, which consists of a WC/Co ball characterized according to Table 3.1, drawn over an Al 1370 wire or over a reinforced Al 1370 with 2%TiC wire.
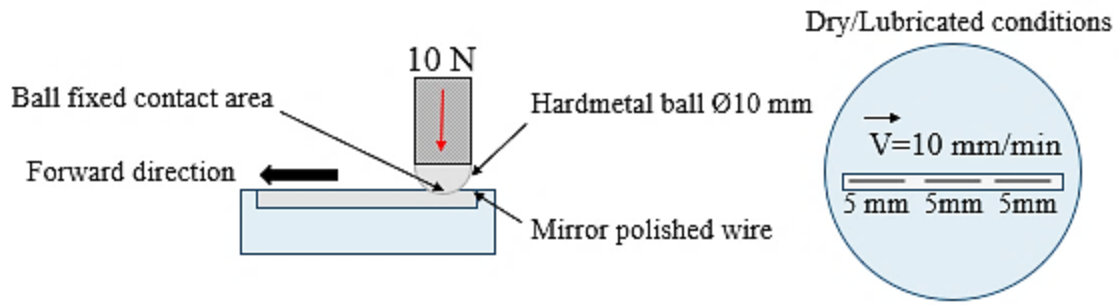
Figure 3.5. Scratch test configuration

Three scratches were performed under uncoated and coated ball conditions, as well as in dry and lubricated conditions according to the experimental parameters described in Table 3.8.

Table 3.8. Experimental parameters of modified scratch test to assess the hardmetal - aluminum sliding contact

Ball Ø	10 [mm]
Load	10 [N]
Sliding distance	5 [mm]
Feed	10 [mm/min]

Each wire sample was polished to mirror surface finish (0.03 µm colloidal silica suspension), keeping the same ball contact area on each pass. After the first scratch, the ball was removed and analyzed by means of SEM in order to determine the wear mechanisms, and by means of CSOM to compute the volume of Al adhered on the ball surface. In the same way, the scratch track was analyzed also by means of CSOM and SEM. After the analysis, the WC/Co ball was fixed again into the holder, exactly in the same position as at the beginning of the test. Then, a second scratch was performed in a new wire surface. The CSOM and SEM analysis were repeated after the second scratch. Finally, a third scratch was performed in the same way as described before. Test were designed in that way in order to reproduce the same wear mechanisms as in the drawing process of WAAM wires feedstock, in where the die is not replaced but the surface wire is always new.

3.2.5. Numerical model

By adapting the Amini et al. [37] 3D ball burnishing numerical model on a pre-textured AISI 1038 steel surface (experimentally settled in previous works [54,81]) to an UNS S46500 martensitic precipitation hardening stainless-steel used in the aerospace industry, the quoted model was validated and established as a versatile numerical tool process parameterization.

This model was settled according to the Power-law model as plastic behavior [74]. Since the inertia effects during the process are negligible [37] and the constant feed rate did not elucidate significant influence on the final steel surfaces [35,38,53], it was configured based on the implicit static analysis in ANSYS software. ANSYS analysis has exploited the augmented Lagrangian method as contact algorithm [125] and the Coulomb-Mohr's frictional model without cohesion [126] to detect contact areas between the ball and the surface. WC-Co ball was approximated as a non-deformed solid rigid due to its small deformation compared to that of part.

Under these considerations, the numerical ball burnishing was performed in x-axis direction, while the pattern of roughness was extruded along the z-axis, according to Figure 3.3 (b). The burnished zone corresponds to an area of 0.9 mm x 1.2 mm. Initial residual stress tensor induced by milling process was embedded at the depth of 4 µm as an initial input. Finally, experimental COFs were introduced as an input in order to approximate the model with the factual tribological interaction. Figure 3.6 shows the model configuration.
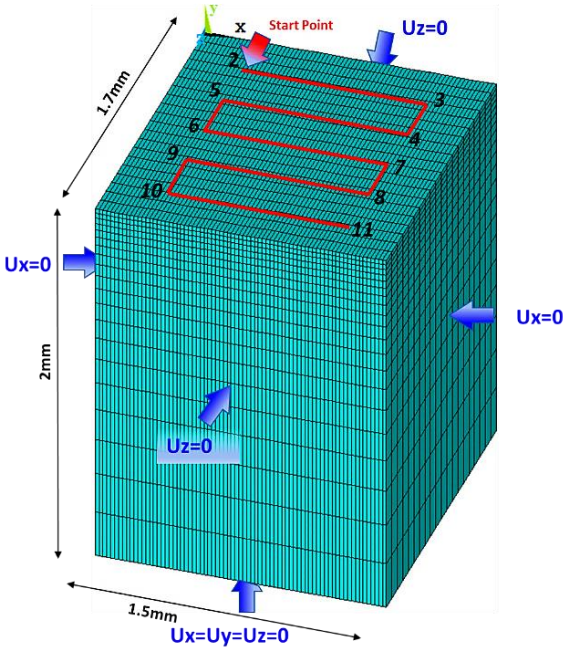
Figure 3.6. Scheme of modeled surface, boundary conditions and the path traveled during ball-burnishing [37]

3.2.6. Surface integrity characterization

Surface integrity characterization of the samples includes surface roughness, residual stresses, and ball and wire wear mechanisms identification and quantification.

3.2.6.1. Surface roughness

Surface roughness were performed with an optical profilometry microscope Alicona (InfiniteFocusSL, Bruker, Karlsruhe, Germany). In this thesis the following roughness and texture parameters were determined with image analysis software (Mountains 5.1.1.5944, Digital Surf, Besançon, France) according to the ISO 4287:1999 standard and ISO 25178-2:2016 standard:

- Ra – Arithmetical mean Roughness: It is the arithmetic average of the roughness profile deviations from the centerline along the evaluation length lm.

- Sa – arithmetical mean height: It expresses the absolute difference in height of each point compared to the arithmetical mean of the surface. This parameter is used generally to evaluate surface roughness.

- Sq – root mean square height: It represents the root mean square value of ordinate values within the definition area. It corresponds to the standard deviation of heights.

- Ssk – Skewness: It represents the bias degree of the roughness shape (asperity). If the Ssk<0, height distribution is biased over the mean plane; if Ssk=0, height distribution (peaks and bottoms) is symmetrical against the mean plane; if Ssk>0, height distribution is biased under the mean plane.

- Sku – kurtosis: It is a measure of the roughness profile sharpness. if Sku<3, height distribution is biased above the mean plane; if Sku=3 there is a normal height distribution. That means that sharp portions and indented portions co-exist; if Sku>3, height distribution is spiked.

- S10z – Ten-point height: It is the mean height over the mean surface mean for the five highest local maximums plus the mean depth under the mean surface for the five lowest local minimums.

- Str – Texture aspect ratio: It is a numerical representation of the orientation strength. If Str<0.3 there is a(directional) anisotropic surface, while Str>0.5 means an isotropic surface.

- Sdr – Developed Interfacial Area Ratio: This parameter expresses the percentage of the additional surface area of the definition area provided by the texture compared to the flat definition area.

These parameters are defined by the expressions quoted in Table 3.9.

Table 3.9. Roughness and texture surface parameters

Amplitude parameters

$$R_a = \frac{1}{lm} \int_0^{lm} y \,. dx = \frac{1}{lm} \left(\sum Ai^+ + \sum Ai^- \right)$$
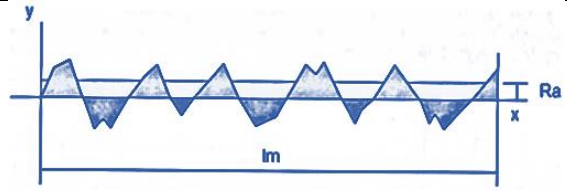
$$Sa = \frac{1}{A} \iint_{A0}^{Af} |Z(x,y)| dxdy$$
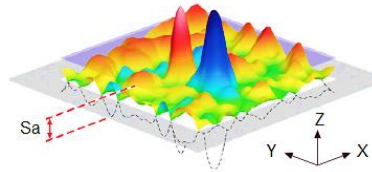
$$Sq = \sqrt{\frac{1}{A} \iint_{A0}^{Af} Z^2 (x,y) dxdy}$$
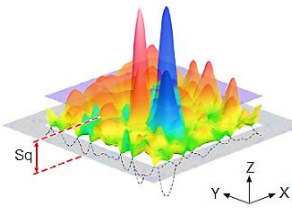
$$Ssk = \frac{1}{Sq^3} \left(\frac{1}{A} \iint_{A0}^{Af} Z^3 dxdy \right)$$

$$Sku = \frac{1}{Sq^4} \left(\frac{1}{A} \iint_{A0}^{Af} Z^4 dxdy \right)$$
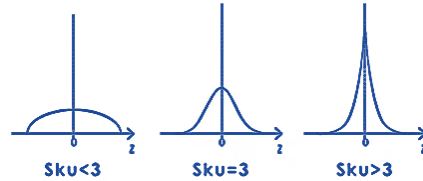
$$S_{10z} = S5p + S5v$$
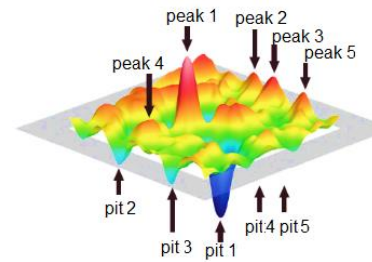
Spatial parameters

$$Str = \frac{min\left\{ \sqrt{t_x^2 + t_y^2} \right\}}{max \left\{ \sqrt{t_x^2 + t_y^2} \right\}}$$
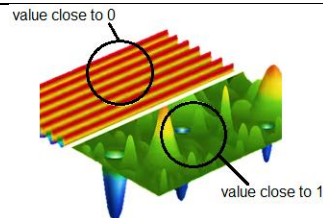
Hibrid parameters

$$S_{dr} = \frac{1}{A} \left[\iint_A \left(\sqrt{\left[1 + \left(\frac{\partial z(x,y)}{\partial x} \right)^2 + \left(\frac{\partial z(x,y)}{\partial y} \right)^2 \right]} - 1 \right) dxdy \right]$$
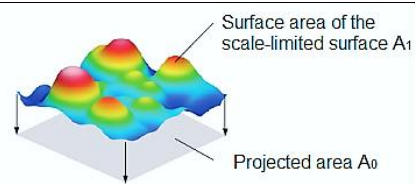
Ball burnishing study case

Before testing, the specimens were subjected to the milling conditions indicated in Table 3.10 using a CNC milling machine (LAGUN 600, MAHER HOLDING, Legutiano, Spain). The macro-texture surface parameters after the milling and burnishing processes were acquired using and further processed.

Table 3.10. Initial Milling Conditions

Tool	Ball Mill coating ø 10 [mm]– Two Teeth
Lateral pass width	0.30 [mm]
Depth of cut	0.20 [mm]
Feed rate	600 [mm/min]
Cutting speed	2000 [rpm]

Four milled samples were measured to obtain the 2D roughness profiles (Fig. 3.7), since the subsequent model configuration needs a two-dimensional signal for its initial development.
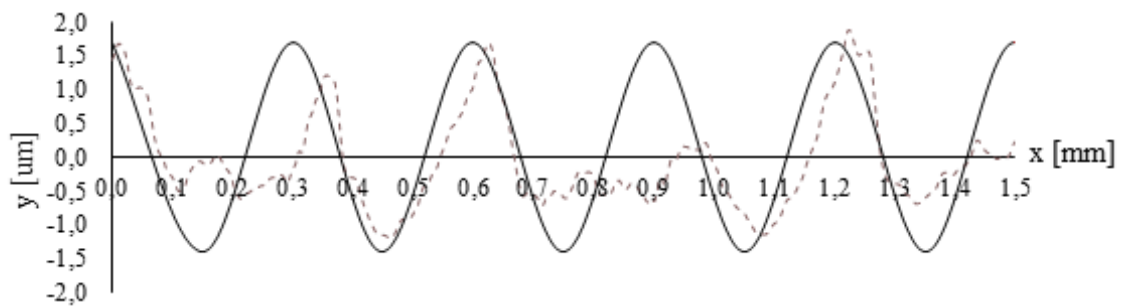
Figure 3.7. Measured roughness profile obtained through ball end milling (discontinuous line) and extruded surface profile (continuous line) applied as an input in the simulation of burnishing process

Additionally, in order to assess the surface changes due to the burnishing process, the 3D texture parameters were computed for each of the studied materials. Accordingly, the arithmetical mean height (Sa), root mean square height (Sq), skewness (Ssk), kurtosis (Sku), texture aspect ratio (Str), and ten-point height (S_{10z}) were processed.

3.2.6.2. Residual stresses

Residual stresses were only measured in burnished samples as surface integrity parameter. Residual stress components (σ_x, σ_z) up to a 4 μm depth on the ball burnished surfaces were obtained using X-ray diffraction equipment (PANalytical—model X'Pert-PRO-MRD, UCDavis, Davis, USA) according to the $\sin^2\Psi$ mode Ω-tilt method. The point detector (pixel size of 255 μm × 255 μm) was assembled on a parallel plate collimator with a 0.27° angular

opening and a planar graphite secondary monochromator. It is well known that machining and finishing operations can induce a phase transformation in austenitic steels. Then, the X-characterization of the milled and burnished austenitic and martensitic surfaces was performed in the reflection (211) of the body-centered cubic (bcc) phase (martensite). The face centered cubic (fcc) phase corresponding to austenitic steels was not found up to a 4 μm depth. This indicates that martensitic transformation occurs during the milling process. Therefore, the final conditions on the austenitic surface are not influenced by a phase change.

Wire drawing case study

3.2.6.3. Identification and quantification of wear mechanisms by advanced microscopy techniques: SEM, EDX, EBSD

In wire drawing case study wear mechanisms were thoroughly investigated as a main parameter of surface integrity that affects both tool service life and wire surface quality surface. In this work, the identification and quantification of the wear mechanism were carried out with advanced microscopy techniques and confocal scanning optical microscopy, respectively.

Advanced microscopy techniques provide information on surface topography, crystalline structure, and chemical composition of the surface of a specimen. All these techniques are based on scanning electron microscopy (SEM). In SEM, the electron beam interacts with the surface material, causing a variety of signals: secondary electrons, backscattered electron. X-Ray, Auger electrons, cathodoluminescence. In this work secondary electrons were used in order to inspect the surface topography of the samples. Also X-Ray photons were used in order to chemically characterize the adhered material in WC/Co balls. Finally, using and EBSD (electron backscattered diffraction) coupled to the SEM, crystal orientation and grain size of the hardmetal dies inspected in wire drawing processes were determined.

Wear mechanisms as well as damage were identified by means of Field Emission Scanning Electron Microscopy (FE-SEM) (Ultra Zeiss, ZEISS, USA) equipped with an X-ray spectrometry (EDX) OXFORD 5 detector. These studies were performed on industrial hardmetal dies and on the materials used at laboratory test (WC/Co balls and aluminum wires). Regarding tribological laboratory test, after each scratch test both, WC/Co ball and aluminum wire track, were inspected to correlate the effect of wear mechanisms on the wire surface integrity. WC/Co ball surface in dry conditions were analyzed after each pass. In lubricated conditions, WC/Co ball contact surface was analyzed only at the end of the last scratch, in order

to preserve the lubricant layer integrity. However, wear tracks have been inspected after each pass.

3.2.6.4. Confocal scanning optical microscopy (CSOM)

Confocal scanning optical microscopy (CSOM) is a microscopy technique that uses light from a laser through the objective of a standard light microscope to excite a specimen within a narrow plane of focus. In addition to scanning the specimen in the X and Y dimensions, CSOM can control the focal plane by raising and lowering the microscope stage. Using a stepper motor, the stage can be stepped in tiny increments (0.1 µm) through a sample. The software controlling the microscope can store the image information as it steps through a sample, allowing a true 3D dimensional analysis of specimens.

Wear damage quantification by means of CSOM were performed on WC/Co balls and aluminum wires used in tribological laboratory test. After scratch tests, the aluminum adhered volumes on the hardmetal ball surface subjected to Al 1370 and Al-2%TiC tribo-contact as well as the profile section of each track (acquired at the middle of the track) were obtained through confocal scanning optical microscopy (PLµ2300, SENSOFAR, Spain) and then processed with image analysis software (Mountains, Digital Surf, France). The specific adhesive wear rate (K) (nondimensional) was computed in agreement with Holm-Archard equation (3) [32]. The aluminum volume adhered on the WC/Co ball in lubricated conditions was acquired at the end of the scratch test in order to maintain the lubrication layer integrity.

To sum up, Chapter 3 has presented the methodology for collection of data for the selected cases study. Surface improvements were prioritized on the burnished surfaces and the wear mechanisms that affect the surface conditions and their improvements on the tool and feedstock materials of the wire drawing process. In both cases, the study has been done from a tribological perspective, as a suitable approach to track improvements on the tool and part surface integrity.

Chapter 4

Influence of the Stainless-Steel Microstructure on Tribological Behavior and Surface Integrity after Ball Burnishing: experimental approach and numerical simulation validation

Ball burnishing is a plastic deformation process that reduces roughness while increasing hardness by introducing compressive residual stresses near the surface zone [35]. These improvements will depend mainly on one fundamental variable: the applied load. However, another essential parameter derived from the applied load must be established, which is the friction resulting from the tool-surface interaction. But, friction will also depend on the nature of the surfaces in contact. Therefore, the microstructural differences in the treated materials have to be considered within this interaction, otherwise, the generalization in the process setup can lead to the early failure of industrial components. Consequently, this study reveals that surface improvements (surface finish and residual stress state) also depend on the tribological interaction degree between the ball and a defined microstructure. Accordingly, a martensitic precipitation-hardened UNS S46500 stainless-steel and an austenitic AISI 316 stainless-steel with textured surfaces are evaluated under the same milling and burnishing process conditions. The effect of friction on surface integrity in terms of surface roughness and the induced residual stresses has been determined in this chapter. Thus, this tribological interaction is now conceptualized experimentally by the friction coefficient.

Stainless steels are widely used in several industries. Since turning and milling are the traditional processes for machining these materials, the existence of irregularities and defects is inherent. These unevenness in the metal surfaces cause considerable energy dissipation (friction), surface wear and fracture over their lifetime [127]. To minimize these troubles, a reduction of roughness and an increase of mechanical properties are requested [1,128]. Consequently, ball burnishing process highlights [40,129]. Nevertheless, the burnishing of reinforced martensitic stainless-steel components (such as UNS S46500) has not been studied until now, enabling to innovate in the upgrading of the surfaces of this material. UNS S46500 is a stainless-steel typified by the presence of nanometric precipitates of Ni_3Ti in a martensitic matrix [130]. The limited previous work reports the ability of the process to introduce a deep and highly compressive layer on martensitic steel surfaces, with the location of the maximum

value at the subsurface level, being influenced mainly by the applied load [2]. High loads cause shear stress towards the surface [55]. However, undue loading causes excessive shear stress and thereby premature degradation of the surface finish [4,33,34,55,58]. Then, a proper operational parameters selection is a must to obtain an optimal surface integrity in terms of both surface roughness and residual stress state.

With all the aforementioned, there is a need of a valid and versatile model to optimize a particular ball burnishing process. This model should adjust to the mechanical properties of several materials (i.e., to their microstructures), to their initial surface integrity conditions (after milling or turning previous operations) as well as to the tribological tool-part interaction thorough the COF.

Thus, several simplified simulations have been settled to optimize the ball burnishing of steel components. However, their conceptualization has not contemplated the tool-part interaction, triggering an unsatisfactory process parameterization. In that sense, Amini et al. [37] eliminated these simplifications in their 3D ball burnishing numerical model on a pre-textured AISI 1038 steel surface. This structured numerical model has been established to reproduce this interaction by various friction coefficient approximations. To extend the applicability of Amini et al. model to other ferrous materials (skipping one of the FEM limitations [79]), this study delivers the tribological process inputs (friction and initial surface integrity conditions) to this model, adjusting it to the UNS S46500 milled martensitic precipitation hardening stainless-steel.

In order to evaluate different tribo-contact scenarios as well as their numerical conceptualization accuracy, ball burnishing experiments have been performed under two loading conditions, 270 N and 470 N. These two load levels entail two different friction coefficients and therefore, a different final surface and subsurface quality (reproduced by the 3D FEM model with accuracy). Hence, the numerical model is able to emulate the deformation induced by the maximum residual tensor and its affectation spread in depth (as is stated experimentally [55]).

Then, the adaptability of ball burnishing numerical simulation with a martensitic stainless-steel component has been investigated and experimentally validated. In that manner this work also contributes to the search for a reliable and versatile numerical tool for the future steel ball burnishing performance.

4.1. Results

4.1.1. Friction

In order to evaluate the microstructural response to the tribo-contact during the burnishing process and to provide the tribological inputs to the model, the COF was computed for each of the studied stainless-steels. Figure 4.1 summarizes the COFs generated by the interactions of austenitic and martensitic milled textured surfaces as a function of the contact pressure. The friction on the already characterized AISI 1038 ferritic steel textured surface [4] was established for comparison purposes.
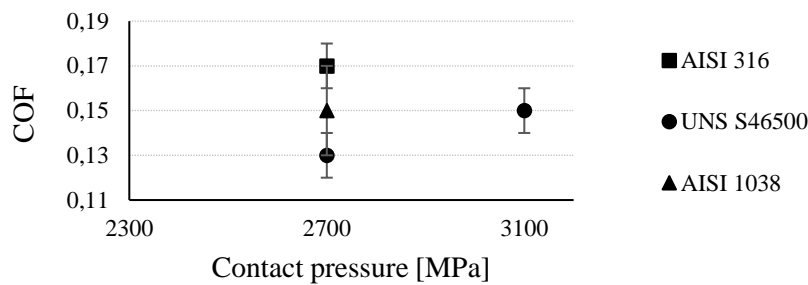
Figure 4.1. COF at different contact pressures

Under the same ball-burnishing configuration, the steels microstructure responses were not coincident. The COF on austenitic steel (0.17) exceeded the COF on ferritic steel (0.15) by 15%. The gap between the austenitic (0.17) and martensitic (0.13) stainless-steels COFs are 30 % different. This means that the frictional shear stress and, therefore, the surface finish and compressive layer induced by the process will be substantially different. After load increment on the martensitic surface, the friction coefficient increased. Henceforth, it is convenient to take into account the tribological performance of the process (which includes the COF, initial roughness, and initial stress state of the target material [37]) in order to achieve a particular surface integrity depending on the machined microstructure.

4.1.2. Surface topography

4.1.2.1. Surface topography: influence of stainless-steels microstructure

Figure 4.2 displays the milled and burnished areas (4 mm × 4 mm) of each target surface in order to provide the qualitative effect of the burnishing operation under the stated operational and tribological conditions. It can be observed that the topography conferred by surface milling

was more prominent on the austenitic stainless-steel than on the martensitic stainless-steel. However, under the same burnishing conditions, the topography of the austenitic milled surface disappeared and was replaced by an imprint of the burnishing tool (Figure 4.2c), showing the extent of the contact area, as well as the magnification of the interaction between the ball and the surface. Regarding the surface finish obtained on the martensitic steel, a softened topography can be seen in comparison with the AISI 316 surface under the same conditions (270 N). It can also be observed that the peaks intensified as the load increased (470 N).

(**a**) AISI 316 milled surface   (**b**) S46500 milled surface

(**c**) AISI316 burnished surface   (**d**) S46500 burnished surface   (**e**) S46500 burnished surface

270 N   270 N   470 N
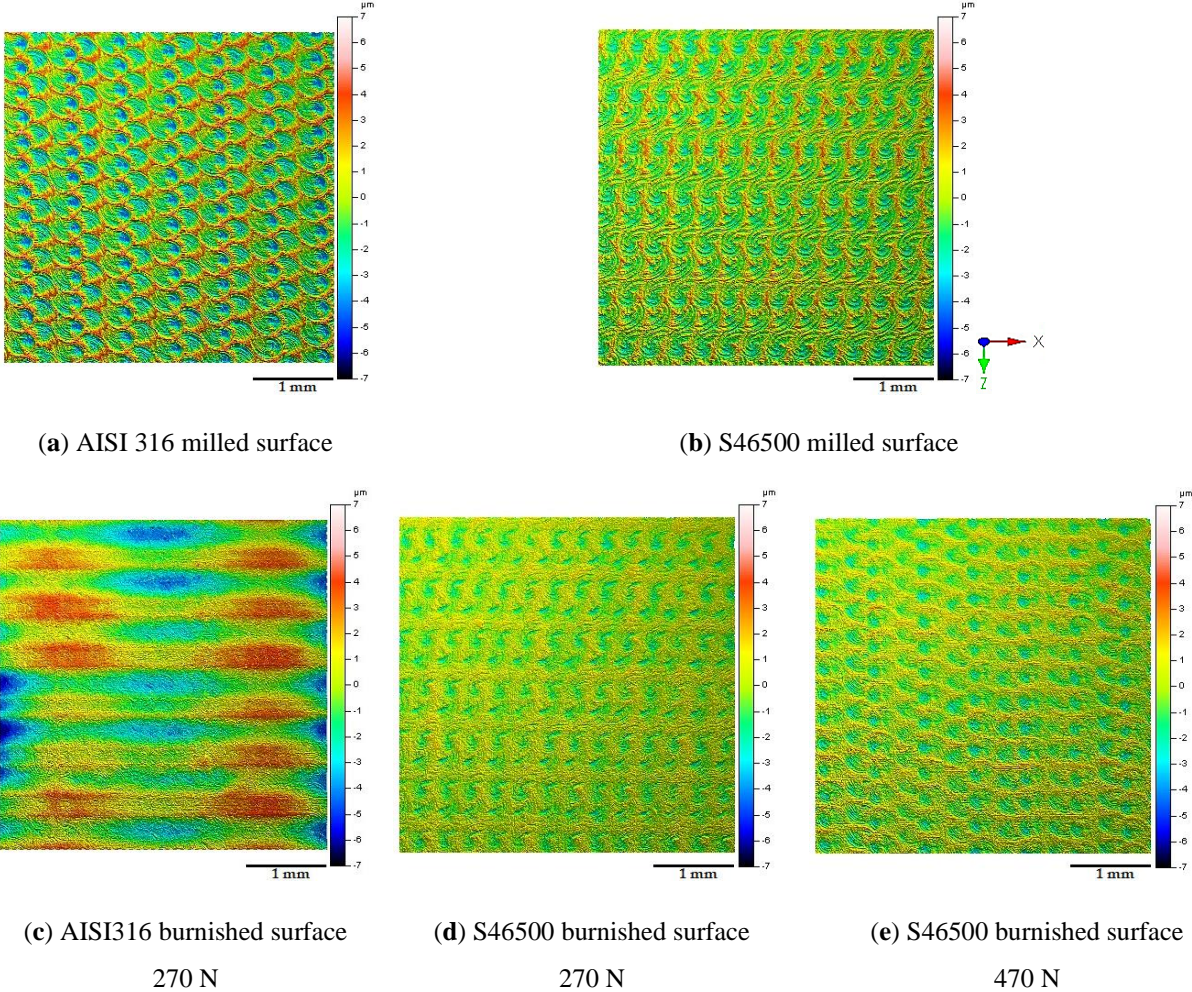
Figure 4.2. Textured surfaces after milling and burnishing at different contact pressures

According to this outcomes, Figure 4.3 summarizes the roughness parameters obtained after milling and ball burnishing in order to provide a quantitative description of the analyzed surface modifications.
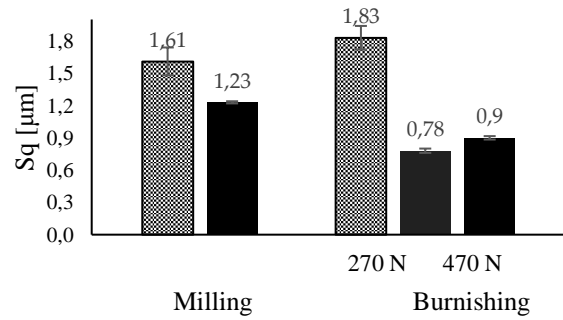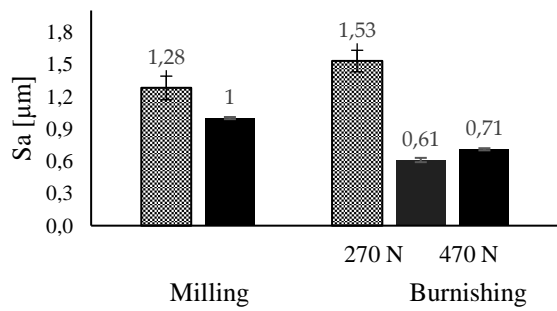
(**a**) Sa

(**b**) Sq
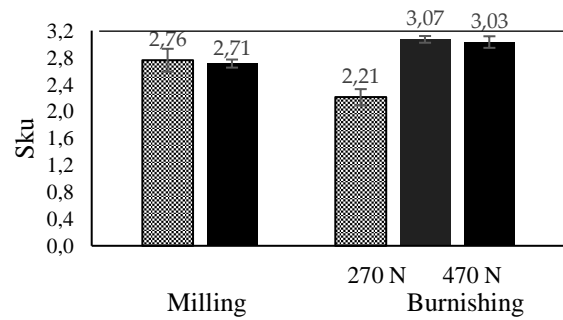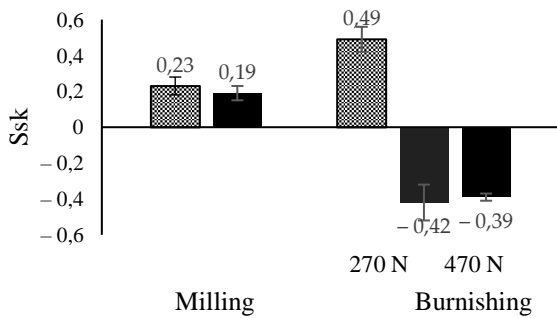
(**c**) Ssk

(**d**) Sku
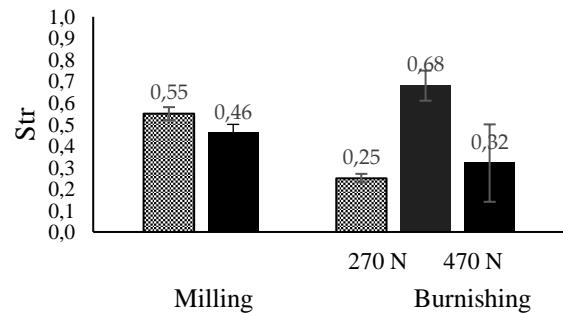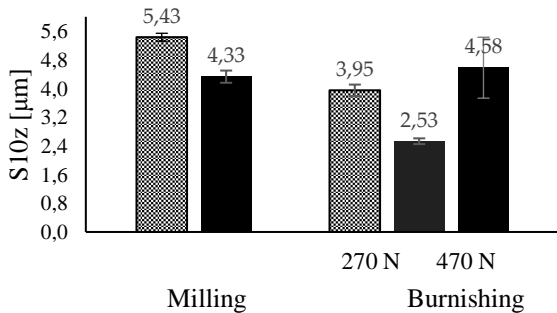
(**e**) S$_{10z}$

(**f**) Str

AISI 316 UNS S46500

Figure 4.3. Textured surfaces after milling and burnishing at different contact pressures

Based on the height parameters Sa and Sq, a normal distribution of heights (Sa = 0.8 Sq) was evidenced under milling conditions for both materials. This observation was corroborated by the skewness values (Ssk ~ 0) under the same milling conditions. This tendency varied after ball burnishing. Thus, under the same load conditions, the statistical asymmetry after burnishing on AISI 316 stainless-steel showed a mass distribution skewed to below the mean plane (Ssk > 0), while the surface of UNS S46500 stainless-steel is skewed to above the main plane (Ssk < 0) in equal proportion. The load increment on the second one slightly varied under this condition. With regard to kurtosis (Sku ~ 3), it was observed that the austenitic surface became a non-abrupt platykurtic condition, whereas the martensitic surface responded with a better fit

to a Gaussian distribution despite the load increase. The S_{10z} parameter provides a practical criterion for the statistical behavior of the height. It reveals that the five-point peak height and five-point pit depth were 20% more prominent on the austenitic surface. However, this was reduced by 36% on martensitic stainless-steel and only 20% on austenitic stainless-steel after ball burnishing. This was not consistent with Figure 2.5c. Since the austenitic crystal lattice (FCC) had a higher deformation capability (reflected in the COF value), a redistribution of the surface texture was evidenced. Thus, the new average roughness profile may have been displaced below the level of the initial valleys, leading to a loss of tolerance. On the other hand, increasing the pressure on the martensitic surface led to the generation of a pile-up and consequently an in-crease in the S10z parameter (~15%). This elucidates the marked differences in the surface roughness depending on the stainless-steel microstructure during the ball-burnishing process.

The directional properties quantified through the Str parameter were shown to be moderately isotropic (Str ~ 0.5) after milling for both surfaces. After ball burnishing, the austenitic surface became directionally anisotropic (Str < 0.3), whereas under the same conditions, the martensitic surface increased its isotropy. At a 470 N load, the martensitic surface became anisotropic.

4.1.2.2. Roughness: numerical model validation

In order to validate the simulation, numerical parameters Sa and Sq have been compared with the average of three experimental measurements obtained on a surface equal to and corresponding to the simulated area (0.9mm x 1.2mm):

■Experimental results ▨Numerical results
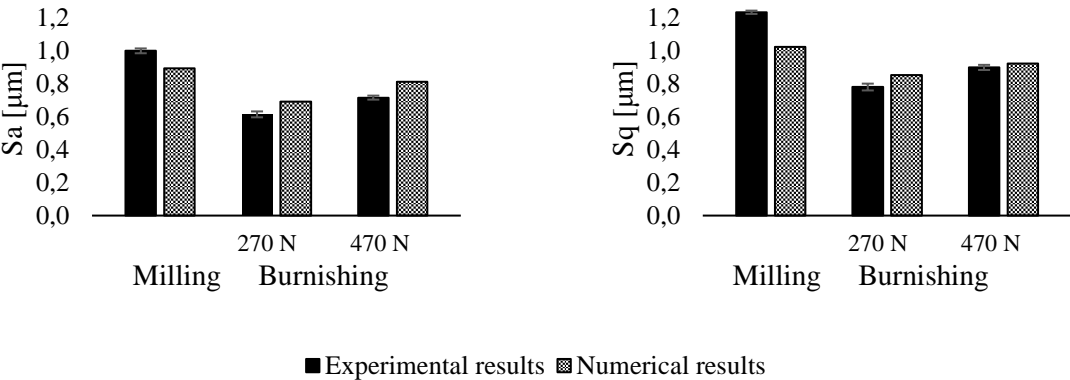
Figure 4.4. Surface amplitude descriptive parameters after machining processes

From Figure 4.4. it can be noted that despite the estimation of the initial roughness profile, results reveal that the numerical model can establish the performance of the target textured martensitic stainless-steel surface under the pressure stimulus transferred by the tool in terms

of roughness. Significant adjustments are obtained in the peaks and valleys distribution with respect to a median plane (Sa) as well as its dispersion (Sq). Hence, Figure 4.5 shows the topography evolution under the milling and burnishing conditions stated in Chapter 3 while the nodal displacement in the Y direction (Uy) from the simulation has been displayed in Figure 4.6.

Burnished surface at 270 N load   Milled Surface   Burnished surface at 470 N load
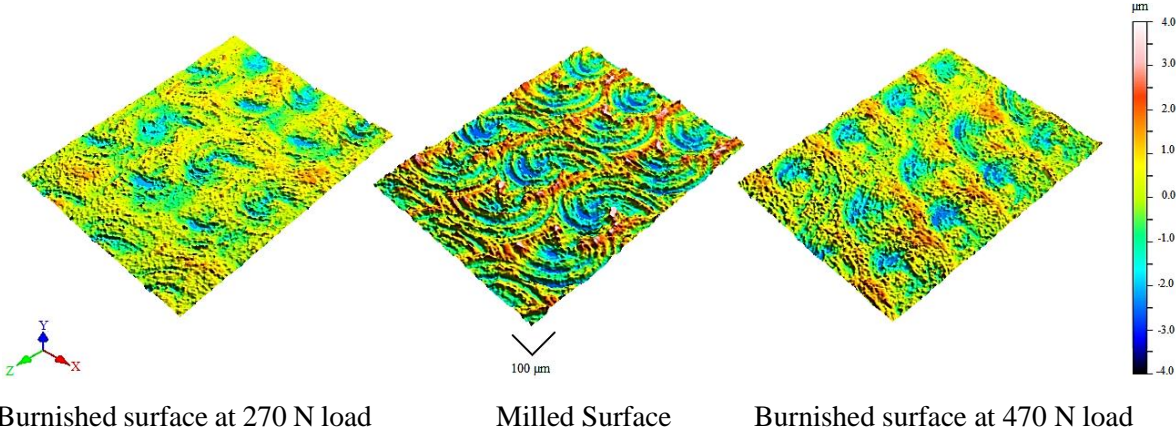
Figure 4.5. Experimental surface conditions after machining processes

Surface after burnishing at 270 N load   Surface after burnishing at 470 N load
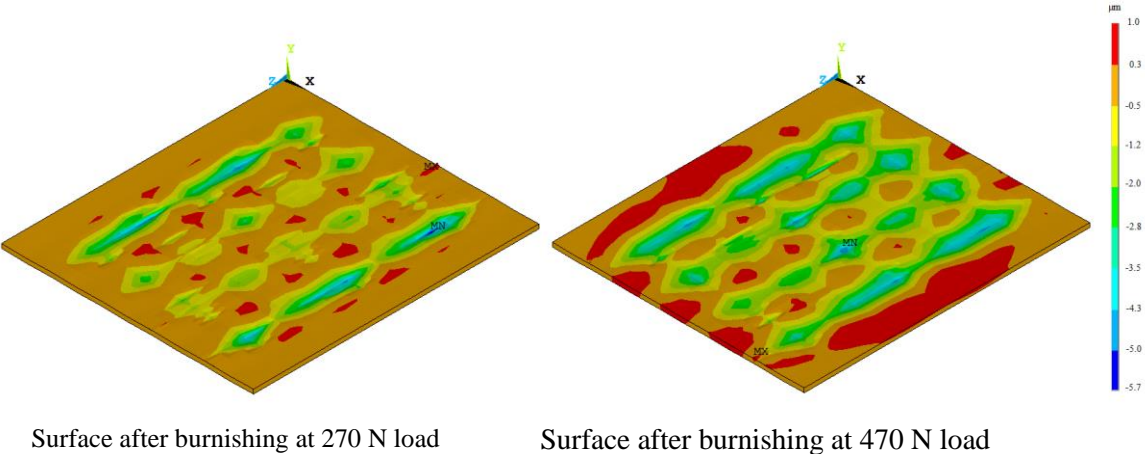
Figure 4.6. Surface topography after simulation

It is worth to note that Figure 4.6 values scale has been adjusted to the surface conditions prior to the ball burnishing execution. Nevertheless, Figure 4.5 and Figure 4.6 are comparable. In this regard, when the burnishing load increases, valleys are deeper (around 4 μm) than the initial value in the roughness profile (1.4 μm), both experimentally and numerically. Simulation results enlighten the material displacement out of the burnished area. Regarding the peaks, experimental data shows maximum around 1.5 μm while the simulation displays it as 1.0 μm, approximately. When ball burnishing is performed at 270 N load, the surface is smoothed consistently. On the other hand, when the load increases, the overlapping of material provides an irregular finish. Results reveal the effect of tribological interaction on the final surface.

4.1.3. Residual stresses

4.1.3.1. Residual stresses on the selected stainless-steels microstructure

Figure 4.7 summarizes the parallel (σ_x) and perpendicular (σ_z) tensor components of the burnishing path obtained after the milling and burnishing processes.
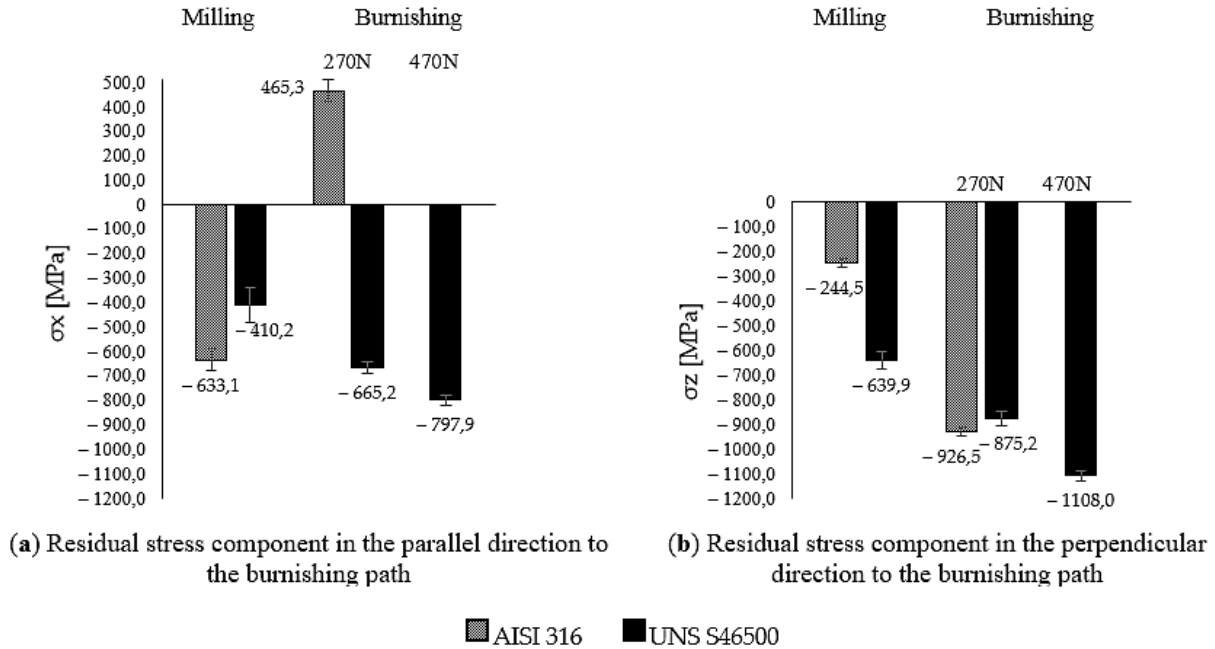
Figure 4.7. Residual tensor after milling and burnishing processes on stainless-steel surfaces

The residual tensor component introduced by milling on the austenitic surface was 61% higher in the parallel direction (σ_x) than in the perpendicular direction (σ_z) to the burnishing path. The opposite occurred on martensitic and ferritic surfaces [70], where the perpendicular component exceeded the parallel component by 45%. In this manner, although the mill feed rate on the austenitic surface increased the tensor component in its perpendicular direction, on the martensitic surfaces, it increased the tensor parallel to the milling route. However, after burnishing, on the austenitic surface there was a substantial increase in the lower compressive state component (σ_z) (4 times greater), whereas in the other direction (x-axis), a tensile state was induced. This extended the hypothesis of an anisotropic state independent of the initial tensor on ferritic surfaces [70] to austenitic surfaces. When burnishing was performed on the martensitic surface, the initial anisotropy was reduced by 9% at a 270 N load, whereas with increasing load, the anisotropy increased by 30%. Therefore, the residual isotropy was qualitatively in agreement with the directional isotropy (Str) for both materials after the burnishing process (Section 3.4.2). Regarding the skewness (Ssk), there was no evidence of a directly proportional relationship with the surface tensor, as mentioned in another study [80].

Depending on the microstructure, the surface integrity varied considerably under the same burnishing conditions.

4.1.3.2. Residual stresses as a parameter to model validation

Both parallel (σ_x) and perpendicular (σ_z) components of residual tensor to the burnishing direction at a depth of 4 μm were obtained by means of X-ray diffraction (XRD) for each condition. Comparison of experimental and numerical results for 270 N and 470 N is depicted in Figure 4.8. The values shown under the experimental bars represent the increased percentage of the residual stress component after burnishing compared to that obtained after milling process.
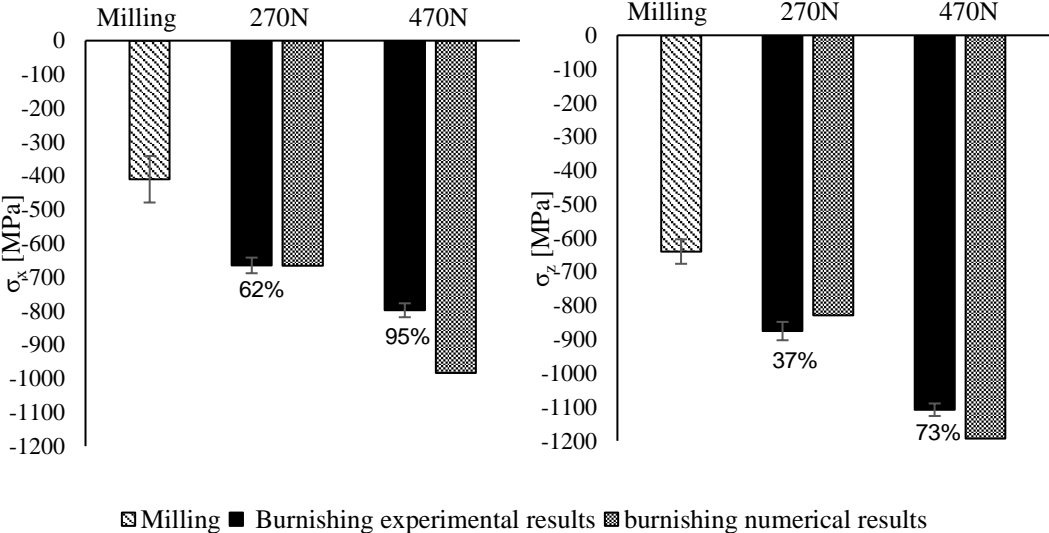
Figure 4.8. σ_x (left) and σ_z (right) components of residual tensor at a depth of 4 μm after machining processes (% values represent the increase of residual stresses compared to the milling condition in each of the simulated processes)

The adapted model started from an anisotropic surface configuration provided by the pre-machining process with the highest residual tensor component along the z-axis. Given that ball burnishing was performed in the perpendicular direction to this initial finishing (along the x-axis), results show that the greatest increase of the compressive residual stress component occurs in the parallel direction to the burnishing path (62% under 270 N load and 95% under 470 N load), with respect to the initial milling state. Thus, these burnishing configurations induce a greater effect in the direction in which the initial residual stress component is weaker (keeping the initial anisotropy trend. Thus, it is worth noting the ability of the model to reproduce this performance through the appropriate mechanical and tribological characterization, where the self-hardening coefficient (n) plays a significant role in the microstructural differentiation. When the simulation was performed at 470 N load, only a slight

mismatch appears in the parallel direction to the burnishing path with respect to the experimental values. Considering that the increase in contact pressure causes the displacement of peaks below the initial valleys (shallow decline), there will be an increase of the pile up, and therefore a larger divergence. Besides, the roughness profile has been extruded along the z-axis, so sharp peaks appear in x-direction. Consequently, these peaks act as a hinder to prevent plastic deformation along the x-axis. As a result, a higher stress than in experimental conditions is observed. The impact assessment of the proposed load conditions shows that the effect of 470 N exceeded the milling valleys below 4 μm depth. This implies a shift in the ball burnishing interaction, increasing the residual stress tensor perpendicular component to the burnishing path by 73% (more than twice the increase obtained at 270 N load). The lower friction coefficient obtained at 270 N load, leads to the fact that the small penetration of the ball into the deformed zones by the initial machining allows displacing part of the peaks towards the valleys, reinforcing the adjacent zone until constitutes a uniform surface as was observed in section 3.3.2. If this hypothesis is factual, the subsurface response should be different for both cases. In fact, simulation provides a first insight of the subsurface tensor behavior inside the characteristic range proposed by Chomienne et al. (300 μm) [35] by means of Figure 4.9.
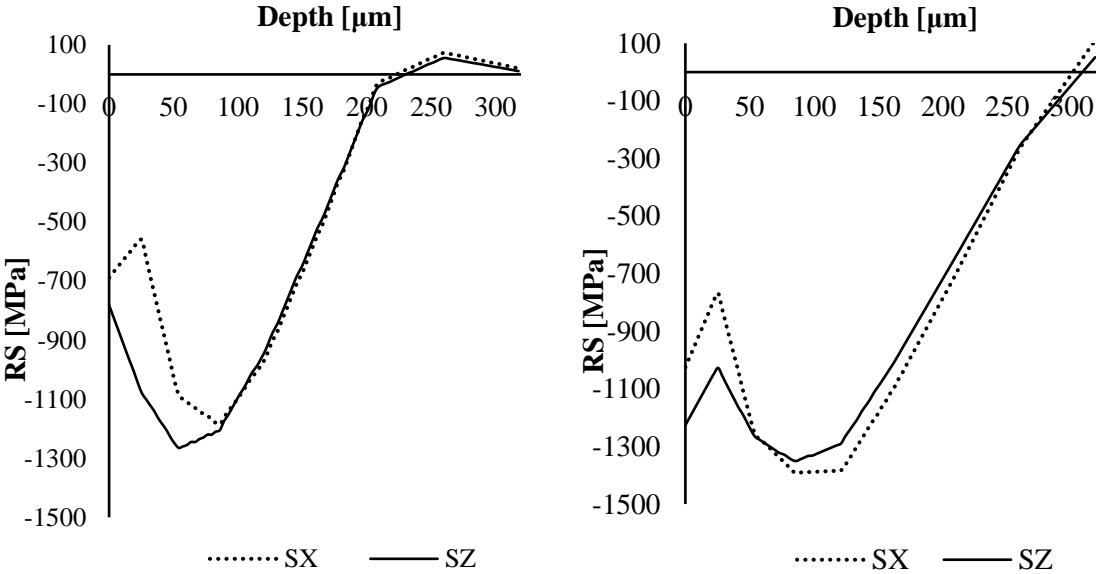
Residual tensor profile at 270 N load   Residual tensor profile at 470 N load

Figure 4.9. Residual stress state up to a depth of 300 μm after burnishing process obtained in the simulation

Data revealed the variability of the final tensor as a function of the applied load. Under 270 N load, the component of the residual surface tensor in the perpendicular direction to the process

tends to increase sub-superficially. On the other hand, it was observed that at 470 N, the residual tensor (both directions) gradually decreases up to 25 um in depth and then increases again. Nevertheless, Sz component (at 54 μm and 86 μm, respectively) is around 1265 MPa, under both load conditions. Another aspect to consider is the isotropic state that the material reaches early (~50 μm) under the highest load. Consequently, high tribological interaction involves both, less anisotropic affectation in depth as well as a reduction tensor in the first microns in the subsurface.

4.2. Discussion

The results elucidate the microstructural impact of the tribological behavior between the burnishing ball and the steel surface. According to Kuznetsov et al. [55], friction constitutes a fundamental parameter to obtain significant improvements or unwanted effects on surface integrity. Therefore, the consequences of high friction in ball burnishing processes, involves the generation of uniaxial tensile stress in the rear zone behind the indenter [55], as well as the increase in the pile-up [37]. However, based on the tribo-contact effects on the selected microstructures, the definitions of high and low friction are ambiguous. The allowable tribo-interaction ranges within the process will be given by the limited plastic deformation of the microstructure. In fact, the stress state conditions after ball burnishing with a 270 N load on the austenitic steel show the presence of a tensile state in the burnishing path direction (x-axis), which is in agreement with the approach of Kuznetsov et al. [55]. A clearly detrimental austenitic surface, reflected in the increase in the roughness parameters; (Figure 4.3) and a residual anisotropic state [37,87] beyond the compressive condition (Figure 4.7) were evidenced. Consequently, a new finish distribution (skipping tolerances) with valleys and peaks defined by the ball track (Figure 4.2 c) was displayed. This high plastic deformation capacity of the austenitic crystallographic lattice allowed for low surface integrity. Nevertheless, under the same conditions (270 N), the textured martensitic stainless-steel surface offered a contrasting microstructural response to the ball burnishing process. The lower COF (Figure 4.1) as an effect of the martensitic matrix, determined the displacement of the peaks toward the milling valleys, conferring uniformity on the surface (Figure 4.2 d), whereas the compressive surface state improved in both directions according to the initial trend established by the milling finish. A higher COF (0.17 after load increment) led to the compressive layers relocation to the surface (as stated by Kuznetsov et al. [55]), a heightening anisotropy (under 270 N) (Figure

4.7), and an onset of pile-up (Figure 4.2). As seen in Figure 4.7, the new pressure exerted on the martensitic surface was far from inducing a tensile state in the parallel direction on the burnishing path (which defines high friction [55]) so the hypothesis of high tribo-interactions on this material was limited to the pile-up initiation. Therefore, defining the burnished components functionality is pertinent. The process configuration must be prioritized, either the contact interactions with other components (roughness) [37] or the exposure to the corrosion, wear, and fatigue conditions whose resistance improves through the generation or increment of the surface compressive residual state [4,36,40,41,136]. It should be noted that determining the compressive layers thickness (sub-surface residual state) as a function of the tribo-interaction degree may modify the high-friction hypothesis of martensitic steels established in this study. Nevertheless, excessive tribo-interaction (overloading) within the process must be prevented in order to allow the treated microstructures to retain some degree of ductility, as cited by Kuznetsov et al. [55].

Taking into account all the above, it is clear that a ball burnishing simulation model that considers both, microstructure and the actual friction is key to a satisfactory operational parametrization of the process. In that sense, in this work, it was proved that 3D Amini's model simulation it is not limited to a specific steel. By introducing the mechanical and tribological properties of the material and eliminating the first simplification considered in other models [36,38,51,71,83,84]) by including the COF between the roughness and the hard ball, the simulation allows to predict the final surface integrity. Despite the irregularities in the roughness profile after milling process, its approximation to the maximum and minimum points (peaks and valleys), permitted to obtain fairly accurate numerical results in the final roughness. Model captured material overlapping adjacent to the burnishing direction (pile up) when ball burnishing proceeded at 470 N load. Otherwise, a uniform surface finishing was achieved at 270 N load. Thus, the effect of friction as well as the assertion of the applied load as a fundamental parameter on the surface integrity deterioration [35,36,38,55,64] are evidenced and validated.

Regarding the new compression residual state [37,44,47-50], enhancements are not limited to the surface [35,37,51,52,54]. According to Chomienne et al. [1], simulation elucidates the bulk affectation of the process over martensitic microstructures (until 300 μm depth), which is also validated in this work. The maximum compression state up to 100 μm in depth [35] has validated as well. The 3D FEM model reflects that high applied burnishing loads (470 N) induces a maximum value of residual stress tensor at the surface (4 μm) in response to the tribo-

contact (higher COF). Under 270 N load, the maximum value is reached within the 50 μm and a noticeable anisotropic residual stress tensor distribution is imposed. According with Capilla-González et al. [58], as the load increases, the isotropy tendency increases. Simulation validates this statement while allows to exhibit the residual stress tensor distribution depending on the tribo-contact between the ball and the textured surface (because of the shift on the applied load).

Therefore, an increase in load involves a bidirectional compression effect. Besides, unlike the ferritic steels [37,54,81], martensitic stainless-steels replay in a different way to this plastic deformation mechanism as reported in the literature [35,49,52]. Substantial improvements in the compression residual state have been obtained in the parallel direction to the burnishing route, although the anisotropic trend remains in the perpendicular direction (as was quoted by [37,51,58,70]). These results demonstrate the flexibility of the model. Therefore, it is worth emphasizing the great importance of supplying a real COF for a successful model adjustment, since the final numerical integrity is substantially dependent on the friction coefficient, as it was demonstrated also in the previous model for ferritic steels [37].

4.3. Partial conclusions

In the quest to enhance the surface finish and mechanical properties of stainless-steels using a ball-burnishing process, the tribological performance of the process must be considered. The interaction capability between the ball and the machined surface, quantified by the friction coefficient, defines the surface integrity improvements of the burnished components. Neither the friction value nor its effects are trivial during the ball-burnishing setup. Therefore, to obtain a balance between roughness reduction, design tolerance, and directional and residual anisotropy, or to prioritize one of them, a pertinent COF must be defined. Hence, the present work provides the starting point for a new methodology to parameterize the process. This methodology is based on the tribological tool-part interaction (in terms of COF) as a factual variable in the current numerical methodologies.

In addition, this study provides the friction effect on two previously textured microstructures (austenitic and martensitic surfaces) in order to contribute to the guidelines for future ball-burnishing crystalline plasticity numerical conceptualization while demonstrating the process's capability of enhancing the surface integrity of martensitic stainless-steel UNS S46500. The microstructural deformation mechanisms at the local level due to the different tribo-contacts

(dislocations, crystallographic orientations, recrystallization, hardness modification, self-hardening), as well as their effect on the thickness of the compressive layer, should be addressed in further research.

Additionally, this study demonstrates the applicability of the Amini et al. [37] structured 3D ball-burnishing numerical simulation (initially configured according to roughness, initial residual condition and friction during ball – milled AISI 1038 steel surfaces contact) adapted to the tribological interaction between the tool and a martensitic stainless-steel surface. Beyond the limitations dictated by a customized FEM configuration for each material, this work shows the versatility of the model because of:

- Numerical 3D roughness parameters as well as the final topography have a convincing agreement with the experimental values. The model limitation to introduce the experimental roughness profile was successfully overcome by approximating the average profile to a sinusoidal wave that considers maximum peaks and minimum valleys. It is noteworthy how after the 2D roughness profile extrusion into the model, a representative surface-weighted pattern of the whole surface was obtained to finally achieve a numerical fit of the Sa and Sq parameters to the experimental outcomes after ball burnishing process. This simulation reproduced the detrimental effects of load and friction increase on the surface quality by a higher dispersion (Sq) in the arithmetical mean heigh (Sa) distribution (valleys reach the 4 μm depth when the initial values were around 1.4 μm).

- A cramped mismatch in terms of residual stress tensor in one of four directions, did not alter either its trend (anisotropy) or the final surface integrity. The increase in contact pressure involved a shallow slump causing a larger divergence. Additionally, the peaks of the roughness profile (restricted to maximum values of experimental peaks) extruded along the z-axis, constitute sharp elements that work as obstacles, obstructing the plastic deformation along the advance route. Nevertheless, despite the higher stress obtained numerically with respect to the experimental values in x-axis direction (a difference of about 200 MPa), the process parameterization can be validated quantitatively as a function of the component applicability (which defines the residual stress conditions) by means of this simulation.

- An approximation of the subsurface stress behavior (up to 300 μm in depth) verifies both the depth extent and the load affectation degree in the final isotropic state cited in previous works. When the process is performed under 270 N load, the surface finish is

improved as the residual tensor increases continuously until 54 μm depth, keeping the anisotropy trend. Under 470 N, the surface residual tensor is higher but tends to shrink during the first microns. Furthermore, this strong interaction leads to a detrimental surface integrity and to an early isotropic state. However, subsurface behavior is out of the reach of the current study since it demands a detailed evaluation at the microstructural level. Nevertheless, considering the relevance of this material applications future experimental and numerical investigations on the microstructural behavior of this material under ball-burnishing should be done.

The outstanding results in terms of the final surface integrity highlighting the relevance of including friction as a fundamental parameter in the numerical process conceptualization. Therefore, the model has been validated with regard to its versatility constituting a useful and economical tool to define the most efficient path for ball burnishing processes on steels not yet studied (such as the UNS S46500 stainless-steel) and that require an increase of the surface quality of the final components.

Chapter 5

Analysis of Industrial Dies and Experimental Approach for Assessing the Tool-Part Tribological Interaction in Wire Drawing of Aluminum Reinforced Wires

The surface quality of a wire after the drawing process can vary depending on the lubrication and the surface condition of the dies. Hardmetal dies are widely used in wire drawing processes, due to its high hardness, good toughness and excellent wear resistance. Its surface condition is an essential parameter that directly influence the surface quality of the produced wire. Moreover, the surface integrity of hardmetal dies is a key factor to improve the tool life and the efficiency of the drawing process. Thus, the analysis of industrial dies after its service life is important to verify their final conditions and its relationship with different mechanisms of damage. In this chapter, different hardmetal dies used in wire drawing of steel, cooper and aluminum were evaluated in order to identify the main wear mechanisms in industrial drawing dies as a previous step to improve the surface integrity of the produced wires.

Once main wear mechanisms in wire drawing have been established, a particular wire drawing process has been analyzed to improve the final wire surface quality. In this chapter a thorough study of different wear reduction strategies on hardmetal dies has been performed to enhance the final quality of aluminum reinforced wires to be used as a feedstock in wire arc additive manufacturing technique.

Among the numerous application procedures of additive manufacturing (AM) [131,132], wire arc additive manufacturing (WAAM) [140] outstands for its adaptability to well-known wire feed welding technologies [134-136]. WAAM uses metal wire as the material feedstock and an electric arc as a heat energy source. The arc melts the wire, and each layer is deposited on top of each other by a robot arm until a desired 3D shape is build layer-by-layer [135]. The ability of printing large metal parts with superior deposition rate, high density, improved mechanical properties, and low costs [131-133,136,137] are some of its advantages. For those reasons, a great number of industries can be benefited of WAAM technology in order to quickly fabricate metal parts, remanufacture heavy-industry parts, fix molds and dies or repair metal parts on-site. Thus, the WAAM process can be widely used in several industries, from lightweight

applications in automotive and aerospace, to construction and packaging, where aluminum takes a crucial role [111,133-138]. Nevertheless, since in WAAM processes the molten wire is used as a filler material that ignites the arc when it meets the metal base [135], cracking and porosity are the biggest drawbacks of aluminum WAAM pieces [139]. Then, a wire feedstock that prevents crack growth and pore formation is required [139,140]. To overcome crack susceptibility, the insertion of nanoparticles of nucleants into the feedstock [141,142] by promoting nucleation of fine and equiaxial grains during solidification have been proposed [139,141]. Accordingly, Langelandsvik [133,135,139] has dispersed TiC nanoparticles as reinforced material into aluminum alloys wires through a novel screw extrusion process [133], establishing an innovative metal matrix composites (MMCs) manufacturing procedure [131,142]. These hardened wires, after a diameter reduction post-processing, constitute the aluminum filler material for WAAM components without crack susceptibility. Then, it is in this post-processing where the second drawback of WAAM component porosity, is solved. It has been shown that final component porosity is mostly influenced by the WAAM feeding wire surface finish. The surface finish of the feedstock wire can influence the arc stability by the hydrogen content on the wire surface generating porosity during solidification [140]. Therefore, aluminum wires must satisfy the welding process requirements such as homogeneous diameter, surface integrity, low sliding friction, stiffness, and hardness [95,143]. Achieving these requirements depends mainly on the wire drawing tribological performance during the post-processing of the wire reduction diameter. [2,95].

In the present study, the desired diameter for WAAM aluminum application ranges from 1.2 mm to 1.6 mm [143]. The characterization and optimization of the hardmetal die – aluminum base alloy [6] interaction, inextricably linked to friction and wear, guaranties the best WAAM feedstock surface quality reducing porosity and then improving the final integrity of the printed component.

To obtain an effective deformation of the wire during its passage through the die it is necessary to minimize the friction generated by the sliding contact [2,95]. For that reason, on one hand, the intrinsic characteristics of the process, such as die geometry, area reduction, feed rate and lubrication need to be optimal [2,82,95]. On the other hand, tool wear, as the principal factor that drastically affects wire tolerances and die service life must be minimized [94]. Therefore, the understanding of the die wear mechanisms and the factors that control the COF are crucial to improve both wire surface quality and tool life. The high-pressures reached during wire drawing process entails adhesion as a main wear mechanism, resulting in a COF increase during

the wire drawing process [2,21,95]. As a result, the aluminum adhered locally in the die [23,82,112], has a high oxygen concentration and higher hardness compared to the original feedstock [144]. This sticky aluminum induces a two-body abrasion [1,145,146] on the wire surface. Besides, it implies a force increase to break the aluminum bond on the tool, leading to aluminum debris generation (micro-plough) [82] and triggering the chevron crack formation in the nascent material coming in front of both the released abrasive particles at the interface, and the adhesive cluster bonding to the hardmetal surface (micro-cut) [23,95]. The free-moving solid particles, whose detachment is facilitated in the presence of a second phase (TiC) in the wire material (Al) [147], are added to the tool-wire interaction inducing a third-body wear mechanism [145,146]. In third-body abrasion, hard particles are free to roll and slide during the contact affecting friction either reducing it forming a transfer film during their bearing or increasing it if the debris inside the interface distorts the wear track [146].

Because of the aforementioned wear mechanisms, marked scratches or striations following the sliding direction are observed in the softer material, the processed aluminum wire [32], resulting in a defective and dimensionally inaccurate product [94]. In addition, it has been reported that the size of the scratch marks observed on the tool correspond to the size of the spall out tungsten carbide grains of the hardmetal tool [96]. There is scarce literature in the field of drawing processes, but some works have reported cavities left by the WC dislodged during machining of aluminum on the WC/Co tool surface due to a preferential wear of its softer binder (Co) [96-100]. Moreover, recent advances in improvements of hardmetal tools wear during continuous sliding contact with soft materials (copper) mentioned this phenomenon; however, its characterization remains in the early stages of development [101]. Thus, the presence of third-body abrasion implies a micro-cutting effect increment due to hard free particles (WC). At that point, micro-cutting effect is repeated several times on the emerging feedstock surface, entailing a ductile microfracture [95,102] known as crow's feet [95]. These microfractures are caused by high local stress concentration on the surface wire due to the micro-cutting that results in a micro-fatigue state on localized parts of the drawn wire [23]. Therefore, third-body abrasion as a consequence of aluminum adhesion in hardmetal dies, constitutes a main problem in terms of wire surface quality, since it allows the propagation of fatigue failure [103] and the retention of impurities on the surface [95]. Moreover, tool service life is also affected due to continuous loss of surface material and consequent matrix weakening [95,102].

In order to reduce these tool and wire detrimental effects, optimal lubrication and the use of coatings as a complement, are mandatory. A proper lubrication strategy reduces adhesion, power, heat, friction, and tool wear while a better surface finished wire is obtained [2,148]. In that sense, it is convenient that the lubricant adheres to the surfaces to reduce friction [2]. Thus, the roughness conditions of the surfaces in contact govern the lubrication regime by voids acting as reservoirs influencing the contact area and local stresses that lead to wear [105]. According to previous studies, wear in the die tool has been considerably reduced both by the effect of TiC nanoparticles in the aluminum alloy matrix, even in dry conditions [108], as well as using coatings on the tool surface [103,107,111]. It has been proved that coating films provides a lower COF, increased thermal and mechanical fatigue and wear resistance to the metal forming tools [103,111,114]. Besides, coatings constitute a shield against Co wear in hardemetal tools, being that even in lubricated conditions [82], the Al adhesion on the tool surface and its effects persist [103]. For this purpose, the use of low friction coatings as diamond-like carbon (DLC) [110-114] has been proved effective. DLC coatings constitute a technological solution to reduce the tool wear mechanisms [114], becoming industrially relevant due to their noteworthy tribological characteristics [110-114]. In that sense, Vidales et al. [114] have evaluated the tribological performance of a-C:H/Cr and a-C:H/CrN amorphous hydrogenated carbon coatings deposited on WC/Co balls while interacting with Al 5754 discs under lubricated conditions. It has been proved that the use of these DLC coatings reduce the tool wear caused by aluminum transfer during the forming process. Furthermore, regarding the drawing Al alloy production, the hardness and roughness of the films must be taken into account in terms of compatibility with the lubricant [103].

Therefore, this study pursues two aims. First, to characterize the hardmetal wear mechanisms critically influenced by the presence of TiC nanoparticles in a WAAM aluminum wire feedstock during sliding contact. Then, once the critical wear mechanisms are identified, the study seeks to optimize the hardmetal-wire tribological behavior through lubrication and DLC coatings strategies implementation. For this purpose, a scratch test has been modified (described in Chapter 3) to use a ball-on-wire configuration under dry and lubricated conditions. Then, the resulting scratch tracks as well as the uncoated and coated hardmetal contact surface have been characterized by both FE-SEM and energy dispersive x-ray analysis (EDX), to identify the sought-after WC/Co wear damage mechanisms and wire defects (lumps, inclusions, scratches, chevron cracking or commonly known as crow's feet). In addition, confocal scanning optical microscopy (CSOM) has been used to compute both the adhesive wear rate on the

WC/Co ball and the aluminum wire surface topography generated because of each scratch configuration. The results of this study show that aluminum adhesion on the hardmetal surface is mitigated by the introduction of TiC nanoparticles as aluminum wire reinforcement and suppressed by DLC coating on the hardmetal surface. Thus, this work document the initial stages of the main wear mechanisms resulting between the hardmetal and Al 1370 and Al-2%TiC tribo-interactions, and their potential solutions, constituting a prior and indispensable stage in the wire drawing optimization. The results obtained in this study is an attempt to reduce the porosity in the final 3D printed components to improve the reinforced WAAM feedstocks surface quality, while extending drawing tool life using amorphous hydrogenated carbon coating strategies.

5.1. Preliminary experimental findings

As a first step to enhance wire surface quality in wire drawing, it is necessary to determine the influence of both the friction and the wear mechanisms on the die tool. Sliding contact will occur during the wire drawing process between the die tool and the wire, thus reducing the wear in the die tool means to improve wire surface quality. In that sense, industrial hardemetal die after service life tools has been analyzes in order to determine the main wear mechanisms affecting wire surface quality during wire drawing. Three different wire drawing processes have been selected for this propose:

- High and medium carbon steel wire drawing for industrial applications and mattress manufacturing springs.
- Cu-Ag wire drawing for transport applications
- Aluminum wire drawing

5.1.1. Characterization of hardmetal dies employed in steel wire drawing

The WC/Co dies surface characterization employed in steel wire drawing process after their service life was performed by means of SEM and SCOM techniques. In the development of this section, three hardmetal dies from different manufacturers were selected according to the diameter reduction rate (Table 5.1).

Table 5.1. Dies geometry and reduction percentage

Dies	A	B	C
Ø max	3.98	7.87	5.49
Ø min	2.43	4.66	3.38
% reduction	0.63	0.65	0.62

First of all, providing that dies come from different manufacturers, a characterization of the WC/Co quality was performed by means of its grain size. Figure 5.1 shows the grain size acquired by means of EBSD, and the distribution of the grain size. The analysis of the grain size of WC/Co is key to classify the quality of the hardmetal dies according to Figure 2.21.
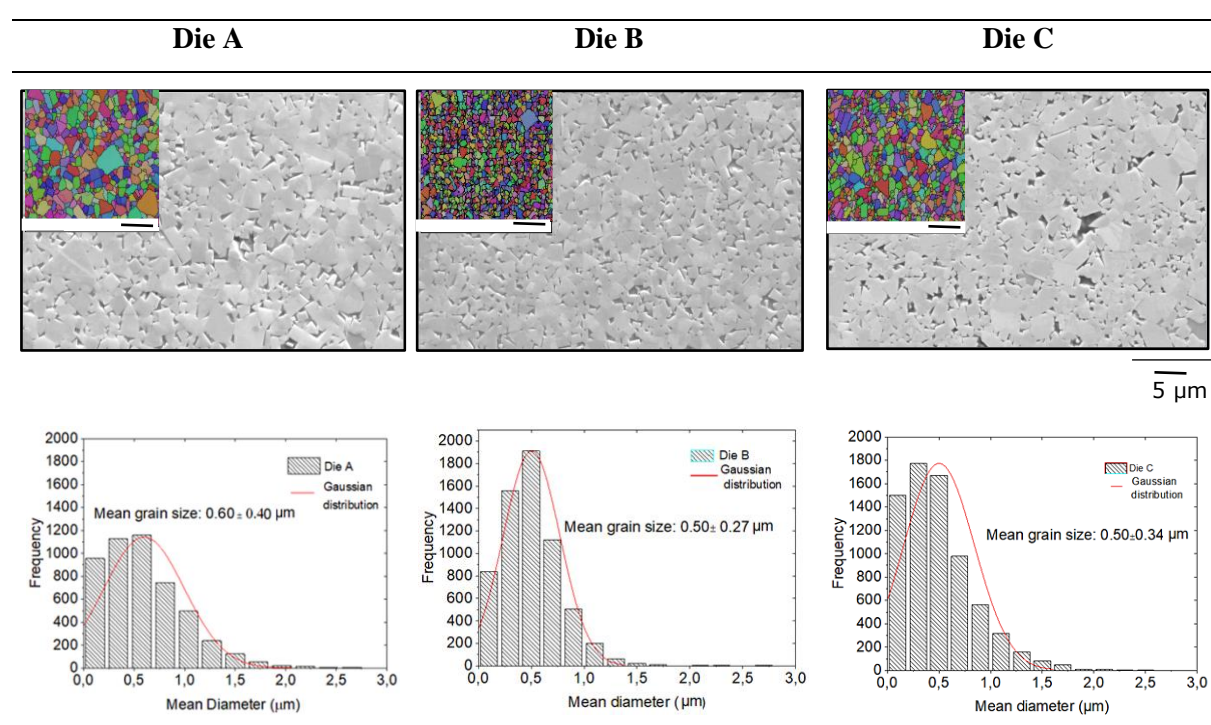
Figure 5.1. WC/Co grain size obtained by EBSD

According to the measured main grain size and the Fachverband Pulvermetallurgie of WC-Co microstructures (Figure 2.21), die A shows a high content of ultra-fine grain, followed by a submicron size and small quantities of fine and medium size, which increases its toughness. The mean grain size for dies B and C is between ultrafine and submicron with small quantities fine grains.

Die geometry can be divided into three zones, as described in Chapter 2. The first contact point between the wire and the die zone o Z1, the working cone zone o Z2 and the bearing at the die exit zone or Z3 (Figure 2.17). Generally, zones 1 and 2 show uniform surfaces, however it could be observed peaks that are related to a deficient die initial polishing rather than to be formed

during the drawing process. On the other hand, zone 3, considered as the critical zone in terms of wear, presents considerable alterations in its topography. In this regard, in this study the surface quality of the die in zone 3 were analyzed by means of SCOM. The selected relevant roughness parameters to define the surface quality were Ra and Sdr. Figure 5.2 shows the obtained results for the three analyzed industrial dies:
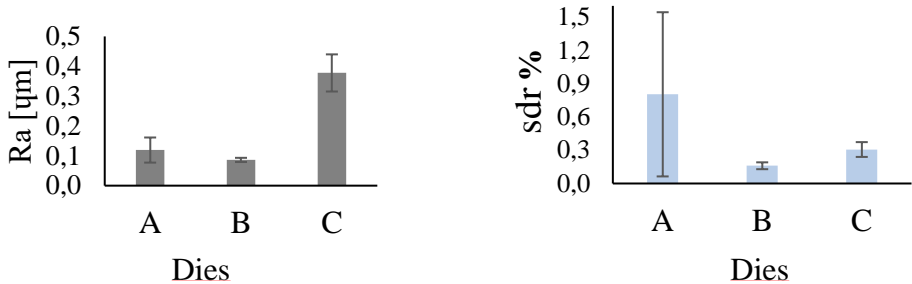
Figure 5.2. Roughness parameters acquired as a mean of three measures in zone 3

In terms of Ra, die C presents a higher roughness, while die A is the one that presents higher Sdr showing a large deviation. . Sdr is affected both by texture amplitude and spacing, in die C with a higher Ra indicated that has a wider spaced texture but die A with a low Ra and high Sdr indicate a finer space texture. Then, in die C and die B the surface trend is more uniform but with the presence of peaks in specific places. The computed surface qualities indicate that adhesion as a wear mechanism is more probable in die A, than in die C or B.

Finally, the surface of the dies was inspected by means of SEM (morphology and topography) and EDX (semi-quantitative chemical composition). Figure 5.3 clearly shows the presence of a white layer induced by the electrical discharge machining (EDM) cutting process. This white layer, as explained in Chapter 2, reduces the surface integrity of the die in detrimental to its service life as well as the surface quality of the wire.
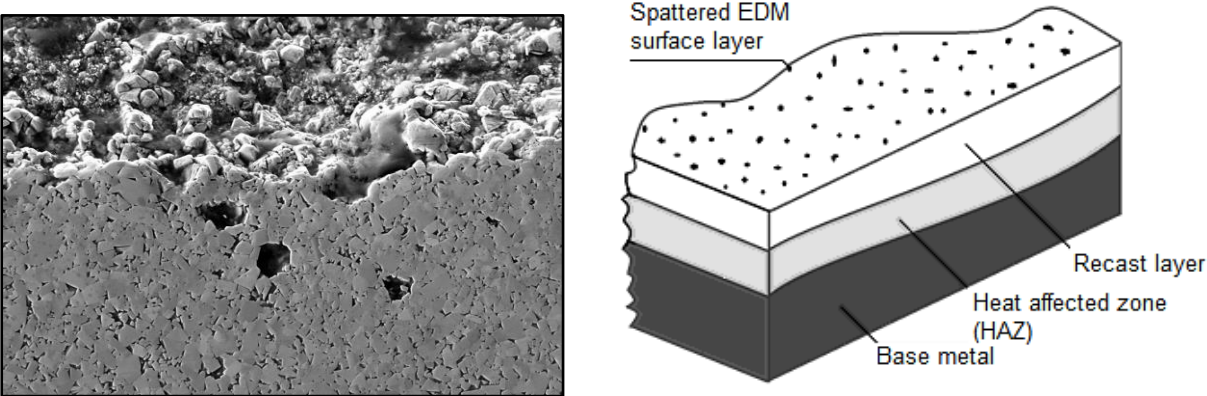
Figure 5.3. EDM effect on the WC/Co surface

According to the literature, one of the most common damages in drawing dies occur due to an inadequate EDM manufacturing [10]. Tool damage is evidenced by a white layer on the surface of the material. The sparks produced during the EDM process melt the metal surface, which then undergo ultra rapid quenching [149]. Beneath the white layer is the heat affected zone. This layer is minimally affected by the carbon enrichment of the white layer, having been thermally treated, but not to the point of reaching melting temperature [9]. At this point, the heat affected zone retains the metallurgical structure of the parent material as the temperature absorbed is not to the level to change the structure. Then, the craters formed in the electrode are sources of defects, that increase with increasing energy [25]. Figure 5.4 shows the existence of a white layer on the surface of the three analyzed industrial dies, evidencing that this is a common defect on industrial applications. A surface characterized by metallic inclusions, micro-cracks and gas trapped in the white layer is observed for the three samples. The evident increase of surface roughness in the inner channel, front and cross section in the zone 3 of the die is an effect previously computed in Figure 5.2.
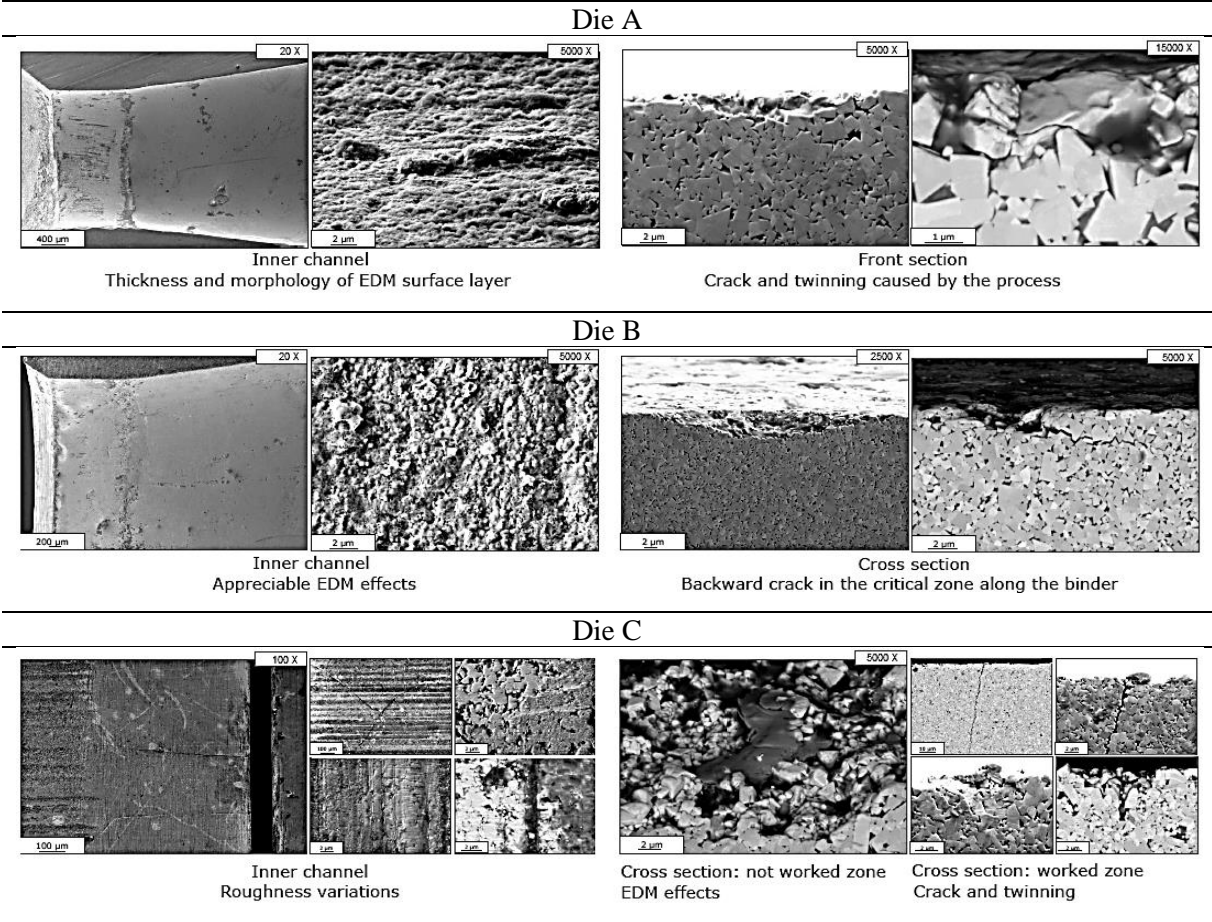
Figure 5. 4. Damage mechanisms in zone 3 on the WC/Co surface dies

The major concern is the amount of microcracks present in the dies. As seen in Figure 5.4, microcracking is extremely prominent as an effect of the presence of a white layer. If this layer

is too thick or is not removed by finer EDM finish or polishing, the effects of this microcracking can cause premature failure of the tool. Also, the existence of these microcracks reduces the material corrosion and fatigue resistance because they act like impurities reservoirs and stresses concentration zones, then surface integrity should be the primary consideration when evaluating the performance of EDM manufacturing.

5.1.2. Characterization of hardmetal dies employed in Cu-Ag wire drawing

The objective of this study is to characterize hardmetal dies after its useful life, in the Cu-Ag alloy catenaries production. In this application, hardmetal dies are submitted to a heat treatment to obtain a composition gradient (Figure 2.22) improving its performance in terms of hardness and fracture toughness.

Figure 5.5. Worn hardmetal tool used in catenaries production

The end of the die life is determined by the loss of the internal angle shown in Figure 5.6.
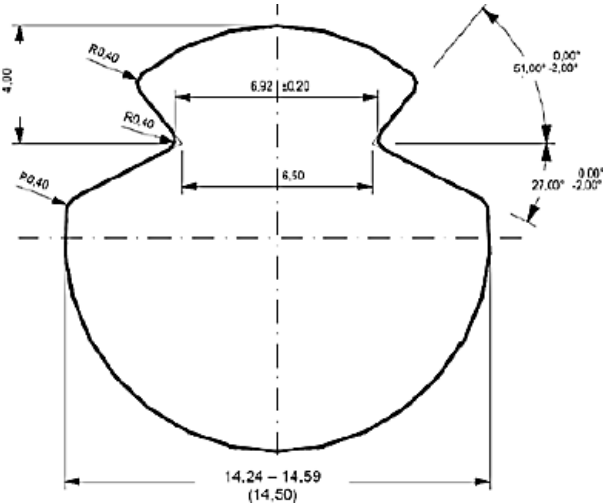
Figure 5.6. Configuration of BC-150 contact wire (dimensions in mm) according to EN 50149

Two dies, one new and one worn were compared by optical inspection, revealing the formation of the annular wear ring in the latter, a fact shown by Figure 5.7.

a) New die   b) worn die
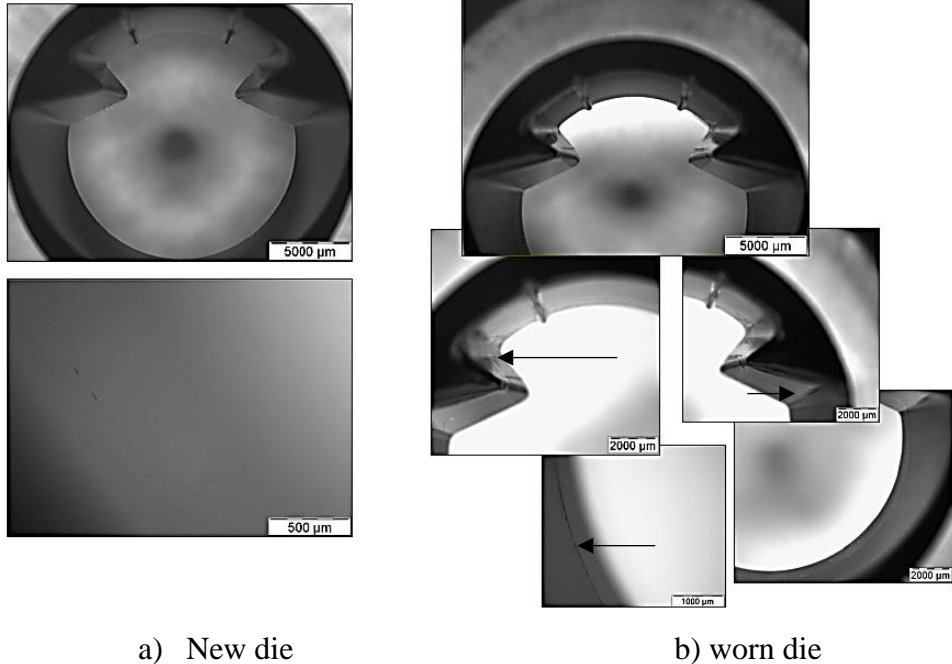
Figure 5.7. Optical microscopy images of the new and worn hardmetal dies

Then, in order to identify the hardmetal failure mechanisms during the Cu-Ag alloy wire drawing, Ra parameter in the critical zone on the internal surfaces of the new and worn dies have been obtained. Figure 5.8 shows the effects of the sliding contact on the die surfaces. The roughness in most of the surface is reduced as a consequence of the continuous interaction.
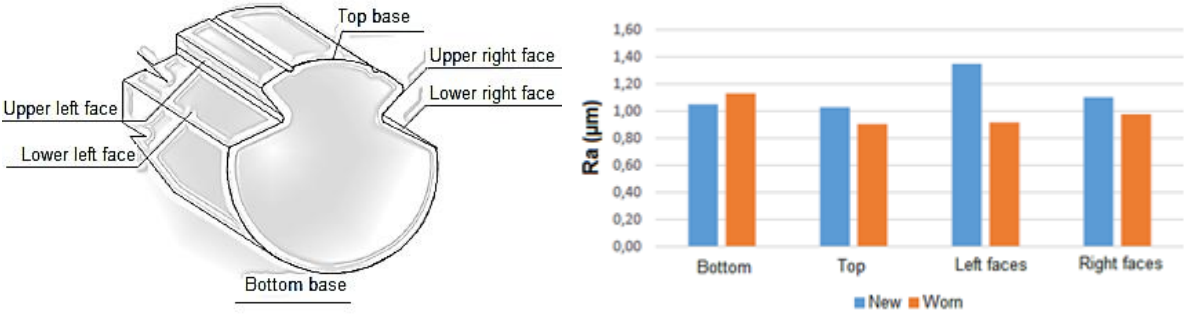
Figure 5.8. Critical zone Z3 roughness

Further on, micro-hardness of the worn die on the edge and on the bulk were measured to discern the gradient effects of the heat treatment on the mechanical properties. Table 5.2 shows these results.

Table 5.2. Worn die micro- hardness

Die area	Hardness HV1
Surface	2084 ± 26
Bulk	2069 ± 15

Additionally, to corroborate the heat treatment effects on the microstructure of the die, chemical composition and, in particular, the percentage of Co was quantified by EDX in both areas, with similar results, as Table 5.3 shows.

Table 5.3. Hardmetal chemical composition (wt.%)

Label	Surface	Bulk
C	10,56	10,39
Cr	0,13	0,13
Co	2,62	2,63
W	86,71	86,85

According to hardness values and the Co content, the effects of a heat treatment on the profile of the die were not observed, being this a possible cause of a premature failure of the die since the desired mechanical properties were not achieved.

On the other hand, a broken die was also characterized metallographically, in order to evaluate the fracture causes. The results are shown in Figure 5.9.
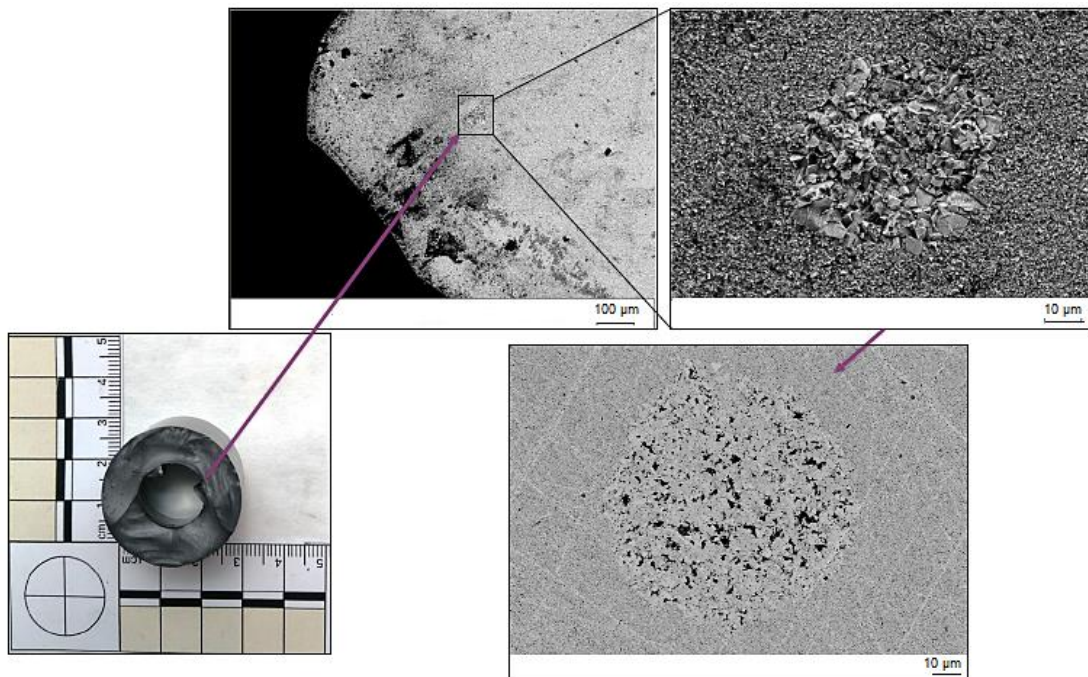
Figure 5.9. SEM images of a WC particles agglomeration defect in the fracture zone of the broken hardmetal die

WC particles agglomeration on several zones were identify. Thus, the previous analyzed worn die was prepared and evaluated under the same conditions that the broken die. The aim of this analysis is to compare hardmetal internal surfaces to understand if these defects are responsible to premature wear damage or fracture. Figure 5.10 shows SEM images of the worn die surface.
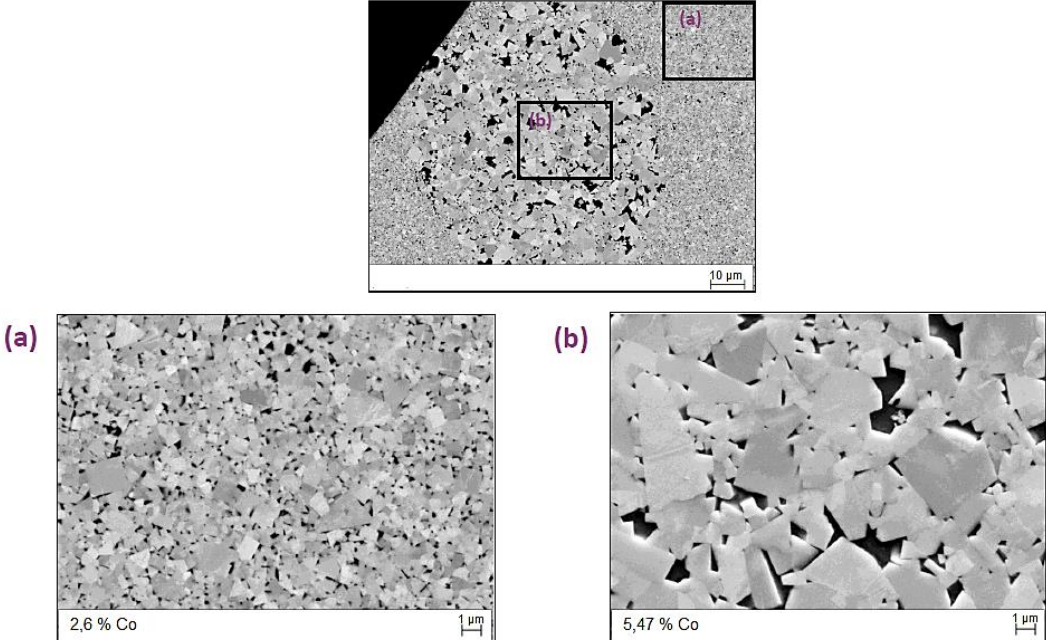
Figure 5.10. SEM images of defects observed in the worn hardmetal die surface: (a) WC/Co microstructure in an adjacent zone and (b) WC microstructure in the defect zone

In both broken and worn dies the presence of WC agglomerates with a different grain size and Co content were identified. Thus, it can be concluded that the dies were submitted to a deficient heat treatment process since there is a localized gradient near the surface, but the desired gradient profile it is not achieved. An inappropriate final microstructure of the die could be a critical factor regarding its premature failure and the final quality of the produced wire.

Then, the fracture zone of the worn and the broken die was assessed to establish the origin of the failure. Results are shown in Figure 5.11 and Figure 5.12, respectively.
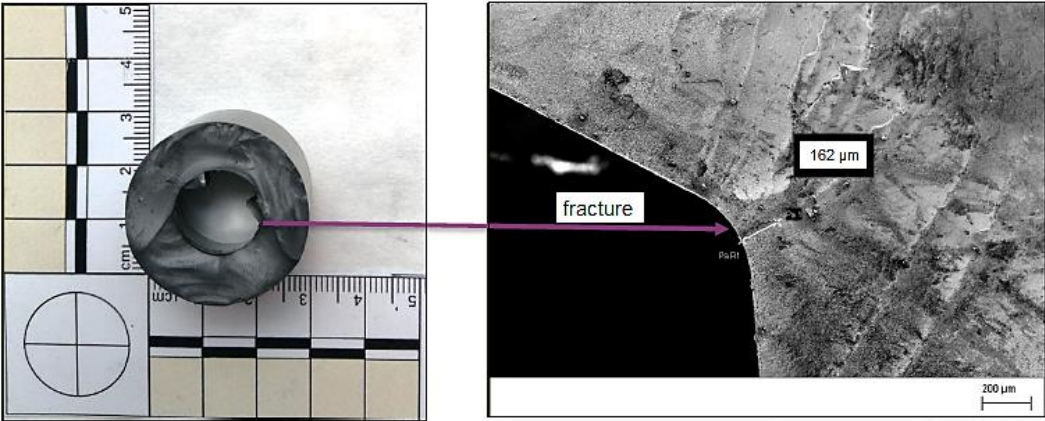
Figure 5.11. Fractures in the worn hardmetal die surface (bottom angle)
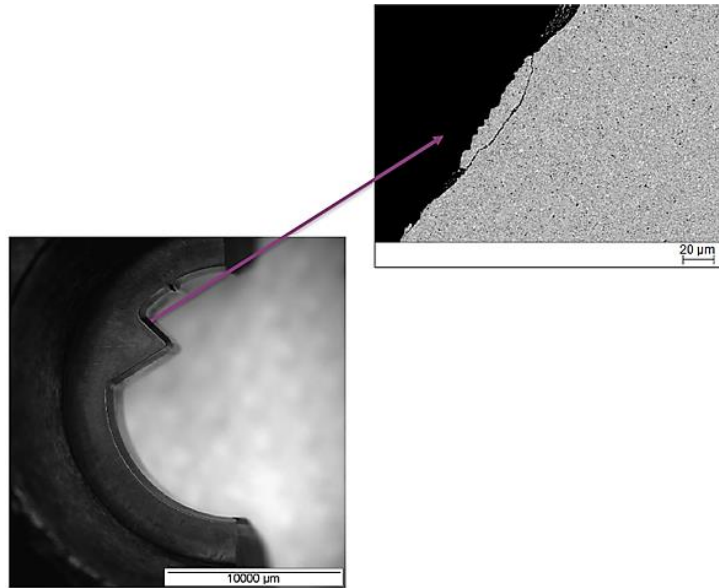
Figure 5.12. Fractures in the worn hardmetal die surface (upper angle)

It can be observed that WC agglomerates act as high hardness localized areas in the critical zones leading to the premature failure of the tool. Then, because of a deficient heat treatment, the final die has not the desired profile in neither microstructure nor mechanical properties, and premature failure of the dies is inevitable.

5.1.3. Characterization of hardmetal dies in Al wire drawing

In chapter 3 it has been detailed the industrial process of Al wire drawing. For the last wire diameter reduction, a hardmetal die is used and is considered the critical one in terms of surface quality of the Al wire. In that sense, it has been inspected to identify the main wear mechanisms affecting both service tool life and surface integrity of the Al wire. After its service life, a section of the hardmetal die was obtained, enabling the inspection of the central part of the die.

First, a classification of the hardmetal quality in terms of its mean grain size has been performed by means of SEM. Several images of the central part of the die were obtained and then the distribution of the carbide size was computed manually. As can be seen in Figure 5.13 (a), the microstructure of the hardmetal is not uniform from the surface to the inner part of the die. Thus, three zones have been identified: base material (inner part of the die), interface and outer layer (surface of the die). For that reason, additionally to the grain distribution, the chemical composition (EDX) of each of the identified zones have been measured. Figure 5.13 (b) and 5.13 (c) show the different percentage of Co and the different grain distribution in each of the identified zones, respectively.

(a)

(b)

(c)
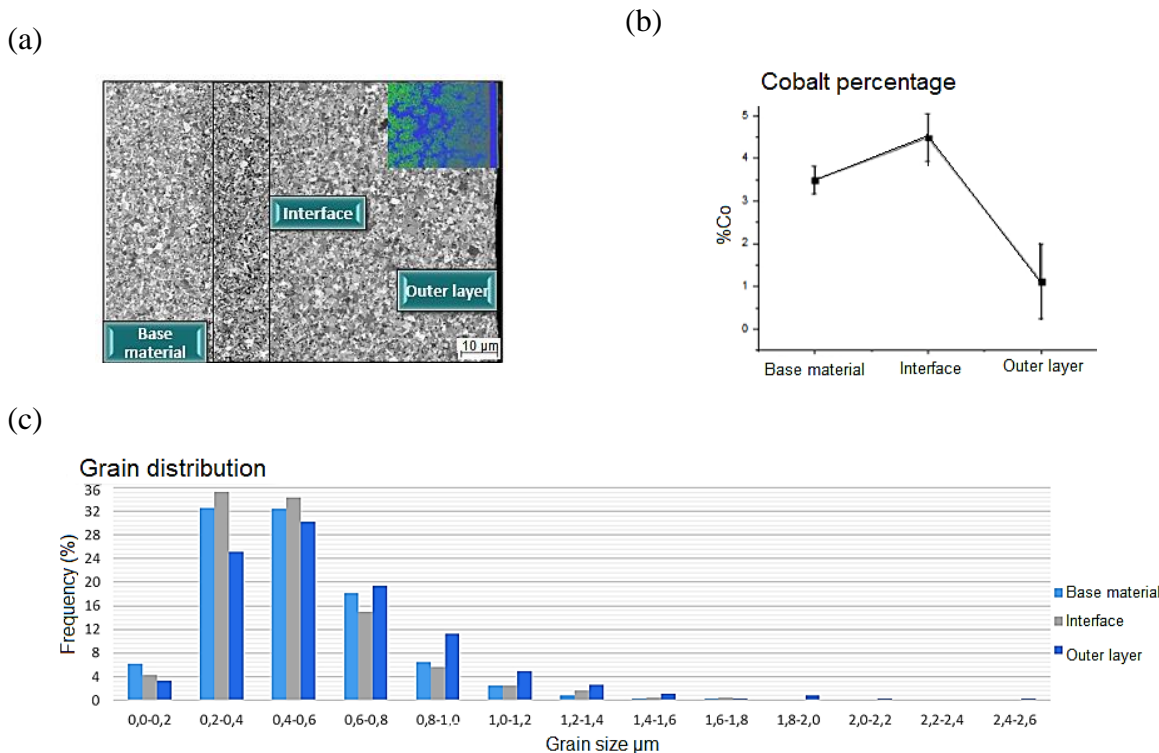
Figure 5.13. (a) SEM image of the microstructure of the die with the three identified zones (base material, interface, outer layer), (b) percentage of Co (in wt.%) and (c) grain size distribution in each of the identified zones

In Table 5.4 the mean grain size and the %Co in each of the identified zones is shown.

Table 5.4. hardmetal chemical composition (wt %)

Die Zone	Mean grain size [μm]	% Co [%wt.]
Base material	0,51 ± 0,22	3,49 ± 0,33
Interface	0,50 ± 0,24	4,49 ± 0,55
Outer layer	0,55 ± 0,24	1,11 ± 0,87

The results evidenced an inhomogeneous structure of the WC/Co of the die. According to the Fachverband Pulvermetallurgie of WC-Co microstructures (Figure 2.21), the grain size mostly ranges from ultrafine to submicron with different frequency, demonstrating a gradient occurrence. Regarding the percentage of binder, it is observed that the base material contains higher amounts of Co that the surface, but is the interlayer the zone with the highest amount of Co. A gradient of the WC/Co microstructure is a common practice to increase the combination of hardness and fracture toughness in the near surface-layer of the gradient hardmetal [150]. It can be expected that this kind of microstructures have a better wear-resistance and performance properties than conventional WC-Co materials. This functionally graded WC/Co is based on having a near-surface layer with a low Co content and a high hardness, as can be seen in Figure 5.14.
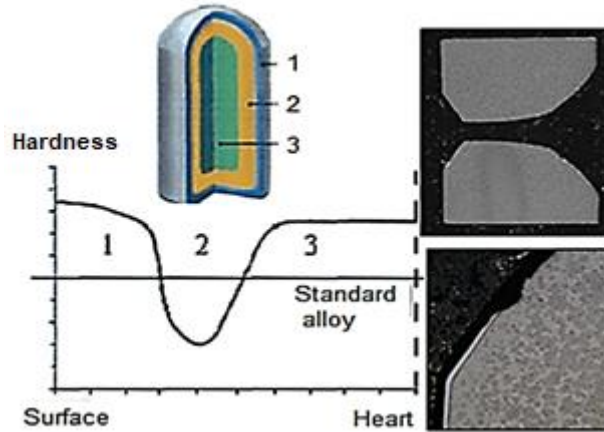
Figure 5.14. Functionally graded WC/Co and its effect on hardness [151]

In order to identify the main wear mechanisms of the die, an optical inspection of the worn die was performed. According to the observed graded microstructure, extreme wear mechanisms are not expected. Figure 5.15 shows a summary of the identified damage and wear mechanisms.
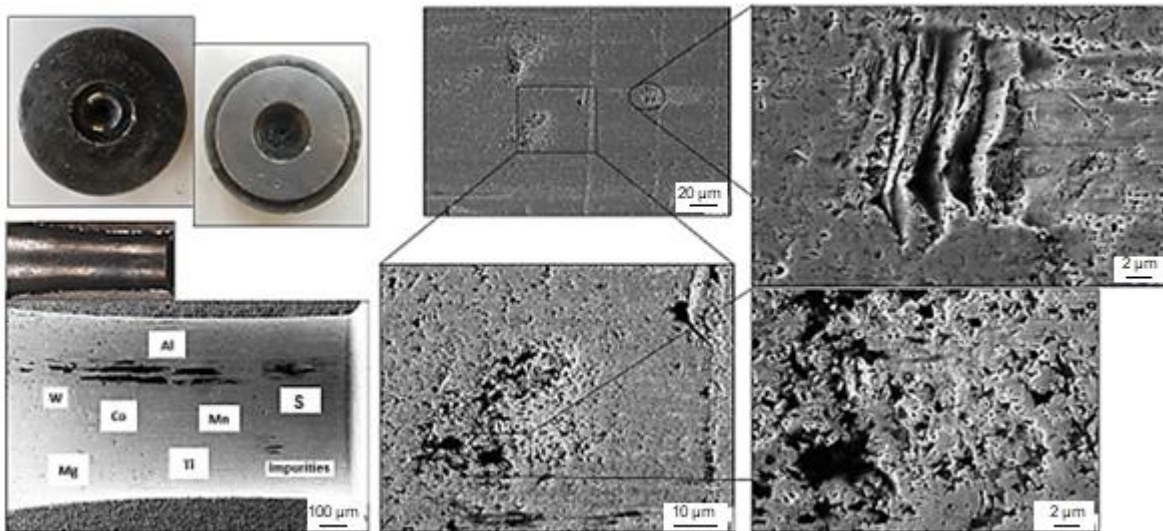
Figure 5.15. Worn WC/Co die critical area after aluminum wire drawing process

From this preliminary inspection, it could be noticed the presence of machining lines (as longitudinal scratches), abrasion (carbides detachment), adhesion, grain cracks, pitting and a possible chemical attack. This wear mechanisms are due to high pressures and therefore elevated friction probably because of a poor lubrication and presence of contaminants.

5.2. Results of the sliding interaction assessment between hardmetal and WAAM aluminum 1370 enhanced with TiC nanoparticles

In the previous section, it has been identified the main tool damages and wear mechanisms of WC/Co industrial dies in wire drawing processes. Defects during the machining of the die specific geometry is one of the main reasons of fractures and tool damage in WC/Co dies. On the other hand, abrasion and adhesion have been identified as the main wear existent mechanisms. Under the emerging demand in the process configuration for MMCs wire drawing, a characterization of the sliding contact interaction between a hardmetal and aluminum alloys: aluminum base (Al 1370) and aluminum reinforced with TiC nanoparticles (Al – 2%TiC) was performed taken into consideration the industrial dies analysis. In that sense, to reduce the effects of an inadequate machining, in this section it has been considered the sliding interaction between hardmetal and aluminum wires at laboratory scale. Under this premise, it is expected that defects in the tool due to wear mechanisms, can be mitigated or even suppressed. Thus, this work document the initial stages of the main wear mechanisms resulting between the hardmetal and Al 1073 and Al-2%TiC tribo-interactions, and their potential solutions, constituting a prior and indispensable stage in the wire drawing optimization. The results obtained in this study is an attempt to reduce the porosity in the final 3D printed components to improve the reinforced WAAM feedstocks surface quality, while extending drawing tool life using amorphous hydrogenated carbon coating strategies.

5.2.1. Influence of lubrication in friction coefficient and wear mechanisms identification during uncoated WC/Co ball drawing

The influence of the lubrication strategy in friction was evaluated by scratch test as described in Chapter 3. Figure 5.16 summarizes the COFs obtained in sliding conditions when an uncoated WC/Co ball is drawn over the polished surfaces of a 1.8 mm Al 1370 and Al-2%TiC wires. Three consecutive passes (unidirectional) were performed in dry and lubricated conditions in order to correlate aluminum adhesion on WC/Co ball with the COF.
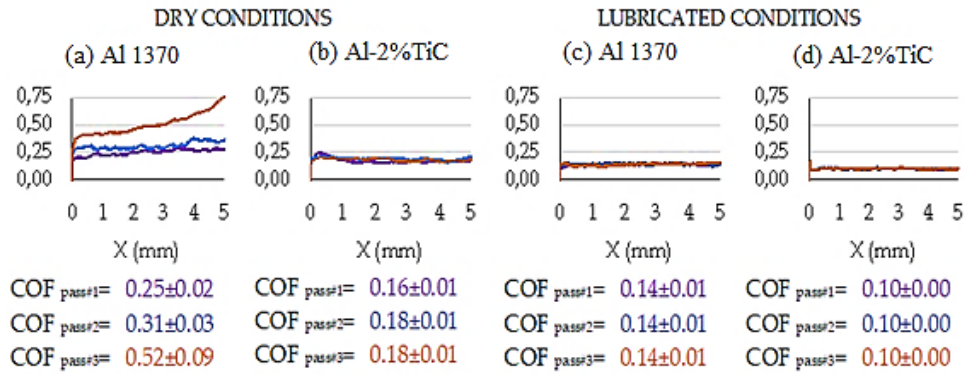
Figure 5.16. COF for Al 1370 wire and Al-2% TiC wire in dry conditions (a) and (b) respectively, and in lubricated conditions (c) and (d), respectively (COF mean values were obtained when the steady state is achieved, neglecting the running-in period)

In general, the presence of TiC particles improves COF behavior, reducing the mean value and stabilizing it along the tests. This tribological improvement is mainly due to the hardening effect (Section 3.2.1.2) of the nanometric TiC particles in the Al 1370 wires. On the contrary, Al 1370 wire increase its COF along the scratch test, while the use of lubrication results as an excellent strategy to reduce and stabilize COF.

In order to understand COF behavior, the wear damage mechanisms resulting of the contact during the scratch test were assessed by means of SEM and SCOM. Figure 5.17 exhibits the identified wear mechanisms on the WC/Co ball surface under dry conditions.
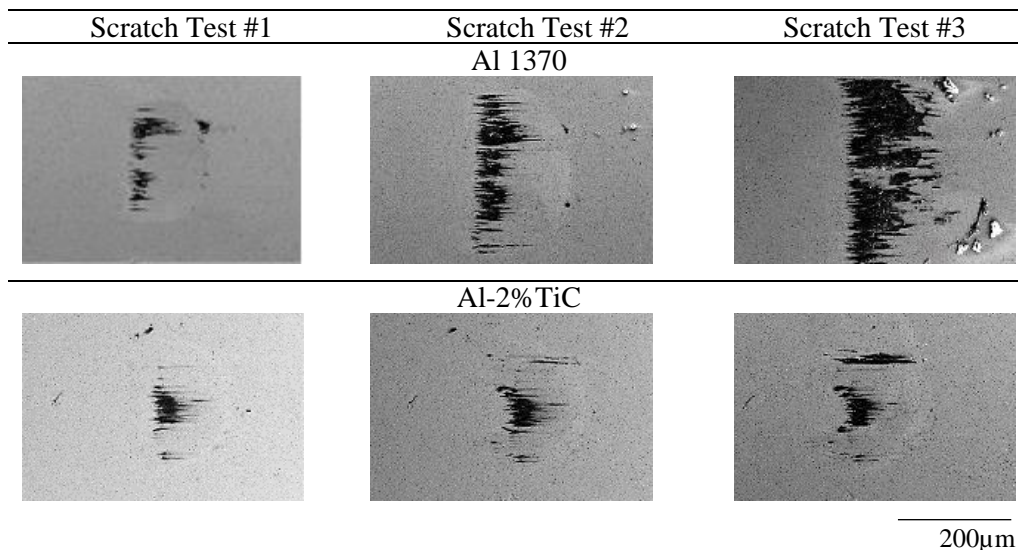
Figure 5.17. Adhesion mechanisms evolution on WC/Co ball surface after dry sliding contact

As can be seen, the main wear mechanism involved in the sliding contact between the hardmetal and the aluminum alloys is adhesion, depicted schematically in Figure 5.18. This mechanism involves both, alterations in the contact area of the ball and in the nascent material of the wire (Figure 5.19).
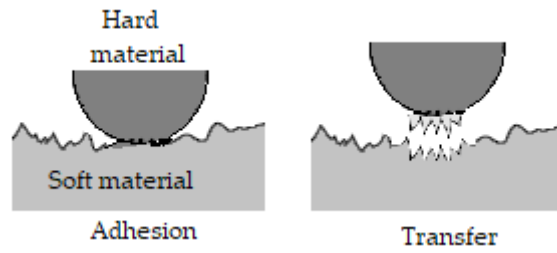
Figure 5.18. Adhesion mechanism during sliding contact

In order to evaluate the adhesion effects on the wire surfaces, Figure 5.19 shows, the SEM images of the scratch tracks in the wire surface, and in the bottom, their section profile, acquired by SCOM.
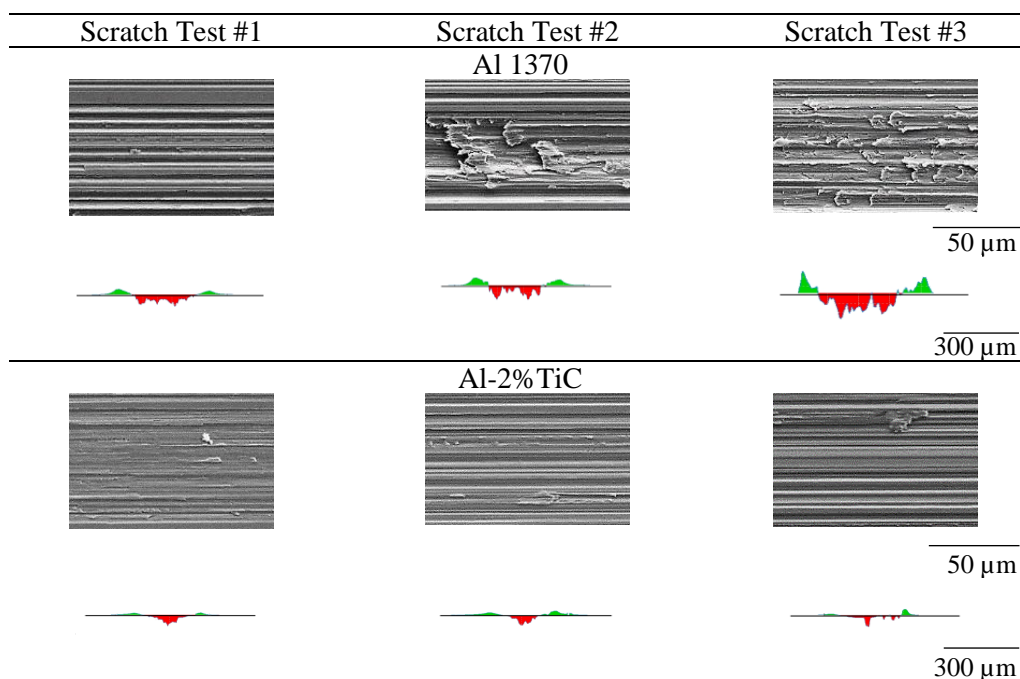
Figure 5.19. Wire track (longitudinal view and middle section profile in a range of ± 6 μm) after dry sliding contact

Figure 5.19 shows the importance of reducing aluminum adhesion on the WC/Co ball in order to improve the final surface quality of the wire. The presence of sturdy longitudinal grooves pronounced chipping and material clumps are directly linked with the wear rate and the COF. These grooves act as preferential points for material transfer in the form of aluminum adhesion. Moreover, because of the repeated sliding with the WC/Co ball surface meaning an increase of the material adhesion, aluminum can break of and act as free particles worsening the surface integrity of the wire. Figure 5.19 also shows that, while in dry conditions Al 1370 wire presents a series of ribs along the section track (in red), in presence of TiC particles, these ribs are presented with shallower and less broad profile. Then, adhesion is reduced in the presence of TiC particles, improving friction, wear and consequently the final surface quality of the WAAM

wire. To evaluate the lubrication effect in the ball wear damage as well as its influence on the track surface conditions, Figure 5.20 provides a preliminary view of the ball-surface sliding interaction under lubricated conditions.
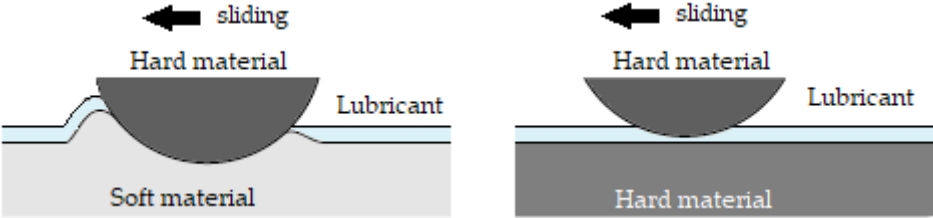
Figure 5.20. Ball- surface interaction resulting under lubricated sliding contact

According to the interaction represented in Figure 5.20, Figure 5.21 and Figure 5.22 show the SEM images and SCOM profiles on the ball and lubricated wires respectively.
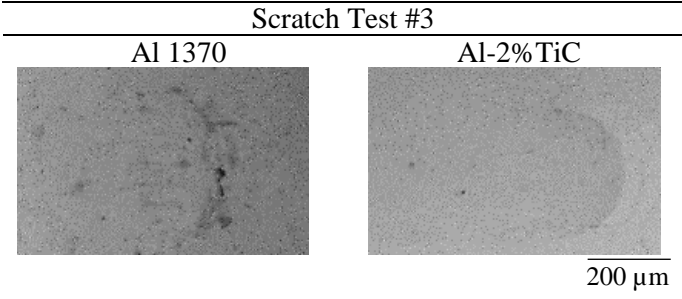
Figure 5.21. Adhesion mechanisms resulting on WC/Co ball surface after lubricated sliding contact

Lubrication significantly reduces the amount of aluminum adhesion especially in the presence of TiC due to its hardening effect. Consequently, lubrication inhibits the adhesion and COF is improved (Figure 5.16).

It can be observed that the scratch track profiles on both wires turn uniform, with few ribs along the track. Moreover, in the presence of TiC particles, the initial apparition of the groove is delayed until the last pass because of the hardening effect. Then, as lubrication reduces aluminum adhesion mechanisms, the appearance of grooves decreases drastically, and a good wire surface quality is obtained.

Scratch Test #1	Scratch Test #2	Scratch Test #3
	Al 1370	

50 µm

300 µm

| | Al-2%TiC | |

50 µm

300 µm
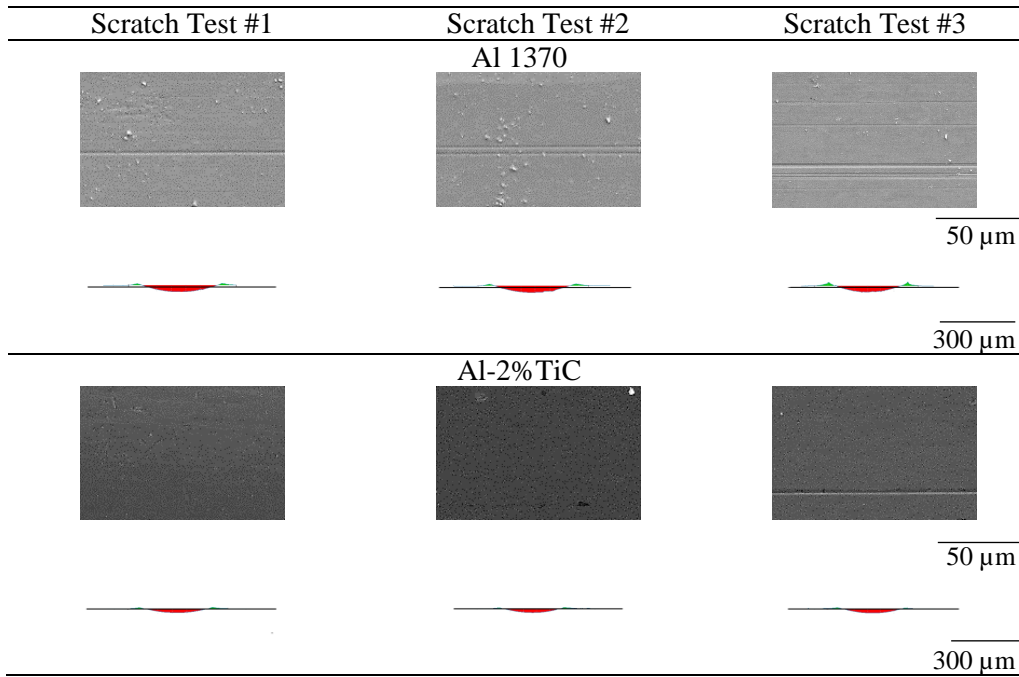
Figure 5.22. Wire track (longitudinal view and middle section profile in a range of ± 6 µm) after lubricated sliding contact

To quantify the amount of aluminum adhesion on WC/Co ball surface, the specific adhesive wear rate (K) was computed after each scratch test (Figure 5.23). It is worth to mention that adhesion values in lubricated condition were negligible; therefore, in this case, it has not been possible to compute K.
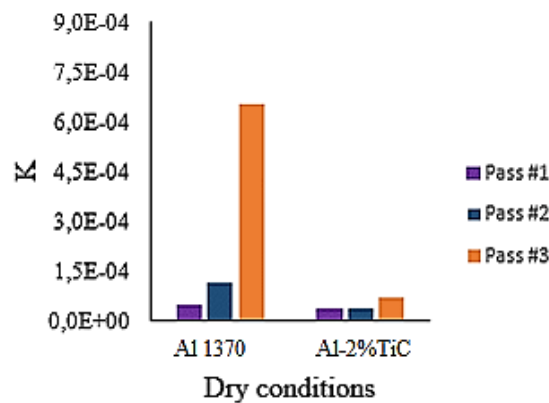
Figure 5.23. Specific adhesive wear rate K on ball surface in dry conditions for Al 1370 and Al-2%TiC wires (K values were negligible under lubricated conditions)

Figure 5.23 shows that, K increases progressively along the scratch test for Al 1370, entailing a significant increase of COF. On the contrary for Al-2%TiC wire, K increases slightly at the third scratch but not enough to increase COF. Then, COF results (Figure 5.16) and the identified wear damage mechanism, aluminum adhesion (Figure 5.17) are in agreement with K values (Figure 5.23).

93

5.2.2. Influence of DLC coatings in friction coefficient and wear mechanisms between Al 1370 and Al-2%TiC wires and WC/Co

The effect of DLC coatings in friction was evaluated by scratch test as described in section 3.2.4. In this study, WC/Co balls coated with an (a-C:H)/Cr and (a-C:H)/CrN DLC coatings were investigated. Table 5.5 summarizes the hardness and roughness of the analyzed coatings in comparison with the uncoated WC/Co ball. .

Table 5.5. Hardness and surface roughness of the analyzed coatings
(The uncoated WC/Co ball surface roughness has been added as a comparison)

Coating	H [GPa]	Ra [µm]
(a-C:H)/Cr	24.5 ± 2.0	0.024 ± 0.013
(a-C:H)/CrN	23.5 ± 1.2	0.031 ± 0.005
Uncoated	20.3 ± 0.6	0.023 ± 0.003

The coated balls were drawn over the polished surface of a 1.8 mm Al 1370 and Al-2%TiC wires. Three consecutive passes (unidirectional) were accomplished in order to correlate aluminum adhesion to the stated DLC coatings with the COF. Figure 5.24 shows the obtained results for each of the analyzed DLC coatings in dry and lubricated conditions.
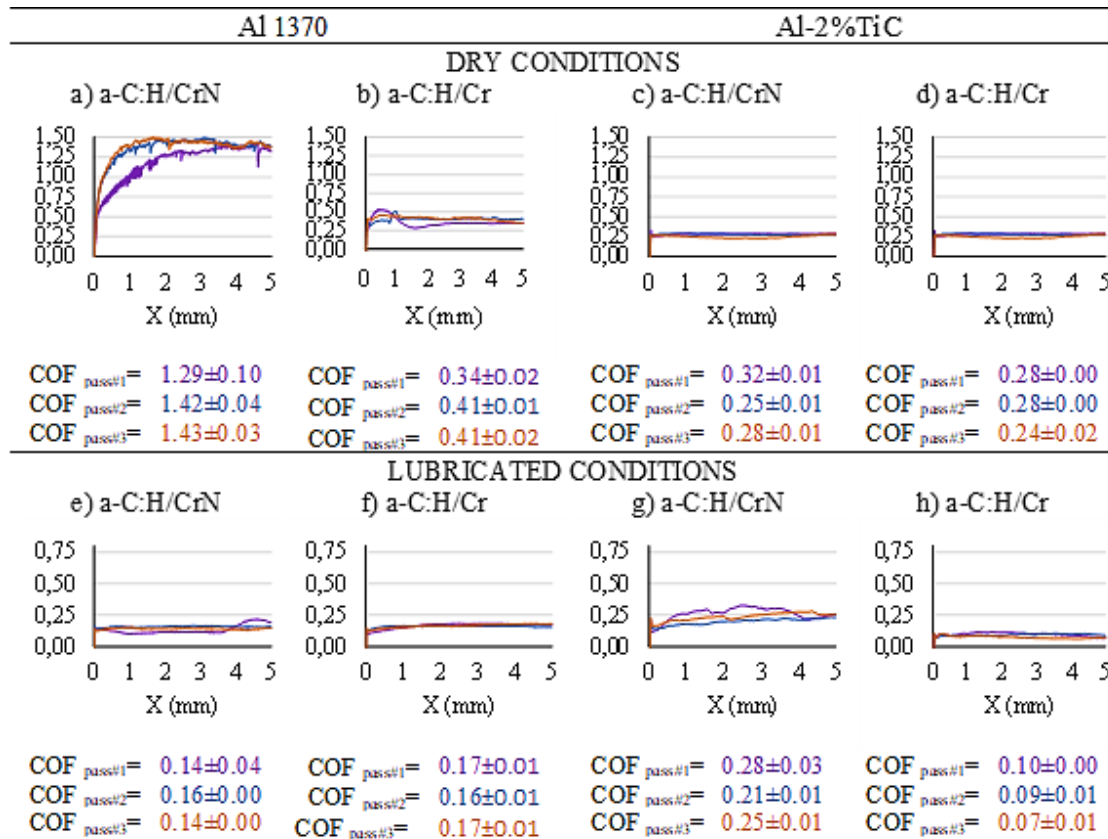
Figure 5. 24. COF for DLC coatings interaction with Al 1370 wire and Al-2% TiC wire in dry conditions (a), (b) and (c), (d), respectively, and in lubricated conditions (e), (f) and (g), (h) respectively (COF mean values were obtained when the steady state is achieved, neglecting the running-in period)

Figure 5.24 shows that the best tribological performance is achieved when the a-C:H/Cr DLC coating is deposited over a WC/Co ball. COF is reduced significantly in comparison with the a-C:H/CrN DLC coating. It is main due to DLC coating surface roughness (Table 5.5). A higher roughness entails and increase of punctual contact points acting as a preferential spots to material transfer, according to Figure 5.25. This triggers localized high contact pressures leading to inordinate adhesion rates, further aided by hard (WC/Co) versus soft (aluminum) sliding contact.
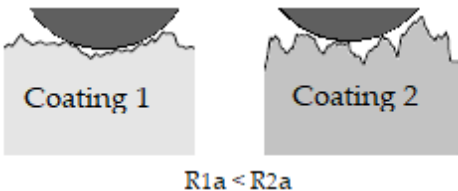
Figure 5. 25. Coating surface roughness – ball contact

In order to correlate this behavior with the adhesion wear damage on the coated ball surface, Figure 5.26 and Figure 5.27 show the amount of aluminum adhered over the a-C:H/CrN and a-C:H/Cr coatings under dry and lubricated conditions, respectively.

a-C:H/CrN		a-C:H/Cr	
Al 1370	Al-2%TiC	Al 1370	Al-2%TiC
Scratch Test #1			
Scratch Test #2			
Scratch Test #3			
			200 µm
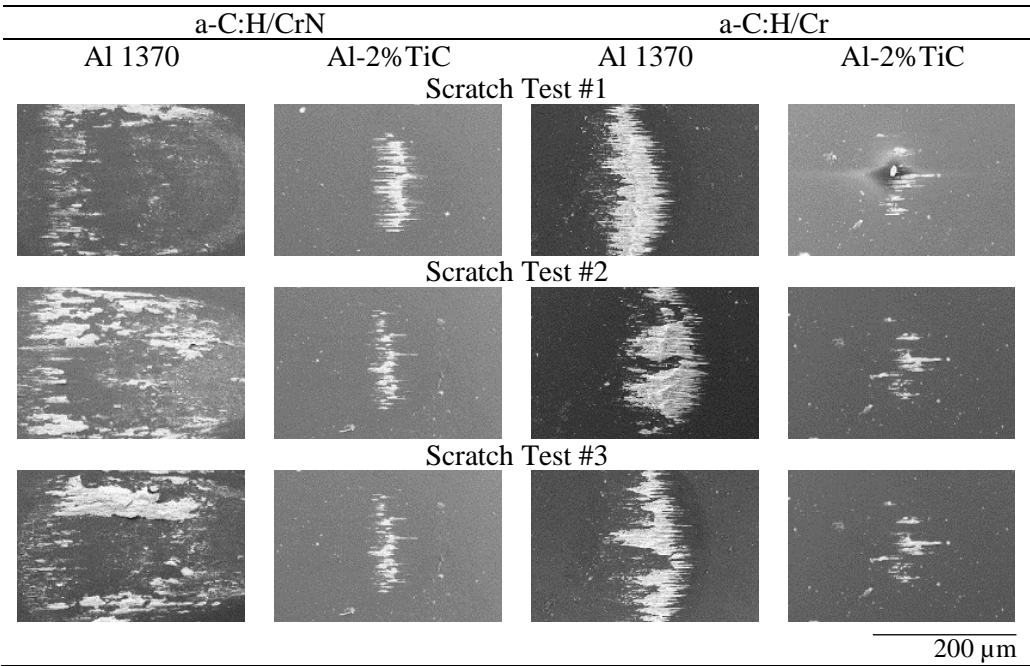
Figure 5. 26. Adhesion mechanisms evolution with DLC coatings on WC/Co ball in dry conditions

It can be observed that under dry conditions, adhesion increases in the case of Al 1370, in agreement with the COF values reported in Figure 5.23. On the other hand, in the presence of TiC particles, both DLC coatings exhibits similar COF as well as similar adhesion volumes.

	a-C:H/CrN		a-C:H/Cr	
	Al 1370	Al-2%TiC	Al 1370	Al-2%TiC

200 µm
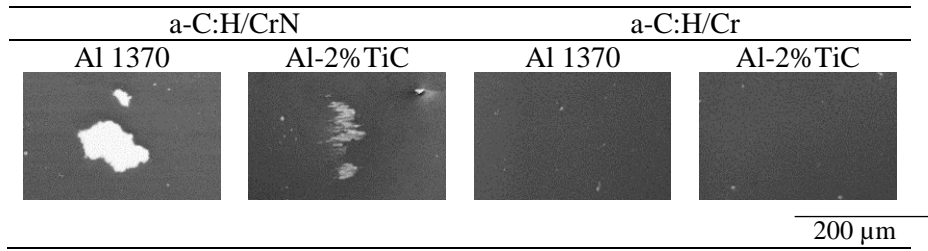
Figure 5.27. Adhesion mechanisms evolution with DLC coatings on WC/Co ball in lubricated conditions

From Figure 5.27, it can be appreciated that under lubricated conditions adhesion is drastically reduced an even eliminated when the a-c:H/Cr coating is used. Then, COFs and adhesion are higher for the a-C:H/CrN coating. In addition, for the a-C:H/Cr DLC coating, COF values decrease in the presence of TiCs due to the hardening effect that it induces on the wire. Figure 5.28 and Figure 5.29 show the final scratch tracks over the wires during the sliding for a-C:H/CrN coating and a-C:H/Cr coating under dry and lubricated conditions, respectively.

	a-C:H/CrN		a-C:H/Cr	
	Al 1370	Al-2%TiC	Al 1370	Al-2%TiC

Scratch Test #1

50 µm

300 µm

Scratch Test #2

50 µm

300 µm

Scratch Test #3

50 µm

300 µm
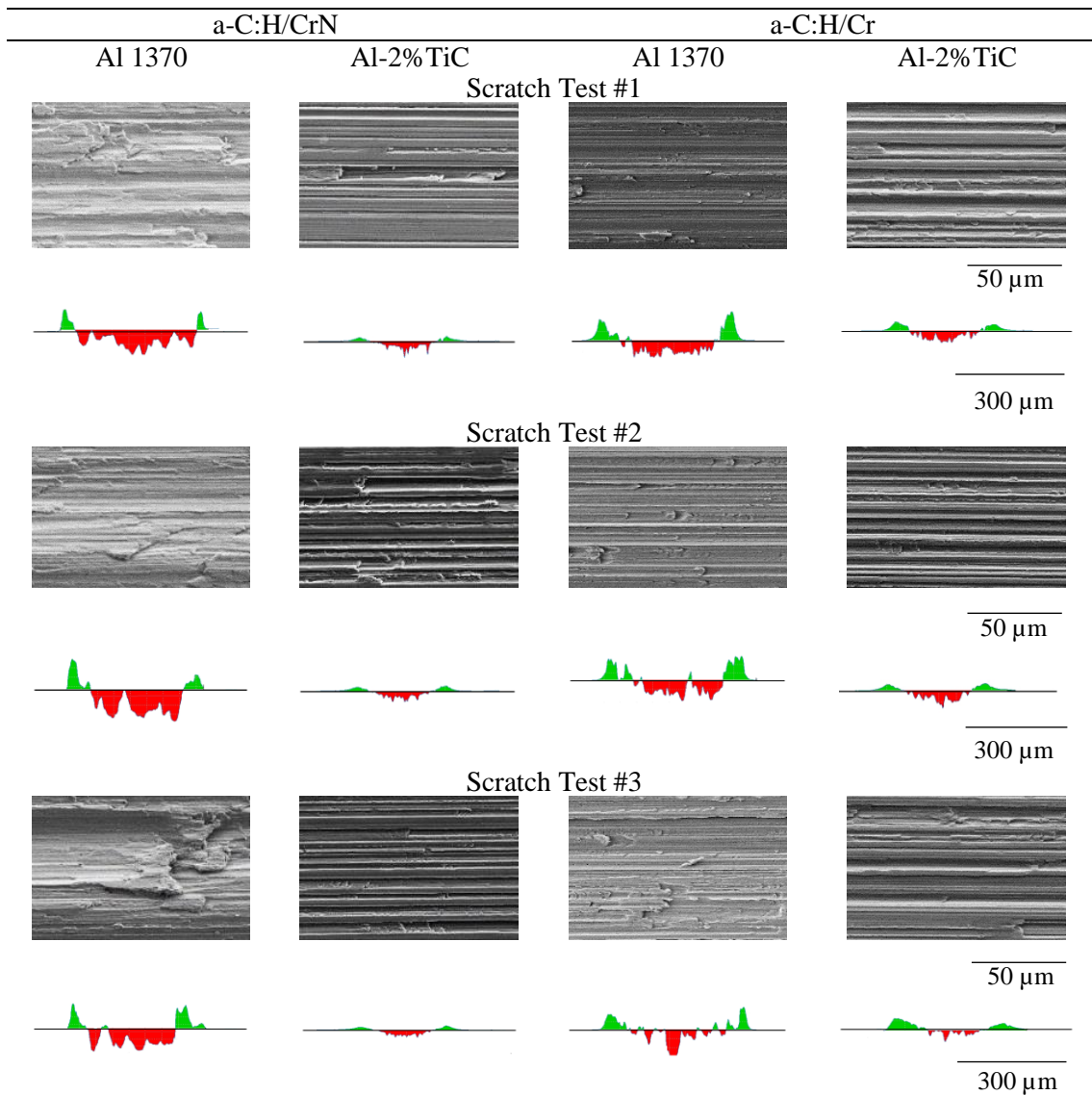
Figure 5. 28. Wire track (longitudinal and middle section profile) in a range of ± 6 µm in dry and coated conditions

It can be noticed that for both DLC coatings, a progressive increase of the pile-up is observed on the Al 1370 scratch track in comparison with the uncoated WC/Co ball. This effect is mainly due to presence of blunt non-abrasive and sharp abrasive grits released as third-body, as Figure 5.29 shows.
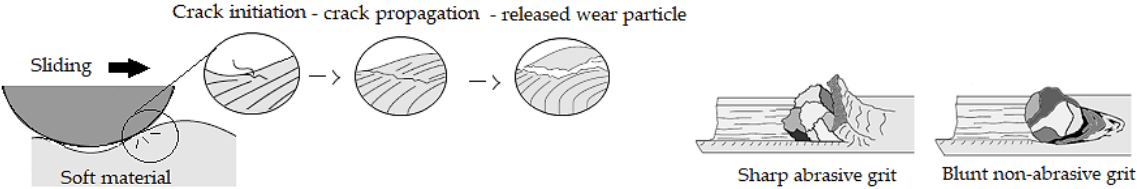
Figure 5.29. Abrasive particles released from the adhesion mechanism [48]

Depending on the wire hardness and the coating roughness, large material overlaps whereby the friction values are triggered (Figure 5.24). For Al – 2%TiC, the irregularities are persistent but shallower than on Al 1370 wire. Nevertheless, these skewed profiles have to be reduced as far as possible, entailing the use of lubrication, as shown in Figure 5.30.
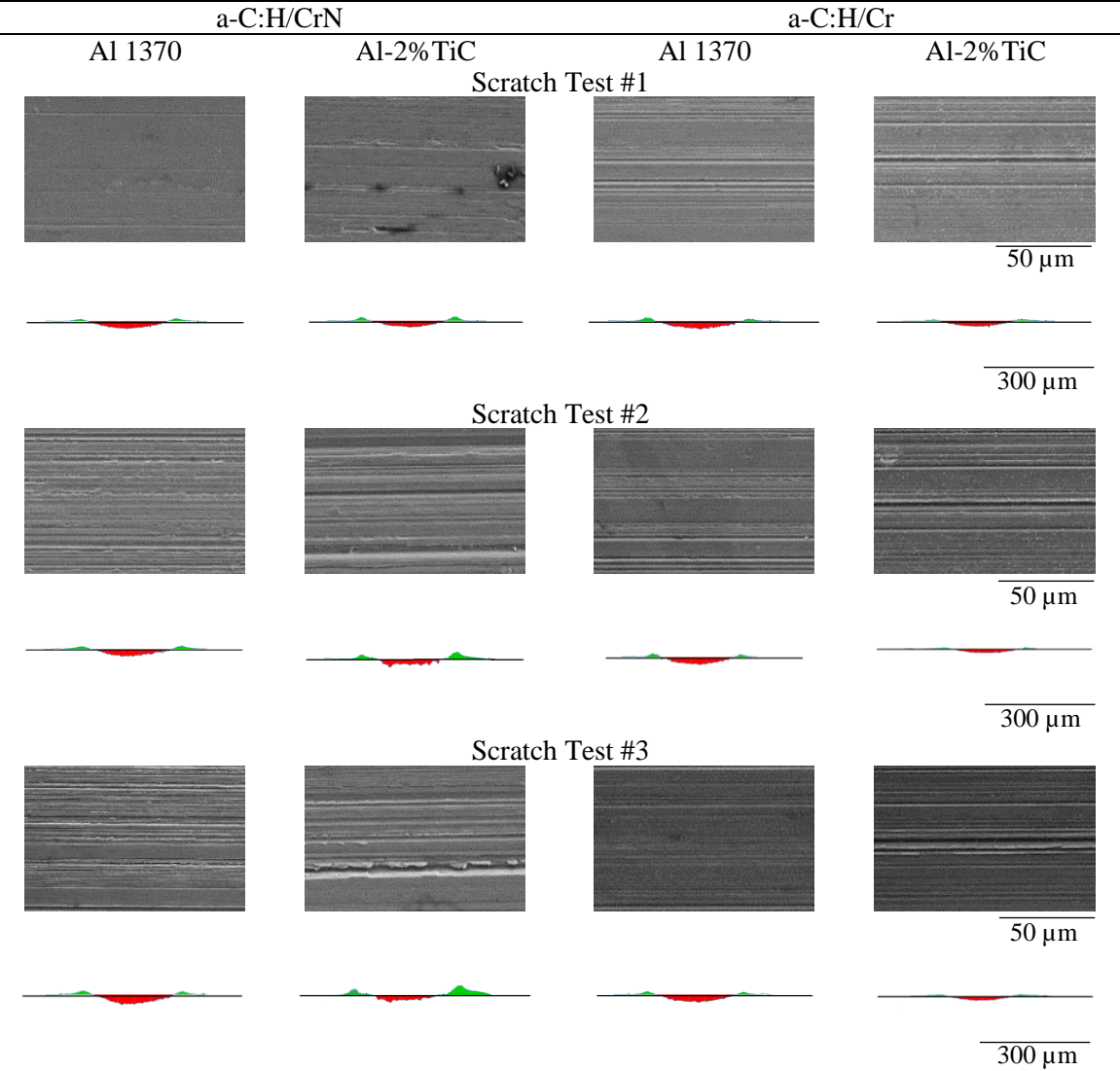
Figure 5.30. Wire track (longitudinal and middle section profile) in a range of ± 6 μm in lubricated and coated conditions

Figure 5.30 shows as these interactions yield in an irregular but minor depth track cross-section profile (red) with smaller volumetric aspect of the overlaps (green) than in the case of dry conditions. When the a-C:H/CrN coating was drawn on the Al 1370 lubricated wire, the track section profile acquired a rounded shape. For a-C:H/Cr coating, improved rounded scratch profiles, shallower than those obtained for Al 1370 are observed. In this case COF values reach similar values that in uncoated lubricated conditions (Figure 5.16 (d) and Figure 5.16 (h)). However, unlike to that configuration, the stretch marks persist (Figure 5.30), even though the adhesion has been suppressed (Figure 5.27). This means that the roughness still performs a critical factor on the wire finish.

These observations can be corroborated by Figure 5.31, which shows the aluminum adhering volume to the WC/Co ball coated surfaces by means of the specific adhesive wear rate (K).
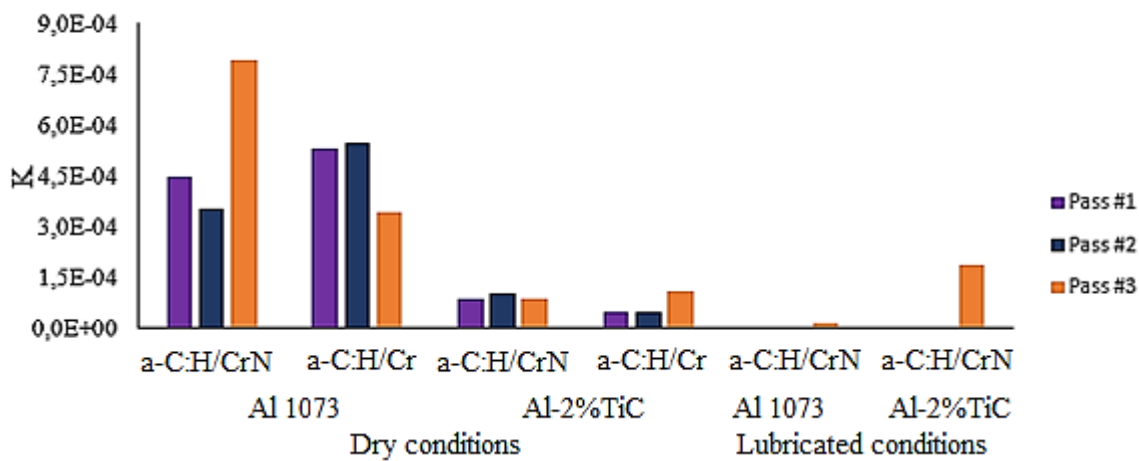
Figure 5.31. Specific adhesive wear rate K on coated ball surface in dry conditions for Al 1370 and Al-2% TiC wire surfaces (negligible K values were acquired with a-C:H/Cr coating)

From Figure 5.31, it can be observed that reported COF values are in agreement with K, since as K increase the COF also increase, meaning that adhesion is detrimental in terms of friction behaviour. This observed aluminum adhesion, as seen with the uncoated WC/Co ball condition, have a direct influence over the final surface quality of the WAAM wire. For Al-2%TiC in dry conditions, it can be appreciated that TiC nanoparticles mitigate the adhesion again while, in agreement with COF values (Figures 5.24 (c) and 5.24 (d)), the wear rates are similar for both DLC coatings (Figure 5.30). In lubricated conditions, for a-C:H/Cr DLC coating, adhesion values were negligible for both aluminum alloys. In the case of a-C:H/CrN DLC coating, K increases in the presence of TiC nanoparticles, reaching higher values than in dry conditions. Therefore, lubrication advantages are suppressed when a-C:H/CrN DLC coating is drawn over Al-2%TiC lubricated wires.

5.2.3. Wear micro-mechanisms

According to the results described in sections 5.2.1 and 5.2.2, aluminum adhesion has a direct influence on both friction and . abrasive wear. In this section the wear micro-mechanisms that leads to the observed results are discussed.
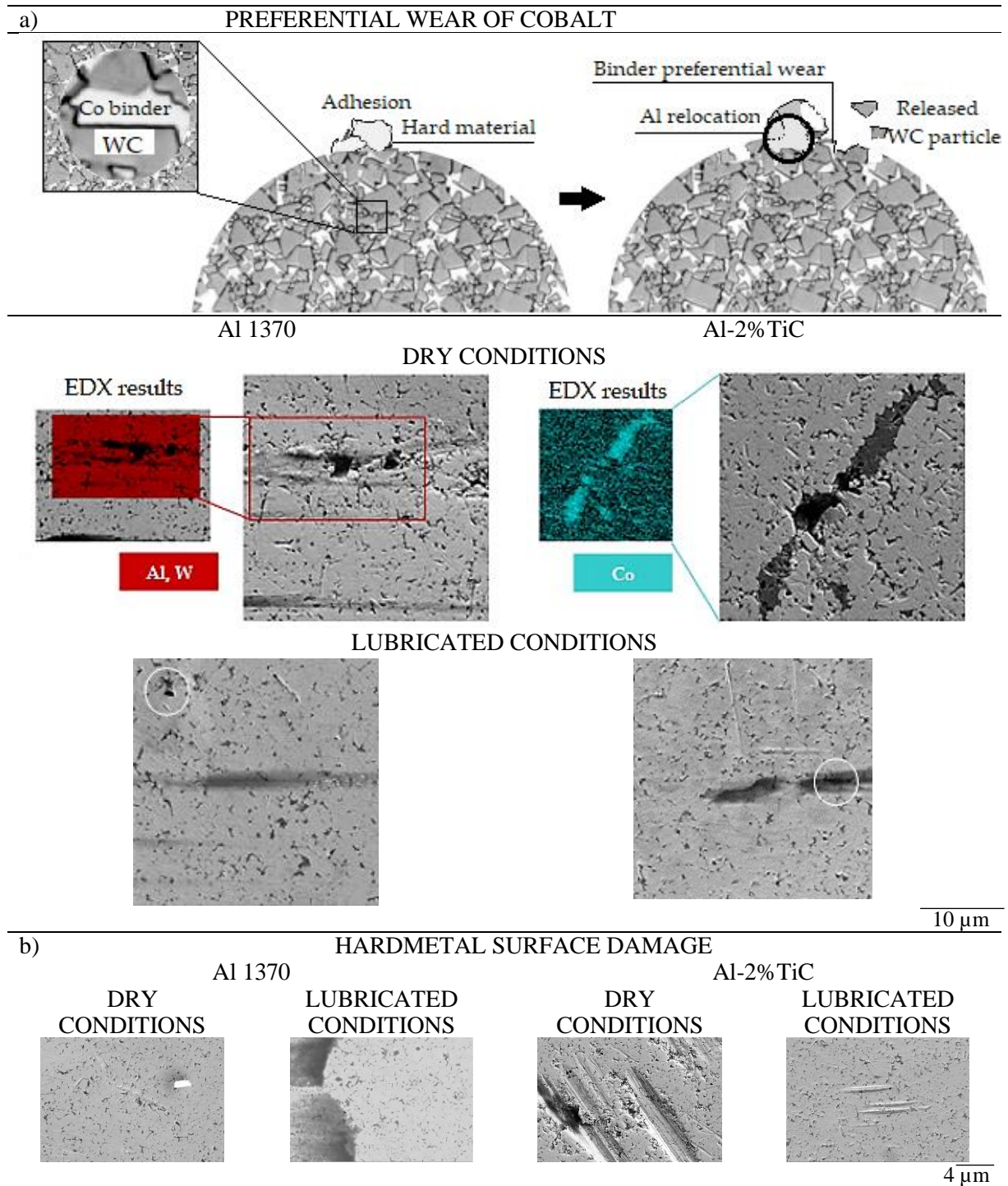
Figure 5.32. Wear micro-mechanisms on Wc/Co ball surface

Figure 5.32 (a) shows how WC particles spelled out in WC/Co surface in dry conditions is intensified in the periphery of the contact zone as the experiment progresses. Due to the

premature wear of the WC/Co softest component: cobalt, WC particles spall out, then the generated empty spot, acts as a preferential location for aluminum adhesion. In that manner, Figure 5.32 (a) exemplifies the TiC nanoparticles effect in this wear micro-mechanism. Their presence facilitates the abrupt separation of hardmetal carbides while reducing the aluminum encroachment, this is because of the TiC nanoparticle hardening effect. In any case, this harsh WC particles spall out generates an additional abrasive wear mechanism: third-body type. These observations are in accordance with the marked difference between the hardmetal damage caused during the scratch tests on Al 1370 wire and the one caused on Al-2%TiC wire. This condition improves once again with lubrication, where adhesion and the presence of scratches are almost negligible.

Figure 5.33 summarizes the wear micro-mechanisms observed during the sliding interaction of the aluminum wires and the DLC coated WC/Co balls.
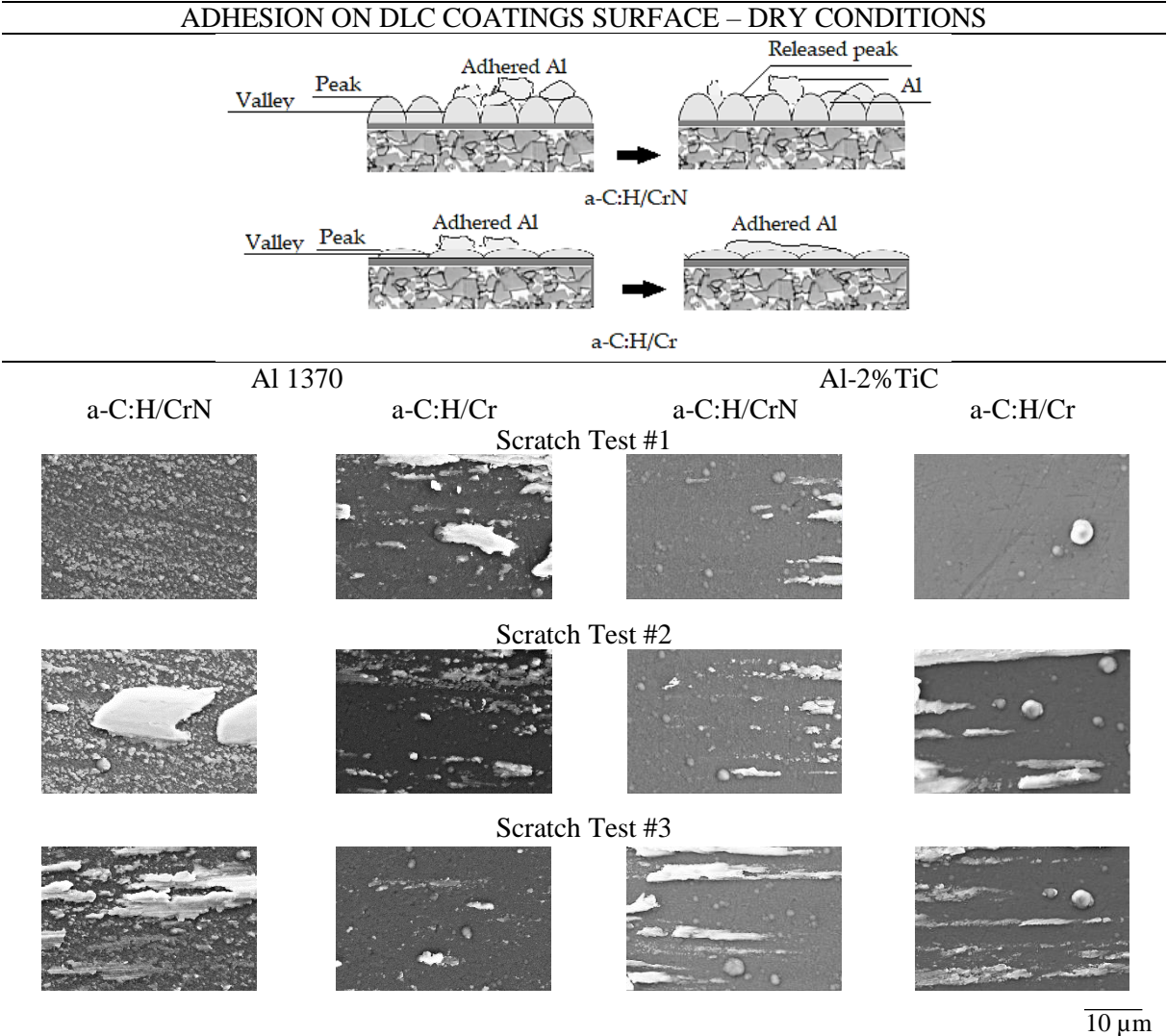
Figure 5. 33. Micro-wear mechanisms on coatings surface under dry conditons

Figure 5.33 demonstrates the coating roughness effect on the aluminum adhesion on its surface. Higher the roughness (a-C:H/CrN), higher the adhesion. Aluminum is first adhered to the peaks of the coating; this adhesion is increased along the scratch tests until its detached due to the shear stresses experienced during the scratch. On the other hand, when the roughness of the coating is decreased (a-C:H/Cr), aluminum adhesion is decreased, however the coating peaks also act as a preferential spot to adhesion. In any case, the detachments of the aluminum adhered on the ball, constitute a third-body element at the contact surface, affecting the final wire surface quality as well. In that sense Figure 5.34 exhibits the micro-mechanisms found on the wire track under the best interaction performances.

CHEVRON CRACKING			
UNCOATED AND LUBRICATED CONDITIONS		a-C:H/Cr COATING AND LUBRICATED CONDITIONS	
Al 1370	Al-2%TiC	Al 1370	Al-2%TiC

4 µm
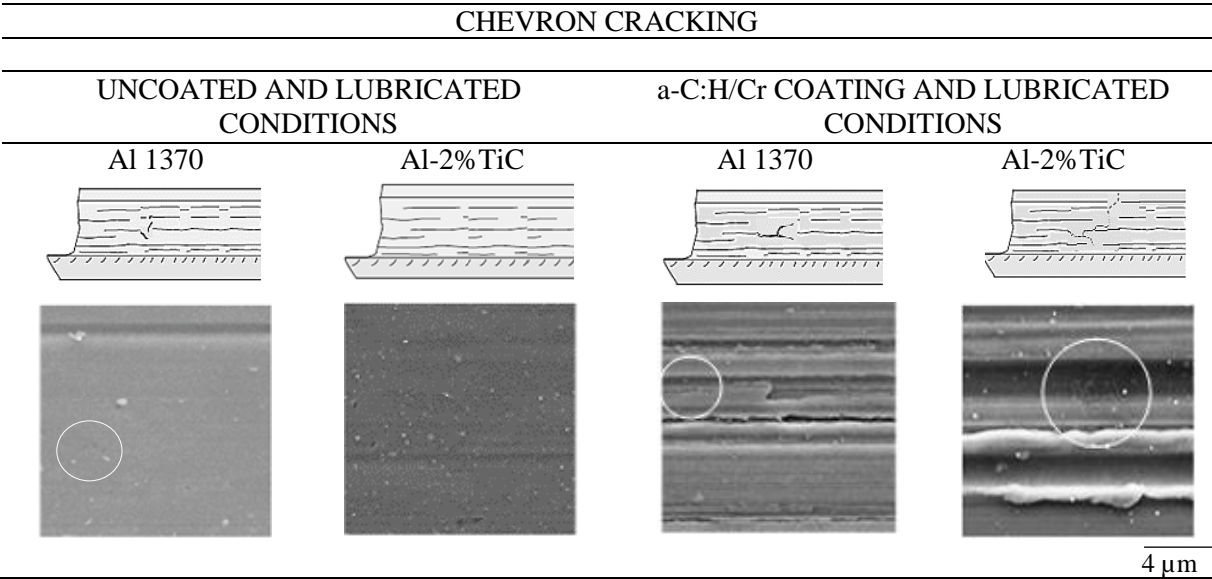
Figure 5.34. Wear micro- mechanisms on the wire track after scratch tests #3 in uncoated and with the optimal DLC coating in lubricated conditions

Concerning the micro-defects generation on the wire surface in lubricated conditions, Figure 5.34 shows that the interaction of the uncoated ball and Al-2%TiC, not exhibit chevron cracking on the scratch path. However, longitudinal scratches with subtle presence of chevron cracking are evident on the Al 1370 track. On the other hand, the a-C:H/Cr DLC coating exhibits chevron cracking on both wires surface (Al 1370 and Al-2%TiC), with pronounced longitudinal scratches (more severe than in uncoated conditions). In this manner, it is evidenced that, despite the fact that coatings suppress preferential wear of Co and the WC spall out, wire striations are maintained according to the coating roughness, leading to a lower chevron cracking manifestation.

5.3. Discussion

The first step in the pursuit of potential solutions to obtain an improved hardened aluminum wire that reduces porosity in the final 3D printed components [139] while satisfying the requirements of WAAM surface conditions: homogeneous diameter, surface integrity and low sliding friction [95,143], is to achieve an effective diameter MMCs wire reduction during its pass through the hardmetal die [2,95]. This challenge is achieved by the prior characterization and subsequent reduction of the friction and wear mechanisms resulting from the sliding contact between the WC/Co and the Al 1370 and Al-2%TiC wires. In that sense, friction reduction, demonstrated in section 5.2.1, was enabled by the action of TiC nanoparticles in the aluminum matrix, as cited [108]. The quoted results show that TiC particles not only act as hardening agents (Table 3.5), but also constitute elements that enhance the interaction, minimizing, and stabilizing friction while mitigating the main wear mechanism: adhesion [2,21,95], even under lean lubrication. However, mitigation is not suppression (Figure 5.17), so under these conditions, the remaining adhered aluminum volumes in the WC/Co surface (Figure 5.17, Figure 5.18) [23,82,102] later constitute the abrasive two-body wear mechanism [1,145,146] for the drawn wire. According to [95], the two-body mechanism is able to micro-cut the emerging feedstock, leading to the eventual ductile microfractures formation known as chevron cracking. Thereby, as Figure 5.19 shows, despite the hardness increase that TiC particles impart to the aluminum wire, the early micro-cut effects as longitudinal grooves, material clumps and chipping, as well as the derived damage: chevron cracking (Figure 5.34) are still observed, especially on the Al 1370 surface [32,94]. Moreover, the adhesion consequences are not limited to the feedstock. Adhesion wear is intensified as result of preferential wear of Co [101,153] was evidenced (Figure 5.32). The existence of cavities left by the WC particles of the WC/Co ball, spall out during the scratch performance on aluminum wires (promoted by the TiCs as a second feedstock phase [146,147]), act as a preferential spots to aluminum adhesion.). Then, these WC particles roll and slide into clusters at the interface deriving in the third-body abrasive wear mechanism [102] and adversely affecting both the WC/Co ball surface and the wire surface quality. The ball damage of this third-body mechanism (previously reported by [96]) was appreciated in Figure 5.34 like deep scratches marks. Finally, with the free WC hard particles insertion into the contact, the aluminum from the Al 1370 wire takes place in zones where cobalt has been worn. It is noticeable how in the case of Al-2%TiC, an inhibitory role to this aluminum reallocation is exerted by the TiCs. Thus, under the characterization of these

precedents, lubrication is proposed as a solution to ameliorate these deleterious conditions, as the next step in the pursuit of this optimization.

As quoted [2,148], a suitable lubrication reduces adhesion, friction, and tool wear while improving wire surface. In this regard, according with section 5.2.1. (Figure 5.16 (c) and 5.16 (d)), lubricant allows a low-wear friction condition, whereby, under its effect, adhesion disappears (Figure 5.23) in contrast to what is affirmed by [103]. Therefore, since friction is no longer influenced by adhesion, the difference between the COFs obtained on Al 1370 and Al-2%TiC wires under these conditions, is established by the TiC particles. These particles constitute the transfer film between the lubricant and the surfaces into contact. Then, TiCs and lubricant work together. Only under the lubricant influence, the scratch track profiles become uniform, with little presence of ribs along the section track. However, when the hardening effect of TiCs in integrated into contact, the longitudinal groove initial apparition (resulting from the WC detachment) is delayed. Nonetheless, wear signs on the WC/Co surface are still observed (Figure 5.32). Thus, it is evident that the lubricating layer in complex with TiCs improve the wire finish but does not itself suppress the undesirable damage on the WC/Co surface. If this damage is not removed, it will later harm the wire integrity. So, another proposal arises: the use of a-C:H DLC coatings.

According to [103,107,111], tool wear has been significantly reduced by using coatings on the tool surface. In that sense, Figure 5.26 and Figure 5.27, allow to validate that inference, showing that DLC coatings establish a shield against Co wear in hardmetal, as quoted [107]. It has also been stated that coating films provides lower COF values [103,111,114]. Nevertheless, is not the case in non-lubricated conditions or in lubricated conditions under the effect of certain factors. Thus, in the lack of lubrication, the a-C:H/CrN and a-C:H/Cr coatings exhibit higher COF values (Figures 5.24 (a) -5.24 (d)) with respect to the uncoated conditions (Figures 5.16 (a) and 5.16 (b)), showing a relevant roughness influence in friction and in the wear mechanisms generation. Furthermore, it is worth noting that despite the different Ra values that both coatings display, the tribological response (COF and K values) of Al-2%TiC is similar for both (Figure 5.24 (c) and 5.24 (d) and Figure 5.31), contrary to what happens in Al 1370 (Figure 5.24 (a), 5.24 (b) and Figure 5.31), that presents high adhesion rates. Hence, the hardening caused by the TiC particles reduces aluminum adhesion tendency and preserves the friction under certain roughness ranges. Moreover, as an effect of the reduced adhesion, the hardened aluminum detachment from the coatings surface is lower (Figure 5.31), involving minor third-body wear

effect. This statement is corroborated by the Al-2%TiC track section profiles that show irregular, but shallower ribs than in the case of Al 1370 (Figure 5.28). To solve this issue, lubrication is proposed again.

Scratch track profile homogeneity is achieved under the effects of lubrication, but it is not the only conditioning factor. Here, roughness and chemical interaction between the wire and the coating also play important roles. On one hand, the roughness conditions of the surfaces in contact act like lubricant reservoirs [2], influencing the contact area and local stresses [105]. Then, the films roughness must be friendly with the lubricant [103]. On hereto, evaluating the a-C:H/Cr behavior (Figures 5.24 (f) and 5.24 (h)), for Al-2%TiC, the friction values (with greater uncertainty) decrease until reaching the values obtained in un-coated conditions (Figure 5.16 (d)). This event does not occur in the case of Al 1370. Therefore, TiCs reinforcement does again promote a proper interaction between the wire, the roughness and nature of the coating and the lubricant. Analogous considerations can be established when analyzing the tracks. Uniform and shallow depth profiles, similar to those obtained in the Al-2%TiC and its interaction in lubricated conditions with the uncoated ball are seen (Figure 5.22 and Figure 5.30). However, for both cases the stretch marks persist, for the former due to the coating roughness (with a nuanced presence of chevron cracking) and for the latter due to the chipping of WC particles from the WC/Co surface.

In this manner, this study shows that in order to improve wire surface integrity during the sliding contact, lubrication plays an important role. Moreover, the use of DLC coatings with low roughness in the WC/Co surface is also a good option to decrease defects on the WAAM wire. However, improvements still remain to be done. When an uncoated hardmetal is used, a continuous loss of surface material (matrix weakening [95,102]) is observed, however with a coated surface it can be still detected chevron cracking formation in the wire surface [23,103]) which results not only from the adhesion as quoted [95,102], but also from the roughness of the coating.

5.4. Partial Conclusions

With the development of new and improved materials, the manufacturing processes demand adjustments that allow their maximum profitability. In the case of reinforced aluminum WAAM feedstock (Al-2%TiC), these demands involve high surface quality, in order to reduce porosity in the final 3D printed component. This aim is attained through the effective wire drawing process performance. For this purpose, the process interactions that ensue must be optimized.

This work focuses on the readjustment of the fundamental interaction among the constituent elements: hardmetal - lubrication - feedstock. Through the tribological study of the sliding contact, the influence of wear mechanisms on the wire dimensional accuracy, its surface finish, and its improvements has been demonstrated, leading to the following conclusions:

- Adhesion as the first weakening factor of both WC/Co and wire integrity, has been evidenced and mitigated by the presence of TiC nanoparticles in the Al base alloy. Furthermore, as a subsequent result of this mitigation, friction was also reduced. It demonstrates that, besides to enhance the anti-cracking properties after WAAM, TiCs improve the wire previous processability. However, despite the friction reduction, there are mechanisms that have not been suppressed but rather attenuated. These are two-body (resulting from the aluminum volumes adhering to the WC/Co surface) and third-body abrasion damage (surface wire and WC/Co damage) generated by the WC particles spelled out, resulting from the preferential Co worn, that persist even in lubricated conditions.

- Lubrication suppress adhesion while reducing friction and WC/Co wear, enhancing the Al-2%TiC wire surface quality. Here, TiC particles act like a transfer film among the lubricant and the surfaces into contact. Uniform wire surface resulting from the scratch tests, with delayed longitudinal grooves were appreciated. Nevertheless, deep scratches as the third-body abrasive damage consequences on the hardmetal surface was still observed.

- The use of DLC coatings was proposed as an effective strategy to reduce wear damage and enhance wire surface quality. DLC coatings with Cr interlayer are a convenient solution to the problems of Al sticking and selective binder wear, as it showed tribological affinity with the TiC particles of the reinforced wire and the lubricant, extending the tool service life. However, its high roughness enhanced aluminum adhesion on the WC/Co surface favoring posterior crow's feet formation, that later will constitute encapsulation sites for hydrogen, lubricant, and impurities, giving porous AM parts. Therefore, the use of soft roughness a-C:H/Cr DLC coating, with less roughness, deposited on the tool surface offers a suitable solution.

- The future approach of this a-C:H/Cr DLC coating with water-based emulsions or with solid components that reduce the oil-based lubricant consumption is proposed. Obtaining this Cr interlayer coating with enhanced roughness surface is another

emerging challenge that will mark the process improvement in terms of both tool and the wire surface integrity.

Chapter 6

Conclusions and future works

6.1. General conclusions

In this dissertation, the study, characterization and optimization of the tool-part tribological interaction for continuous deformation processes have been achieved. The proposed experimental methods to compute friction as well as their wear consequences in the surface integrity of the interacting components allow the successful conceptualization of ball burnishing and wire drawing from a tribological perspective. In that sense, optimal operational parameters and strategies have been established for the tribological response of stainless-steels and aluminum alloys to the cold plastic deformation performed by hardmetal tools. Besides, this research is established as an input for future integral simulations setup, that consider friction and its effects as primary constituents for accurate wear and surface integrity predictions. Therefore, the main objective of this dissertation has been achieved, optimizing both continuous deformation processes thorough the characterization of the tool-part tribological interaction to guarantee the surface integrity of the interacting parts. Nevertheless, the proposed solutions must be industrially tested for their entire implementation. Even though these inferences are thoroughly explained in the previous chapters, the general conclusions of the present dissertation are cited below:

Ball burnishing process

- In order to improve the surface integrity of machined components in ball-burnishing process, the tribo-interaction between the hardmetal tool and the microstructure of the surface piece is the primary aspect to be addressed. This interaction is measurable by means of COF. This parameter sets the final conditions of the burnished components. Roughness, texture, tolerances, residual stresses, and the directional and residual anisotropy are depending on friction.
- The developed experimental methodology to compute the friction coefficient according to the burnishing parameters, provides factual inputs for both the existent numerical methodologies and the future ball-burnishing crystalline plasticity numerical models.

Regarding the numerical methodologies, its adaptability has been validated adjusting a previous integral simulation to other material conditions and feeding it with the presented experimental values. The outstanding results in terms of the final surface integrity highlight the relevance of including friction as a fundamental parameter in the numerical process conceptualization. Therefore, a novel and economical tool to establish the most efficient path for the ball burnishing process was proved.

- This research also demonstrates that adapting the operational parameters, in this case the force, to the treated microstructure, the ball burnishing process is able to enhance the surface integrity of steels not yet studied (such as the UNS S46500 stainless steel). The microstructural deformation mechanisms at the local level results on unique tribo-contacts, entailing different induced states of surface roughness and residual stress profiles. Thus, it has been proved that friction is a key operational parameter in ball burnishing, controlling the subsurface final condition state.

Wire drawing process

- The main damage tool mechanisms in industrial wire drawing have been established. The surface integrity of the manufactured die has a direct effect on both their service life and the surface integrity of the produced wire. Although, adhesion and abrasion has been identified as the main wear mechanisms affecting the surface integrity of both the die and the surface quality of the wire.

- The tribological characterization of reinforced aluminum WAAM feedstock and hardmetal interaction allows to establish a reliable path for the wire drawing execution. Based on the proper materials and surfaces conditions, by means of lubrication and DLC coatings strategies implementation, a high-quality wire surface was obtained. Taking into account wear mechanisms and micro-mechanisms effect on COF, wire surfaces with dimensional accuracy and minor flaws can be produced.

- In the quest to increase drawing tool service life and wire surface quality, adhesion is the first wear mechanism to be overcome during the process. In that sense, the presence of TiC nanoparticles in the Al base alloy and the use of lubrication strategies, mitigated its effects. The use of hardmetal as a die material, can increase third-body abrasion damage due to a preferential Co wear that leads to a WC particle spall out. The use of coated dies strategies, such low friction DLC coatings, eliminates third-body abrasion.

- The roughness of DLC coatings plays a relevant role in the sliding tribo-interaction with Al based alloy wires. High roughness enhances adhesion and can induce chevron cracking or crow's feet formation on the wire surface, sometimes suppressing the lubricant benefits.

6.2. Future works

In order to contribute to the guidelines for future research derived from this thesis, some proposals are mentioned as follow:

- The developed experimental methodology applied to the numerical configurations must be evaluated in an industrial application, where several metal surfaces are improved by means of ball burnishing procedure. In that sense, both stainless-steel microstructural responses to the plastic deformation induced by the burnishing tool, also shall serve as the basis to develop ball-burnishing crystalline plasticity numerical models.

- The surface and sub-subsurface microstructural response, in terms of microhardness and induced texture on the stainless steels after burnishing execution, as well as the friction effects at the sub-surface level have to be evaluated in detail in order to increase the required anisotropy, according to the burnished components application. The understanding of the deformation mechanisms in a nano-scale can reveal new enhancements in the process implementation.

- The use of a-C:H/Cr DLC coating as a protective layer of hardmetal tool during reinforced wire drawing performance must be evaluated in situ, as long as a smooth surface finish has been obtained. In this regard, new proposals for low friction and low roughness coatings must be developed.

- Novel approaches in water-based emulsions or solid lubricants to diminish the oil-based lubricant consumption during the wire drawing process should be arise. These approaches cannot detract the compatibility with the coating and the reinforcement nanoparticles in the aluminum alloys.

Bibliography

1. Callister, W.D.; Rethwisch, D.G. Materials Science and Engineering, 9th ed.; Wiley: Hoboken, NJ, USA, 2014. Materials 2022, 15, 8829 12 of 12.

2. Groover, M. Fundementals of Modern Manufacturing Materials, Processes and Systems 2010, (John Wiley & Sons).

3. Saffioti, M.; Sanguedolce, M.; Rotella g. and Filice, L. Effects of Burnishing Process on Tribological Surface Resistance of Additively Manufactured Steel. ESAFORM 2021 [Online], Online since 23 March 2021, connection on 03 March 2023. URL: https://popups.uliege.be/esaform21/index.php?id=1903

4. Jerez-Mesa, R. *Study and Characterization of Surface Integrity Modification after Ultrasonic Vibration-Assisted Ball Burnishing; Mechanics of materials* [physics.class-ph]; Université Paul Sabatier, Toulouse III: Toulouse, France, 2018.

5. Podgornik, J., Hogmark, B., Pezdirnik, S. Comparison between different test methods for evaluation of galling properties of surface engineered tool surfaces, *Wear*. 2004, 257, 7–8, 843-851.

6. ASTM G40: Standard Terminology Relating to Wear and Erosion. 2022.

7. Astakhov, V. Surface Integrity – Definition and Importance in Functional Performance, 2010.

8. Del Pozo, D.; De La Calle, L. N. L.; López, J. M. and Hernández, A. A. Prediction of press/die deformation for an accurate manufacturing of drawing dies. *Int. J. Adv. Manuf. Technol.* 2008, 37, 649–656

9. Griffiths, B. Manufacturing Surface Technology: Surface Integrity & Funtional Performance. Lodon: Penton Press, 2001.

10. Knoerr, M.; Lange, K. and Altan, T. Fatigue failure of cold forging tooling: Causes and possible solutions through fatigue analysis. *J. Mater. Process. Technol*. 1994, 46, 57–71.

11. ASM, "Volume 18: Friction, Lubrication and Wear Technology", vol. 18. 2005.

12. Raja, J.; Muralikrishnan, B.; Shengyu, F. Recent advances in separation of roughness, waviness and form. *Precision Engineering Journal of the International Societies for Precision Engineering and Nanotechnology*.2002, 26, 222–23

13. Foadian, F. P*recision Tube Production Influencing the Eccentricity, Residual Stresses and Texture Developments: Experiments and Multiscale Simulation*. Doctoral Thesis (Dissertation) Farzad Foadian from Tabriz / Iran, 2017.

14. Withers P. J. and Bhadeshia H. K. D. H. Residual stress. Part 1; Measurement techniques. Mater. Sci. Technol. 2001,17, 4, 355–365.

15. Javadi, Y.; Akhlaghi, M. and Najafabadi, M. A. Using finite element and ultrasonic method to evaluate welding longitudinal residual stress through the thickness in austenitic stainless steel plates. *Mater. Des*.2013, 45, 628–642.

16. Hauk V. and Behnken, H. Eds., Structural and residual stress analysis by nondestructive methods: Evaluation - application - assessment. Amsterdam: Elsevier, 2006.

17. Falk, B.; Engel, U. and Geiger, M. Estimation of tool life in bulk metal forming based on different failure concepts, *J. Mater. Process. Technol.* 1998, 80–81, 602–607.

18. Carlsson P. and Olsson, M. PVD coatings for sheet metal forming processes—a tribological evaluation. *Surf. Coatings Technol*. 2006, 200, 14–15, 4654–4663. doi: 10.1016/J.SURFCOAT.2004.10.127.

19. Holmberg, K. Coatings Tribology: Properties, Mechanisms, Techniques and Applications in Surface Engineering, 2nd Edition, 2009.

20. Saha, P. Aluminum Extrusion Technology. Ohio, ASM 2000.

21. ASM, Volume 14A: Metalworking: Bulk Forming, vol. 14A. 2005.

22. Broeckmann, C. Microstructure and mechanical properties of tool steel, in Proceedings of the 5th International Conference on Tooling, Leoben, Austria, 29 September–1 October, 1999

23. Dowey, S. J. ; Zhang, J.; Doyle, E. D. and Matthews, A. Life analysis of coated tools using statistical methods. *Surf. Coatings Technol*. 1999; 116–119, 654–661, doi: 10.1016/S0257-8972(99)00074-2.

24. Archard, J. Contact and rubbing of at surfaces. J. *Appl. Phys.* 1953, 24, 981–988

25. Stachowiak, G.W. and Batchelor, A.W. Engineering tribology. Butterworth-heineman, 2013.

26. Rigney D.A. and Hirth, J.P. Plastic Deformation and Sliding Friction of Metals. *Wear.* 1979, 53, pp. 345-370.

27. Engel, U. Prediction of tool failure from a probabilistic point of view. *J. Mater. Process. Technol.* 1994, 42, 1–13

28. Haddi, A.; Imad, A.; Vega G. On the Analysis of Die Wear in Wire-Drawing Process. Tribology Transactions. 2012, 55, 4, 466-472

29. Devia, D.M. *Mecanismos de Desgaste en Herramientas de Conformado con Recubrimientos de TiAlN por medio de Sistemas PAPVD*, Universidad Nacional de Colombia. 2012.

30. Hanson, R. A. The adhesion and deformation properties of CVD TiC coated bearing ball sunder heavy loads. MRS Online Proceedings Library (OPL), 1988.

31. Schaat, W. Sintervörgänge: Grundlagen, VDI Verlag GmbH. 1992

32. Popov, V.L. Tratamiento riguroso del contacto—El Contacto Hertziano. In Principios y Aplicaciones de la Mecánica de Contacto en Tribología, Fricción y Adherencia, 3rd ed.; Martín-Martínez, J.M., Moreno-Flores, S., Eds.; Publicacions de la Universitat d'Alacant: Alicante, España, 2015; pp. 79–85.

33. Mahajan, D.; Tajane, R. A Review on Ball Burnishing Process. *Int. J. Sci. Res. Publ.* 2013, 3, 1–8.

34. Malleswara Rao, J.N.; Chenna Kesava Reddy, A.; Rama Rao, P.V. The effect of roller burnishing on surface hardness and surface roughness on mild steel specimens. *Int. J. Appl. Eng. Research.* 2011, 1, 777–785.

35. Chomienne, V.; Valiorgue, F.; Rech, J.; Verdu, C. CIRP Journal of Manufacturing Science and Technology Influence of ball burnishing on residual stress profile of a 15-5PH stainless steel. *CIRP J. Manuf. Sci. Technol.* 2016, 13, 90–96.

36. Balland, P.; Tabourot L.; Degre, F.; Moreau, V. Mechanics of the burnishing process. *Precis Eng* 2013;37(1):129e34. https:// doi.org/10.1016/j.precisioneng.2012.07.008.

37. Amini, C.; Jerez-Mesa, R.; Travieso-Rodriguez, J.A.; Llumà, J.; Estevez-Urra, A. Finite element analysis of ball burnishing on ball-end milled surfaces considering their original topology and residual stress. *Metals* 2020;10(5). https://doi.org/10.3390/met10050638.

38. Rodríguez, A.; López de Lacalle, L.N.; Celaya, A.; Lamikiz, A.; Albizuri, J. Surface improvement of shafts by the deep ball burnishing technique (2012). Surf Coat Technol; 206:2817-2824.

39. Segawa, T.; Sasahara, H.; Tsutsumi, M. Development of a new tool to generate compressive residual stress within a machined surface. *J. Mach. Tools Manuf.* 2004, 44, 11,1215–1221.

40. Saï, W.B.; Lebrun, J.L. Influence of finishing by burnishing on surface characteristics. *J. Mater. Eng. Perform.* 2003, 12, 37–40.

41. Konefał, K.; Korzynski, M.; Byczkowska, Z.; Korzynska, K. Improved corrosion resistance of stainless steel X6CrNiMoTi17-12-2 by slide diamond burnishing. *J. Mater. Process. Technol.* 2013, 213, 1997–2004.

42. Kułakowska, A.; Patyk, R.; Bohdal, Ł.; Kałduński, P.; Chodór, J.; Koszalińska, P. Wybrane aspekty ekoinnowacyjnej obróbki nagniataniem, Srodkowo-Pomorskie Towarzystwo Naukowe Ochrony ´ Srodowiska. ´ Rocz. Ochr. Sr. 2016, Tom 18, 478–492.

43. Rech, J.; Hamdi, H.; Valette, S. Machining: fundamentals and recent advances. London: Springer; 2008 [Chapter 3].

44. Luca, L.; Neagu-Ventzel, S.; Marinescu, I. Effects of working parameters on surface finish in ball-burnishing of hardened steels. Precis Eng. 2005,29:253-6.

45. Abrao, A.M.; Denkena, B.; Kohler, J.; Breidenstein, B.; Mortke, T. The influence of deep rolling on the surface integrity of AISI 1060 high carbon steel. *Procedia CIRP*. 2014, 13:31-6.

46. Pu, Z.; Song, G.L.; Yang, S.; Outeiro, J.; Puleo, O.D.; Jawahir, D.I. Grain refined and basal textured surface produced by burnishing for improved corrosion performance of AZ31B Mg alloy. *Corrosion Sci*. 2012, 57/0:192-201.

47. Lopez de Lacalle, L.N.; Lamikiz, A.; Sanchez, J.A.; Arana, J.L. The effect of ball burnishing on heat treated steel and Inconel 718 milled surfaces. *Int J Adv Manuf Technol*. 2007, 32:958-68.

48. Abrao, A.M.; Denkena, B.; Kohler, J.; Breidenstein, B.; Mortke, T. The influence of deep rolling on the surface integrity of AISI 1060 high carbon steel. *Procedia CIRP* 2014;13:31-6.

49. García-Granada, A.A.; Gomez-Gras, G.; Jerez-Mesa, R.; Travieso-Rodriguez, J.A.; Reyes, G. Ball-burnishing effect on Deep residual stress on AISI 1038 and AA2017-T4. *Mater Manuf Process.* 2017, 32(11). https://doi.org/10.1080/10426914.2017.1317351.

50. Loh, N.H.; Tam, S.C.; Miyazawat, S. Ball burnishing of tool steel. School of Mechanical and Production Engineering, Division of Engineering. Production, Nanyang Technological University, Singapore, and Manufacturing Systems Department, Mechanical Engineering Laboratory. 1993.

51. Lee S. and Loh, N. Computer-integrated ball burnishing of a plastic-injection mould cavity insert. *J. Mater. Process. Technol.* 1996, 57, vol. 1,189–194.

52. Zhang, T.; Bugtai, N.; Marinescu, I.O. Burnishing of aerospace alloy: a theoretical-experimental approach, *J Manuf Syst*. 2014, 7/part 2: 472-478.

53. Yen, Y.C.; Sartkulvanich, P.; Altan, T. Finite element modeling of roller burnishing process. *CIRP Ann - Manuf Technol* 2005, 54/1:237-40.

54. Travieso-Rodríguez, J.A.; Jerez-Mesa, R.; Gómez-Gras, G.; Llumà-Fuentes, J.; Casadesús-Farràs, O.; Madueño-Guerrero, M. Hardening effect and fatigue behavior enhancement through ball burnishing on AISI 1038. *J Mater Res Technol*. 2019, 8(6):5639-46. https://doi.org/10.1016/j.jmrt.2019.09.032.

55. Kuznetsov, V.P.; Smolin, I.Y.; Dmitriev, A.I.; Tarasov, S.Y.; Gorgots, V.G. Toward control of subsurface strain accumulation in nanostructuring burnishing on thermostrengthened steel. *Surf. Coat. Technol*. 2016, 285, 171–178.

56. Jerez-Mesa, R.; Fargas, G.; Roa, J.J.; Llumà, J.; Travieso-Rodriguez, J.A. Superficial effects of ball burnishing on trip steel AISI 301LN sheets. *Metals* 2021, 11, 82.

57. Zaborski, A.; Tubielewicz, K.; Major, B. Contribution of burnishing to the microstructure and texture in surface layers of carbon steel. *Arch. Metall* 2000, 45, 333–341.

58. Capilla-González, G.; Martínez-Ramírez, I.; Díaz-Infante, D.; Hernández-Rodríguez, E.; Alcántar-Camarena, V.; Saldaña-Robles, A. Effect of the ball burnishing on the surface quality and mechanical properties of a TRIP steel sheet. *Int. J. Adv. Manuf. Technol*. 2021, 116, 3953–3964.

59. El-Axir, M. and Ibrahim, A. Some surface characteristics due to center rest ball burnishing. *J. Mater. Process. Technol*. 2005, 167, 1, 47–53.

60. Tadic B.; Randjelovic, S.; Todorovic, P.; Zivkovic, J.; Kocovic, V.; Budak, I.; Vukelic, D. Using a high-stiffness burnishing tool for increased dimensional and geometrical accuracies of openings. *Precis. Eng*. 2016, 43, 335–344, doi: 10.1016/j.precisioneng.2015.08.014.

61. Gharbi, F.; Sghaier, S.; Al-Fadhalah, K. and Benameur, T. Effect of ball burnishing process on the surface quality and microstructure properties of AISI 1010 steel plates. J. *Mater. Eng. Perform*. 2011, 20, 6, 903–910.

62. Okada, M.; Suenobu, S.; Watanabe, K.; Yamashita, Y.; Asakawa, N. Development and burnishing characteristics of roller burnishing method with rolling and sliding effects. *Mechatronics.* 2015, 110–118.

63. Loh, N.; Tam, S. and Miyazawa, S. Optimization of the surface finish produced by ball burnishing. *J. Mech. Technol*. 1989, 19, 1, 101–107.

64. El-Taweel, T.A.; El-Axir, M.H. Analysis and optimization of the ball burnishing process through the Taguchi technique. *Int JAdv Manuf Technol*. 2009, 41:301-10.

65. Ortner, H.; Kolaska, H. and Ettmayer, P. The history of the technological progress of hardmetals, *Int. J. Refract. Met. Hard Mater*. 2014, 148–159.

66. García, J.; Collado Ciprés, V.; Blomqvist, A. and Kaplan, B. Cemented carbide microstructures: a review. Int. J. Refract. Met. Hard Mater. 2019, vol. 80, pp. 40–68, doi: 10.1016/j.ijrmhm.2018.12.004.

67. Lay, S.; Hamar-Thibault, S. and Lackner, A. Location of VC in VC, Cr3C2 codoped WC-Co cermets by HREM and EELS. *Int. J. Refract. Met. Hard Mater*. 2002, 20, 61–69.

68. Suzuki, H. Fuke, Y. and Hayashi, K. *Powder & Powder Met, J. Jap. Soc*. 1972, 19,106–112.

69. Schubert, W.D. Doped Hexagonal Tungsten Carbide and Method for Producing Same. Patent application WO2012145773. 2011.

70. Dzierwa, A.; Markopoulos, A.P. Influence of ball-burnishing process on surface topography parameters and tribological properties of hardened steel. *Machines* 2019, 7, 11.

71. Rao, J.M.; Reddy, A.C.K.; Rao, P.R.; Mayuri, B. Finite element approach for the prediction of residual stresses in aluminum workpieces produced by roller burnishing. *Int J Des Manuf Technol* 2011;2. 0976-6995.

72. Weidow, J., Halwax, E. and Schubert, W. D. Analysis of WC with increased Ta doping. *Int. J. Refract. Met. Hard Mater*. 2015, 51, 56–60.

73. Gu, D.; Wang, H.; Dai, D.; Yuan, P.; Meiners, W.; Poprawe, R. Rapid fabrication of Al-based bulk-form nanocomposites with novel reinforcement and enhanced performance by selective laser melting. *Scr. Mater*. 2015, 96, 25–28.

74. Jones, R.M. Deformation theory of plasticity. 2009.

75. Werenskiold, J.C.; Auran, L.; Roven, H.J.; Ryum, N.; Reiso, O. Screw Extruder for Continous Extrusion of Materials with High Viscosity. International patent number EP2086697B1 WO2008 06307; Patent reference JP-A-2004 035 961; U.S. A-2 787 022

76. Hassan, A.; Al-Jalil, H. and Ebied, A. Burnishing force and number of ball passes for the optimum surface finish of brass components. *J. Mater. Process. Technol*. 1998, 83, 1, 176–179.

77. Jarfors, A.; Castagne, S.; Danno, A. and Zhang, X. Tool Wear and Life Span Variations in Cold Forming Operations and Their Implications in Microforming. *Technologies.* 2016, 5, 1. doi: 10.3390/technologies5010003.

78. Jerez-Mesa, R.; Gómez Gras, G.; Travieso-Rodriguez, J.A.; Llumà, J. Ultrasonic Vibration-Assisted Ball Burnishing Tool; Universitat Politècnica de Catalunya: Barcelona, Spain, 2018.

79. Li, F.L.; Xia, W.; Zhou, Z.Y.; Zhao, J.; Tang, Z.Q. Analytical prediction and experimental verification of surface roughness during the burnishing process. *Int J Mach Manuf* . 2012, 62:67-75.

80. Aviles, R.; Albizuri, J.; Rodriguez, A.; Lopez de Lacalle, L.N. Influence of low-plasticity ball-burnishing on the high-cycle fatigue strength of medium carbon AISI1045 steel. *Int J Fatig* 2013, 55:230-44.

81. Jerez-Mesa, R.; Landon, Y.; Travieso-Rodriguez, J.A.; Dessein, G.; Llumà-Fuentes, J.; Wagner, V. Topological surface integrity modification of AISI 1038 alloy after vibration-assisted ball burnishing. *Surf Coat Techno.l* 2018, 349, 364-377.

82. Barquins, M.; Kennel, M.; Courtel, R. Comportement demonocristaux d cuivre sous l'action de contact d'un frotteur hemisphèrique. *Wear*. 1968, 11:87-110.

83. Sayahi, M.; Sghaier, S.; Belhadjsalah, H. Finite element analysis of ball burnishing process: comparisons between numerical results and experiments. *Int J Adv Manuf Technol.* 2013, 67(5e8):1665e73. https://doi.org/10.1007/s00170-012-4599-9.

84. Maximov, J.; Duncheva, G. Finite element analysis and optimization of spherical motion burnishing of low-alloy steel. *Proc Inst Mech Eng Part C J Mech Eng Sci*. 2012, 226:161-76.

85. Swirad, S.; Wydrzynski, D.; Nieslony, P.; Krolczyk, G.M. Influence of hydrostatic burnishing strategy on the surface topography of martensitic steel. *Measurement* 2019;138:590-601.

86. Kermouche, G.; Rech, J.; Hamdi, H.; Bergheau, J. On the residual stress Field induced by a scratching round abrasive grain. *Wear* 2010;269:86-92.

87. Jerez-mesa, R.; Travieso-Rodríguez, J.A.; Landon, Y.; Dessein, G.; Lluma-fuentes, J. Comprehensive analysis of surface integrity modification of ball-end milled Ti-6Al-4V surfaces through vibration-assisted ball burnishing. *J. Mater. Process. Technol*. 2019, 267, 230–240.

88. Yang, S.; Li, W. Surface Finishing Theory and New Technology; Springer: Berlin/Heidelberg, Germany, 2018.

89. Pang, C.; Luo, H.; Zhang, Z.; Ma, Y. Precipitation behavior and grain refinement of burnishing Al-Zn-Mg alloy. *Prog Nat Sci:Mater Int* 2018;28(1):54-9. https://doi.org/10.1016/j.pnsc.2017.11.006.

90. Zhang, X.; Luo, H.; Han, Z.; Lv, J. Evolution of microstructures and texture in the surface layer of copper during burnishing process. *Mater Sci Technol* 2014;30(14):1742-50. https://doi.org/10.1179/1743284713Y.0000000463.

91. Electrical Discharge Machining - an overview; in Machinery Component Maintenance and Repair (Fourth Edition). ScienceDirect Topics. 2019.

92. Ryan, E.; Sabin, T.; Watts, J.; Whiting, M. The influence of build parameters and wire batch on porosity of wire and arc additive manufactured aluminum alloy 2319, *Journal of Materials Processing Technology*. 2018, 262, 577. //doi.org/10.1016/j.jmatprotec.2018.07.030

93. German, R. Sintering Theory and Practice. 1996.

94. Haddi, A.; Imad, A.; Vega, G.. On the Analysis of Die Wear in Wire-Drawing Process. Tribology Transactions 2012, 55: 466-472, 2012 doi: 10.1080/10402004.2012.671451

95. Wright, R. Wire technology process engineering and metallurgy 2011, (Butterworth-Heinemann).

96. Wang, X. & Kwon, P.Y. WC / Co Tool Wear in Dry Turning of Commercially Pure Aluminum . IAEME 2014. 136, 1–8. https://doi.org/10.1115/1.4026514

97. List, G.; Nouari, M.; Gehin. D.; Gomez, S.; Manaud, J. P.; Petitcorps, Y. L. and Girot, F. Wear Behaviour of Cemented Carbide Tools in Dry Machining of Aluminum Alloy. *Wear*. 2005, 259(7-12), pp. 1177-1189.

98. Girot, F.; Gutierrez-Orrantia, M. E.; Calamaz, M. and Coupard, D. Modeling and Adhesive Tool Wear in Dry Drilling of Aluminum Alloys. AIP Conf. Proc. 2011, 1315, pp. 1639-1644.

99. Rivero, A.; Aramendi, G.; Henranz, S. and Lopez de Lacalle, L. N. An Experimental Investigation of the Effect of Coatings and Cutting Parameters on the Dry Drilling Performance of Aluminum Alloys. *Int. J. Adv. Manuf. Technol*. 2006, 28(1-2), pp. 1-11.

100. Nouari, M.; List, G.; Girot, F. and Coupard, D. Experimental Analysis and Optimisation of Tool Wear in Dry Machining of Aluminum Alloys. *Wear*. 2003, 255(7-12), pp. 1359-1368.

101. Ekholm, F.; Heinrichs, J.; Wiklund, U.; Jacobson, S. Wear of cemented carbide against Cu/Zn alloys: an experimental and thermodynamic investigation. NORDTRIB 2022, Ålesund, Norway.

102. Nilsson, M. Tribology in Metal Working 2011. Uppsala University, Sweden.

103. Wang, X.; Wang, C.; She, X.; Sun, F. High-Speed Drawing of Al Alloy Wire by Diamond-Coated Drawing Die Under Environmentally Friendly Water-Based Emulsion Lubrication. *Journal of Manufacturing Science and Engineering*. 2018, 140(12): 124502 https://doi.org/10.1115/1.4041477

104. Abd-eltwab, A. A.; Elmetwally, H. & Saied, E. An Experimental Study of Lubricant Effect on Wire Drawing Process. *International Journal of Advanced Science and Technology*. 2020, 29 (1), pp. 560-568.

105. Pruncu, I.; Aherwar, A.; Gorb, S. Tribology and Surface Engineering for Industrial Applications 2021. 1st Ed. (Taylor & Francis group).

106. Ramírez, G.; Gonzalez Castro, J.M.; Orrit-Prat, J.; Bonet, R.; Cuadrado, N.; Vilaseca, M.; Carreras, L.; Caro, J. Super-Hard DLC Coatings as an Alternative to Polycrystalline Diamond for Cutting Tools: Predictive Analysis of Aluminum Alloy Surface Quality. *Lubricants.* 2022, 10, 135. https://doi.org/10.3390/lubricants10070135

107. Lu, R.; Minarro, L.; Su, Y.Y.; Shemenski, R. Failure mechanism of cemented tungsten carbide dies in wet drawing process of steel cord filament. *International Journal of Refractory Metals and Hard Materials*. 2008, 26, 6, 589-600. https://doi.org/10.1016/j.ijrmhm.2008.01.009

108. Rao, V. Tribological properties of Aluminum Metal Matrix Composites (AA7075 Reinforced with Titanium Carbide (TiC) Particles .*Int.Journal of Advanced Scienc and Tech*. 2016. 88:13-26. https://doi.org/10.14257/ijast.2016.88.02

109. Vidales, E., Cuadrado, N., Garcia-Llamas, E., Garitano, J.T., Aseguinolaza, I., Carranza, M., Vilaseca, M., Ramirez, G. Surface roughness analysis for improving punching tools

performance of 5754 aluminum alloy. *Wear*. 2023, 204743. https://doi.org/10.1016/j.wear.2023.204743

110. Zeidler, H.. & Scholz, P. Micro structuring of coated tools for dry sheet metal forming of aluminum , Eu spen's 15 th International Conference 2015.

111. Abraham, T.; Bräuer, G.; Flegler, F.; Groche, P. & Demmler, M. Dry sheet metal forming of aluminum by smooth DLC coatings – a capable approach for an efficient production process with reduced environmental impact. *Procedia Manufacturing*. 2020, 43, 642–649.

112. Czyzniewski, A. Surface & Coatings Technology Preparation and characterization of a-C and a-C : H coatings deposited by pulsed magnetron sputtering. *Surface & Coatings Technology*. 2009, 203(8), 1027–1033. https://doi.org/10.1016/j.surfcoat.2008.09.027

113. Ronkainen, H.; Varjus, S.; Koskinen, J.; Holmberg, K. Differentiating the tribological performance of hydrogenated and hydrogen-free DLC coatings. *Wear*. 2001, 249,3-4,260-266

114. Zak Fang, Z.; Wang, X.; Ryu, T.; Hwang, K.S. and Song H.Y. Synthesis, sintering, and mechanical properties of nanocrystalline cemented tungsten carbide – a review. *Int. J. Refract. Met. Hard Mater*. 2009, 27, 288.

115. González Oliver, E. A.; Álvarez C.J.R. and García, J. L. Kinetics of densification and grain growth in ultrafine WC-Co composites. *Int. J. Refract. Met. Hard Mater*. 2006, 59, 121–131

116. Exner, H.E. Physical and chemical nature of cemented carbides. *Int Met Rev*. 1979, 24,4, 149–173.

117. García J. and Pitonak, R. The role of cemented carbide functionally graded outerlayers on the wear performance of coated cutting tools. *Int. J. Refract. Met. Hard Mater*. 2013, 36, 52–59

118. Mingard, K. P.; Roebuck, B.; Marshall, J. and Sweetman, G. Some aspects of the structure of cobalt and nickel binder phases in hardmetals. *Acta Mater*. 2011, 59, 2277–2290.

119. Prakash L. and Gries, B. WC hardmetals with iron based binders, in L. Sigl, P. Rödhammer, S. Wildner (Eds.), Proc 17th International Plansee Seminar Reutte, Vol. 2. 2009

120. ISO 6892-1:2009; Metallic Materials—Tensile Testing—Part 1: Method of Test at Room Temperature, European Committee for Standardization. ISO: Geneva, Switzerland, 2009.

121. Oliver, W.; Pharr, G. An improved technique for determining hardness and elastic modulus using load and displacement sensing 669 indentation experiments. *Journal of Materials Research*. 1992, 7, 1564–1583. https://doi.org/https://doi.org/10.1557/JMR.1992.156 6704.

122. Banh, Q.; Nguyen, H.; Tran, A.S. Numerical simulation and experimental validation of surface roughness by the smoothing small ball-burnishing process. 2021.

123. Luo, H.; Liu, J.; Wang, L.; Zhong, Q. Study of the mechanism of the burnishing process with cylindrical polycrystalline diamond tools. *J Mater Proces Technol*. 2006;180:9-16. https://doi.org/10.1016/j.jmatprotec.2005.03.041.

124. Peter, H.; Ulf, B.; Mikael, O. Influence of surface topography of arc-deposited TiN and sputter-deposited WC/C coatings on the initial material transfer tendency and friction characteristics under dry sliding contact conditions. *Surf. Coat.* 2009, 203(13), 1748–1755. doi:10.1016/j.surfcoat.2008.12.011

125. Fortin, M.; Glowinski, R. Augmented Lagrangian methods: applications to the numerical solution of boundary value problems. Elsevier B.V; 1991.

126. Labuz, J.F.; Zang, A. Mohr-Coulomb failure criterion. Rock Mech Rock Eng 2012;45(6):975e9. https://doi.org/10.1007/s00603-012-0281-7.

127. El-Tayeb, N.S.M.; Low, K.O.; Brevern, P.V. Influence of roller burnishing contact width and burnishing orientation on surface quality and tribological behaviour of Aluminum 6061. *J. Mater. Process. Technol.* 2007, 186, 272–278.

128. Michael, A.; Shercliff, H.; Cebon, D. Materials: Engineering, Science, Processing and Design, 1st ed.; Butterworth-Heinemann: Cambridge, UK, 2007; ISBN 978-0-7506-8391-3.

129. Yang, S.; Li, W. Surface Finishing Theory and New Technology; Springer: Berlin/Heidelberg, Germany, 2018

130. Magnabosco, R.; Alonso-falleiros, N. Effect of Aging Heat Treatment H950 and H1000 on Mechanical and Pitting Corrosion Properties of UNS S46500 Stainless Steel. *Mater. Res*. 2018, 22, 1–9.

131. Boillat, R.; Isanaka, S.P.; Liou, F. The Effect of Nanostructures in Aluminum Alloys Processed Using Additive Manufacturing on Microstructural Evolution and Mechanical Performance Behavior. *Crystals* 2021, 11, 524. https://doi.org/10.3390/cryst11050524

132. Ponche, R.; Hascoët, J.; Kerbrat, O.; Mognol, P.; Ponche, R.; Hascoët, J.; Kerbrat, O.; Mognol, P. A new global approach to design for additive manufacturing. HALL 2013. Id: hal-00781211.

133. Langelandsvik, G. Wire Arc Additive Manufacturing of Aluminum Alloys (263). Doctoral thesis, NTNU, Norway, 2021

134. Mathers, G. (n.d.). The welding of aluminum and its alloys. Woodhead Publishing Limited, Abington Hall, Abington Cambridge CB1 6AH, England. 2002

135. Langelandsvik, G.; Grandcolas, M.; Skorpen, K. G.; Furu, T.; Akselsen, O. M.; Roven, H. J. Development of al-tic wire feedstock for additive manufacturing by metal screw extrusion. *Metals* 2020, 10 (11), 1–17. https://doi.org/10.3390/met10111485

136. Haselhuhn, A.S.; Buhr, M.W.; Wijnen, B.; Sanders, P. G.; Pearce, J.M. Structure-property relationships of common aluminum weld alloys utilized as feedstock for gmaw-based 3-d metal printing. *Materials Science and Engineering*: A. 2016, 673, 511-523. https://doi.org/10.1016/j.msea.2016.07.099

137. Frazier W.E. Metal additive manufacturing: a review. Journal of Materials Engineering and performance 2014, 23(6):1917–1928

138. Ng, C–H.; Yahaya, S. and Majid A. Reviews on aluminum alloy series and its applications. *Academia Journal of Scientific Research*. 2017, 5(12): 708-716. https://doi.org/10.15413/ajsr.2017.0724

139. Langelandsvik, G., Eriksson, M., Akselsen, O.M. et al. Wire arc additive manufacturing of AA5183 with TiC nanoparticles. *Int J Adv Manuf Technol*. 2022, 119, 1047–1058. https://doi.org/10.1007/s00170-021-08287-6

140. Ryan, E.; Sabin, T.; Watts, J.; Whiting, M. The influence of build parameters and wire batch on porosity of wire and arc additive manufactured aluminum alloy 2319. *Journal of Materials Processing Technology*. 2018, 262, 577. //doi.org/10.1016/j.jmatprotec.2018.07.030

141. Martin J.H.; Yahata, B.D;, Hundley, J.M.; Mayer, J.A.; Schaedler, T.A.; Pollock, T.M. 3D printing of high-strength aluminum alloys. *Nature* 2017, 549, 365–369.

142. Li, X.; Ji, G.; Chen, Z.; Addad, A.; Wu, Y.; Wang, H.; Vleugels, J.; Van Humbeeck, J.; Kruth J. Selective laser melting of nano-TiB 2 decorated AlSi10Mg alloy with high fracture strength and ductility. *Acta Mater* 2017, 129, 183–193

143. AWS A5.10/A5.10M. Specification for Bare Aluminum and Aluminum-Alloy Welding Electrodes and Rods 2021. 12th Ed.

144. Hu, J. and Chou, Y. K. Characterizations of Cutting Tool Flank Wear-Land Contact. *Wear.* 2007, 263(7-12), pp. 1454-1458.

145. Saini, M.S.; Salot, M.; Shah, S.; Joshi, M. Study on Wear Resistance of Al-Si Alloy using A 3-Body Dry Abrasive Wear Testing Machine. *International Journal of Engineering Research & Technology (IJERT)* 2016.

146. Abdelbary, A. Sliding mechanics of polymers. Wear of Polymers and Composites 2014, 37-66. https://doi.org/10.1533/9781782421788.38

147. Williams, J. E. and Rollason, C. E. Metallurgical and Practical Machining Parameters Affecting Built-Up-Edge Formation in Metal Cutting. *J. Inst. Met.* 1970, 95, pp. 144-153.

148. Abd-eltwab, A. A.; Elmetwally, H. & Saied, E. An Experimental Study of Lubricant Effect on Wire Drawing Process. *International Journal of Advanced Science and Technology.* 2020, 29 (1), pp. 560-568.

149. Wang, C.C.; Chow, H.M.; Yang, L.D; Chun, T.L. Recast layer removal after electrical discharge machining via Taguchi analysis: A feasibility study. *Journal of Materials Processing Technology.* 2009, 209(8):4134-4140. DOI: 10.1016/j.jmatprotec.2008.10.012

150. Konyashin, I.; Ries, B.; Lachmann, F.; Fry, A.T. Gradient WC-Co hardmetals: Theory and practice. *Int. Journal of Refractory Metals and Hard Materials.* 2013, 36 (2013) 10–21

151. Mcct (https://www.mcctcarbide.com/es/properties-and-application-of-gradient-cemented-carbide/)